

ULTRA-WIDEBAND CIRCUITS, SYSTEMS, AND APPLICATIONS

GUEST EDITORS: YO-SHENG LIN, BAORYONG CHI, HSIEN-CHIN CHIU,
AND HSIAO-CHIN CHEN





Ultra-Wideband Circuits, Systems, and Applications

Journal of Electrical and Computer Engineering

**Ultra-Wideband Circuits, Systems,
and Applications**

Guest Editors: Yo-Sheng Lin, Baoyong Chi, Hsien-Chin Chiu,
and Hsiao-Chin Chen



Copyright © 2012 Hindawi Publishing Corporation. All rights reserved.

This is a special issue published in “Journal of Electrical and Computer Engineering.” All articles are open access articles distributed under the Creative Commons Attribution License, which permits unrestricted use, distribution, and reproduction in any medium, provided the original work is properly cited.

Editorial Board

The editorial board of the journal is organized into sections that correspond to the subject areas covered by the journal.

Circuits and Systems

M. T. Abuelma'atti, Saudi Arabia	Yong-Bin Kim, USA	Gabriel Robins, USA
Ishfaq Ahmad, USA	H. Kuntman, Turkey	Mohamad Sawan, Canada
Dhamin Al-Khalili, Canada	Parag K. Lala, USA	Raj Senani, India
Wael M. Badawy, Canada	Shen-Iuan Liu, Taiwan	Gianluca Setti, Italy
Ivo Barbi, Brazil	Bin-Da Liu, Taiwan	Jose Silva-Martinez, USA
Martin A. Brooke, USA	Joaõ Antonio Martino, Brazil	Nicolas Sklavos, Greece
Chip Hong Chang, Singapore	Pianki Mazumder, USA	Ahmed M. Soliman, Egypt
Y. W. Chang, Taiwan	Michel Nakhla, Canada	Dimitrios Soudris, Greece
Tian-Sheuan Chang, Taiwan	Sing Kiong Nguang, New Zealand	Charles E. Stroud, USA
Tzi-Dar Chiueh, Taiwan	Shun-ichiro Ohmi, Japan	Ephraim Suhir, USA
Henry S. H. Chung, Hong Kong	Mohamed A. Osman, USA	Hannu Tenhunen, Sweden
M. Jamal Deen, Canada	Ping Feng Pai, Taiwan	George S. Tombras, Greece
Ahmed El Wakil, UAE	Marcelo Antonio Pavanello, Brazil	Spyros Tragoudas, USA
Denis Flandre, Belgium	Marco Platzner, Germany	Chi Kong Tse, Hong Kong
P. Franzon, USA	Massimo Poncino, Italy	Chi-Ying Tsui, Hong Kong
Andre Ivanov, Canada	Dhiraj K. Pradhan, UK	Jan Van der Spiegel, USA
Ebroul Izquierdo, UK	F. Ren, USA	Chin-Long Wey, USA
Wen-Ben Jone, USA		

Communications

Sofiène Affes, Canada	K. Giridhar, India	Mohammad S. Obaidat, USA
Dharma Agrawal, USA	Amoakoh Gyasi-Agyei, Ghana	Adam Panagos, USA
H. Arslan, USA	Yaohui Jin, China	Samuel Pierre, Canada
Edward Au, China	Mandeep Jit Singh, Malaysia	John N. Sahalos, Greece
Enzo Baccarelli, Italy	Peter Jung, Germany	Christian Schlegel, Canada
Stefano Basagni, USA	Adnan Kavak, Turkey	Vinod Sharma, India
Jun Bi, China	Rajesh Khanna, India	Ickho Song, Republic of Korea
Z. Chen, Singapore	Kiseon Kim, Republic of Korea	Ioannis Tomkos, Greece
René Cumplido, Mexico	D. I. Laurenson, UK	Chien Cheng Tseng, Taiwan
Luca De Nardis, Italy	Tho Le-Ngoc, Canada	George Tsoulos, Greece
M.-G. Di Benedetto, Italy	C. Leung, Canada	Laura Vanzago, Italy
J. Fiorina, France	Petri Mähönen, Germany	Roberto Verdone, Italy
Lijia Ge, China	M. Abdul Matin, Bangladesh	Guosen Yue, USA
Zabih F. Ghassemlooy, UK	M. Nájjar, Spain	Jian-Kang Zhang, Canada

Signal Processing

S. S. Aghaian, USA	Paul Dan Cristea, Romania	Zabih F. Ghassemlooy, UK
P. Agathoklis, Canada	Petar M. Djuric, USA	Ling Guan, Canada
Jaakko Astola, Finland	Igor Djurović, Montenegro	Martin Haardt, Germany
Tamal Bose, USA	Karen Egiazarian, Finland	Peter Handel, Sweden
A. G. Constantinides, UK	W. S. Gan, Singapore	Andreas Jakobsson, Sweden



Jiri Jan, Czech Republic
S. Jensen, Denmark
Chi Chung Ko, Singapore
M. A. Lagunas, Spain
J. Lam, Hong Kong
D. I. Laurensen, UK
Riccardo Leonardi, Italy
Mark Liao, Taiwan
Stephen Marshall, UK
Antonio Napolitano, Italy

Sven Nordholm, Australia
S. Panchanathan, USA
Periasamy K. Rajan, USA
Cdric Richard, France
William Sandham, UK
Ravi Sankar, USA
Dan Schonfeld, USA
Ling Shao, UK
John J. Shynk, USA
Andreas Spanias, USA

Srdjan Stankovic, Montenegro
Yannis Stylianou, Greece
Ioan Tabus, Finland
Jarmo Henrik Takala, Finland
A. H. Tewfik, USA
Jitendra Kumar Tugnait, USA
Vesa Valimaki, Finland
Luc Vandendorpe, Belgium
Ari J. Visa, Finland
Jar Ferr Yang, Taiwan

Contents

Ultra-Wideband Circuits, Systems, and Applications, Yo-Sheng Lin, Baoyong Chi, Hsien-Chin Chiu, and Hsiao-Chin Chen

Volume 2012, Article ID 567230, 2 pages

All-Optical Fiber Interferometer-Based Methods for Ultra-Wideband Signal Generation,

Kais Dridi and Habib Hamam

Volume 2012, Article ID 314872, 6 pages

UWB Localization System for Indoor Applications: Concept, Realization and Analysis, Lukasz Zwirello,

Tom Schipper, Marlene Harter, and Thomas Zwick

Volume 2012, Article ID 849638, 11 pages

Performance Analysis of Ultra-Wideband Channel for Short-Range Monopulse Radar at Ka-Band,

Naohiko Iwakiri, Natsuki Hashimoto, and Takehiko Kobayashi

Volume 2012, Article ID 710752, 9 pages

Ultrawideband Technology in Medicine: A Survey, R. Cha'vez-Santiago, I. Balasingham, and J. Bergsland

Volume 2012, Article ID 716973, 9 pages

Ranging Performance of the IEEE 802.15.4a UWB Standard under FCC/CEPT Regulations, Thomas Gigl,

Florian Troesch, Josef Preishuber-Pfluegl, and Klaus Witrisal

Volume 2012, Article ID 218930, 9 pages

Analysis and Mitigation of the Narrowband Interference Impact on IR-UWB Communication Systems,

Ehab M. Shaheen and Mohamed El-Tanany

Volume 2012, Article ID 348982, 8 pages

Editorial

Ultra-Wideband Circuits, Systems, and Applications

Yo-Sheng Lin,¹ Baoyong Chi,² Hsien-Chin Chiu,³ and Hsiao-Chin Chen⁴

¹ Department of Electrical Engineering, National Chi Nan University, Puli 545, Nantou, Taiwan

² Institute of Microelectronics, Tsinghua University, Beijing 100084, China

³ Department of Electronic Engineering, Chang Gung University, Kwei-Shan 333, Taoyuan, Taiwan

⁴ Department of Electrical Engineering, National Taiwan University of Science and Technology, Taipei 106, Taiwan

Correspondence should be addressed to Yo-Sheng Lin, stephenlin@ncnu.edu.tw

Received 21 May 2012; Accepted 21 May 2012

Copyright © 2012 Yo-Sheng Lin et al. This is an open access article distributed under the Creative Commons Attribution License, which permits unrestricted use, distribution, and reproduction in any medium, provided the original work is properly cited.

Ultra-wideband (UWB) technology include many applications, such as WiGig, home networking, wireless universal serial bus (USB), wireless personal area network (WPAN), wireless body area network (WBAN), healthcare and medical imaging, and automotive radar. The burgeoning application of UWB technology has brought about new challenges and opportunities for both the academia and the industry. For example, recently, many groups are dedicated to the application of UWB technology on medical sensing, localization, and communication, which leads to potential applications in medicine, especially for less invasive medical diagnosis and monitoring. Undoubtedly, with UWB technology, current wireless health systems and novel medical applications can be further improved and developed.

Ka-band UWB vehicular radars can inherently achieve high-range resolution. In the research article entitled “Performance analysis of ultra-wideband channel for short-range monopulse radar at Ka-band,” the development and measurement results of a prototype UWB monopulse radar equipped with a two-element receiving antenna array are illustrated. Additionally, to design suitable radar’s waveforms, performance degradation attributed to a number of averaged received monopulses is examined.

Furthermore, in the research article entitled “Analysis and mitigation of the narrowband interference impact on IR-UWB communication systems,” the impact of narrowband interference signals on impulse radio UWB communication systems is investigated by proposing an interference canceller scheme. This scheme is capable of suppressing the impact of such interference and enhancing the performance of UWB communication systems.

UWB signal generation is critical in UWB communication systems. In the research article entitled “All-optical fiber-interferometer-based methods for ultra-wideband signal generation,” two new, simple, and cost-effective all-optical methods for generating UWB impulse radio signals are reported. These methods not only generate UWB pulses optically but also assure the propagation over optical networks.

UWB signals show robustness against multipath interference and allow for high-accuracy positioning. Thus, it is promising to apply them in real-time locating systems (RTLSs) and wireless sensor networks which adopt the IEEE 802.15.4a standard. In the research article entitled “Ranging performance of the IEEE 802.15.4a UWB standard under FCC/CEPT regulations,” a coherent receiver and an energy detector (i.e., a noncoherent receiver) are studied for ranging in IEEE 802.15.4a, in the sense of maximal allowed transmit energy and path-loss, and maximal operating distance.

In the research article entitled “UWB localization system for indoor applications: concept, realization and analysis,” a complete UWB indoor localization demonstrator is presented. This demonstrator is targeted on operation with a predeployed access point infrastructure. The proposed methods have improved the average accuracy from 9 cm to 2.5 cm.

The inherent features of the UWB radio signals make them highly suitable for less invasive medical application. For example, the UWB radar may be used in novel noninvasive sensing and imaging techniques thanks to its high temporal resolution for detecting backscattered signals. In the review article entitled “Ultra-wideband technology in medicine: a survey,” the authors described their current research on the application of the UWB technology to noninvasive

measurement of blood pressure. In addition, they reported a survey of recent research in UWB technology for medical sensing and communications.

The Guest Editors of this special issue acknowledge all the authors who responded to the call for papers, and they thank all the reviewers for their dedication for ensuring a high standard for the selected papers. Though this special issue only covers some but not all of the important areas related to ultra-wideband circuits, systems, and applications, we hope that readers will find this issue insightful and useful.

Yo-Sheng Lin
Baoyong Chi
Hsien-Chin Chiu
Hsiao-Chin Chen

Research Article

All-Optical Fiber Interferometer-Based Methods for Ultra-Wideband Signal Generation

Kais Dridi and Habib Hamam

EMAT Laboratory, Electrical Department, Faculty of Engineering, University of Moncton, 18 Avenue Antonine Maillet, Moncton, NB, Canada E1A 3E9

Correspondence should be addressed to Kais Dridi, k.dridi@gmail.com and Habib Hamam, habib.hamam@gmail.com

Received 28 October 2011; Accepted 8 April 2012

Academic Editor: Baoyong Chi

Copyright © 2012 K. Dridi and H. Hamam. This is an open access article distributed under the Creative Commons Attribution License, which permits unrestricted use, distribution, and reproduction in any medium, provided the original work is properly cited.

We report two new, simple, and cost-effective all-optical methods to generate ultra-wideband (UWB) impulse radio signals. The proposed methods are based on fiber-interferometric structures, where an input pulse is split and propagates along the two interferometer arms. The interference of these pulses at the output of the interferometer leads to UWB pulse generation. A theoretical analysis is provided and some relevant simulation results are presented. Large bandwidths are obtained while satisfying the requirements of the Federal Communication Commission (FCC). With these two techniques, UWB pulses can be readily generated and cost-effectively propagated through optical fibers.

1. Introduction

Major advances in wireless communications, networking, radar, imaging, and positioning systems have been made since the fast emergence of ultra-wideband (UWB) technology. UWB radio technology converges towards being a strongest candidate compared to the other existing radio technologies. It has gained ground since the USA FCC's proposed rulemaking. In its Report and Order (R&O) issued in February 2002, large bandwidth from 3.1 to 10.6 GHz has been unleashed with an isotropic radiated power level of less than -41 dBm/MHz. Besides, this radio technology owns its success due to its intrinsic features and benefits including low power consumption, low complexity, low cost, wide occupied bandwidth, high data rates, immunity to multipath fading, and high security [1–3].

Unfortunately, shot-range propagation is still considered as a main limitation preventing widespread deployment of such technology: transmitted signals can propagate for distances less than 10 meters as illustrated by Figure 1. To overcome this inherent restriction, solutions based on the integration of optical fibers and UWB radio are promising. The idea is to widen the area of coverage by means of

small antennas interconnected by optical fibers. Large surface can hence be divided into small picocells where low-power transmitters are used. A key point in such architecture is the fact that UWB pulses are generated from a central station (CS) and distribute to UWB access points (UWB-AP) through optical fibers as shown in Figure 1. This way saves optoelectronic (O/E) conversions, which limit the bandwidth. In addition, it ensures seamless integration with the high-rate optical networks. Thus, UWB over fiber (UWB-o-F) system can be deployed to achieving high data rate access in an indoor environment.

UWB signals have been generated both electronically [4–8] and optically [9–22]. Several approaches have been proposed for optical UWB signal generation. For example, monocycle pulses have been generated using a hybrid system based on a gain switched Fabry-Pérot laser diode (FPLD) and a microwave differentiator [9, 10]. Other techniques were based on cross-phase modulation (XPM) [11] and cross-gain modulation (XGM) [12] in a semiconductor optical amplifier (SOA). Birefringence time delay has been also applied by cascading phase modulator (PM) with a polarization maintaining fiber (PMF) [13]. Generation based on the gain saturation of a dark return-to-zero (RZ) signal in an SOA

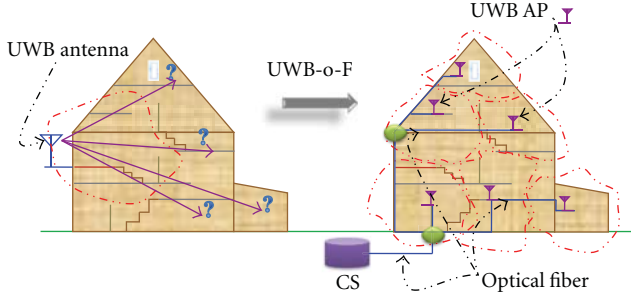


FIGURE 1: An UWB-o-F system for high data rate coverage (UWBAP: UWB Access Point).

[14] has been also demonstrated. Moreover, other types of UWB signals (e.g., doublet) have been generated based on a Mach-Zehnder modulator (MZM) biased at a nonlinear region [15], a combination of an optical phase modulator with a dispersive fiber [16], and a special frequency shift keying modulator [17], and a conversion from phase modulation (PM) to intensity modulation (IM) is performed by an optical frequency discriminator-based Fiber Bragg Grating (FBG) [18–22]. The aforementioned techniques require a lot of adjustment and control to be able to ensure a relative stable UWB pulse generation. This may lead to complex solutions, which will be costly when implementing. In this paper, we advance two new and simple approaches for monocycle and doublet UWB signal generation in the optical domain.

2. Development of the Design Methods

In nonlinear (NL) dispersive fibers, propagation of optical pulses is governed by a propagation equation which can be reduced to the nonlinear Schrödinger Equation (NLSE) under certain conditions [23]. The propagation equation can be written as follows:

$$i \frac{\partial u}{\partial z} + i\beta_1 \frac{\partial u}{\partial t} + i\frac{\alpha}{2}u - \frac{1}{2}\beta_2 \frac{\partial^2 u}{\partial t^2} - \frac{i}{6}\beta_3 \frac{\partial^3 u}{\partial t^3} + \gamma|u|^2u = 0, \quad (1)$$

where u is the slowly varying amplitude of the incident pulse envelope, α is the attenuation coefficient related to fiber losses effects, and β_2 and β_3 are, respectively, the second- and third-order dispersion parameters: the group velocity dispersion (GVD) ($[\text{ps}^2/\text{Km}]$) and the third-order dispersion (TOD) ($[\text{ps}^3/\text{Km}]$) parameters. The nonlinear parameter is represented by γ known as the self-phase modulation (SPM) parameter. β_1 is the first-order dispersion constant or merely the inverse of the group velocity v_g ($[\text{ps}/\text{Km}]$).

Suppose that a related time frame T which is measured in a frame of reference moving with the pulse at the group velocity v_g ($T = \tau - (z/v_g) = t - \beta_1 z$). The β_1 term of (1) can be omitted. Besides, since pulses are significantly larger than 5 picoseconds, TOD as well as nonlinear effects can also be neglected [24]. In a previous work and for another application a more rigorous analysis including TOD was carried out [24]. However in our present application the pulse width is larger than 10 ps, which means that TOD and

nonlinear effects have insignificant meaning. By neglecting the TOD (and preserving the non linear parameter γ for the moment) we obtain

$$i \frac{\partial u}{\partial z} + i\frac{\alpha}{2}u - \frac{1}{2}\beta_2 \frac{\partial^2 u}{\partial T^2} + \gamma|u|^2u = 0. \quad (2)$$

Let us consider the case where only the dispersion is dominating and the pulse is propagating in a lossless medium ($\alpha = 0$); (2) can be rewritten as

$$i \frac{\partial u}{\partial z} = \frac{1}{2}\beta_2 \frac{\partial^2 u}{\partial T^2}. \quad (3)$$

Nonlinearity effects can be neglected under the following condition: $L_d/L_{nl} \ll 1$, where L_d is the dispersion length expressed by $T_0^2/|\beta_2|$ and L_{nl} is the nonlinear length expressed by $1/\gamma P_0$. P_0 and T_0 are, respectively, the peak power and initial width for the incident pulse. For given values of the fiber parameters γ and β_2 , P_0 should be $\ll 1$. W and T_0 should be in the picoseconds range.

Consider now a normalized amplitude $s(z, \tau)$ introduced as follows:

$$u(z, \tau) = \sqrt{P_0} \exp\left(-\frac{\alpha z}{2}\right) s(z, \tau), \quad (4)$$

where τ is a time scale—normalized to the input pulse width T_0 —defined by T/T_0 .

Under all the aforementioned conditions, if we define the normalized amplitude $s(z, T)$ according to (4), $s(z, T)$ satisfies the following partial differential equation:

$$i \frac{\partial s}{\partial z} = \frac{1}{2}\beta_2 \frac{\partial^2 s}{\partial T^2}. \quad (5)$$

The expansion of (5) leads to

$$i(s(z + \Delta z, T) - s(z, T)) = \frac{1}{2}\Delta z \beta_2 \frac{\partial^2 s}{\partial T^2}. \quad (6)$$

Let us suppose the difference between the two fields $s(z + \Delta z, T)$ and $s(z, T)$ as an output signal described by the following expression:

$$s^1_{\text{out}}(z, T) = s(z + \Delta z, T) - s(z, T). \quad (7)$$

Expression (7) represents a *spatial difference* since it is a difference fulfilled in the space (i.e., z) domain. In addition to this *spatial difference*, a *temporal difference* can be achieved as well. This is done by fixing z and varying T by a certain delay of τ . Hence, another difference results as

$$s^2_{\text{out}}(z, T) = s(z, T - \tau) - s(z, T). \quad (8)$$

A Fourier domain analysis tells us that

$$\begin{aligned} TF(s^1_{\text{out}}(z, T))\alpha - \omega^2 S(z, \omega), \\ TF(s^2_{\text{out}}(z, T))\alpha - \omega S(z, \omega). \end{aligned} \quad (9)$$

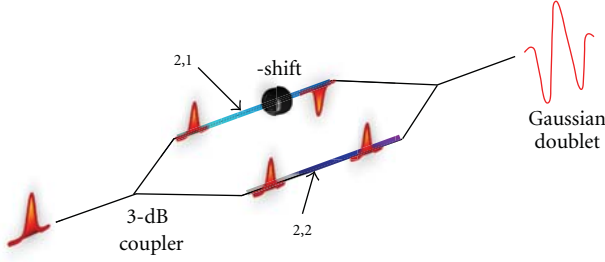


FIGURE 2: Possible doublet pulse generation scheme.

Going back to time domain, s^1_{out} and s^2_{out} are proportional to the first and second derivatives of the impulse s itself:

$$\begin{aligned} s^1_{\text{out}}(z, T) & \propto \alpha s^{(2)}(z, T), \\ s^2_{\text{out}}(z, T) & \propto \alpha s^{(1)}(z, T). \end{aligned} \quad (10)$$

Two possible schemes can hence be proposed for the generation of UWB signals. In both cases the first and the second derivatives of a Gaussian impulse give the monocycle and the doublet pulses, respectively [25, 26].

2.1. Space-Based UWB Pulse Generation. Figure 2 shows us a clear insight on how a physical implementation for UWB impulses generation would be: an interferometer system having two arms with different lengths z and $z + \Delta z$. The π -shift element induces a negative impulse.

In the following analysis, we used the expressions of s_1 and s_2 that can be deduced from the solution of (5) in two different ways:

$$\begin{aligned} s_1(z, T) & = s(z, T) \\ & = \frac{T_0}{(T_0 - i\beta_{2,1}z)^{1/2}} \exp\left(-\frac{T^2}{2(T_0^2 - i\beta_{2,1}z)}\right), \end{aligned} \quad (11)$$

$$\begin{aligned} s_2(z, T) & = s(z + \Delta z, T) \\ & = \frac{T_0}{(T_0 - i\beta_{2,1}(z + \Delta z))^{1/2}} \\ & \quad \times \exp\left(-\frac{T^2}{2(T_0^2 - i\beta_{2,1}(z + \Delta z))}\right). \end{aligned} \quad (12)$$

β_2 in (5) is $\beta_{2,1}$.

Equation (12) contains a virtual GVD parameter $\beta_{2,2}$, which is different from the first one ($\beta_{2,1}$):

$$\beta_{2,2} = \beta_{2,1} \frac{z + \Delta z}{z}. \quad (13)$$

So, instead of adding a short fiber-length (Δz) to the second arm, we can choose a fiber arm as long as the first arm but with a different dispersion parameter as depicted in Figure 3.

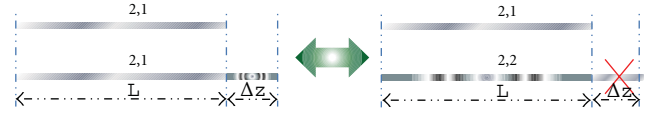


FIGURE 3: Length-dispersion equivalence.

Expression (12) becomes

$$\begin{aligned} s_2(z, T) & = s(z + \Delta z, T) \\ & = \frac{T_0}{(T_0 - i\beta_{2,2}z)^{1/2}} \exp\left(-\frac{T^2}{2(T_0^2 - i\beta_{2,2}z)}\right). \end{aligned} \quad (14)$$

For a fixed first arm length $z = L$, $\beta_{2,2}$ is constant. As a special case, if we fix z to L_d , which is the dispersion length over which the effects of dispersion become more important (introduced in Section 2), the following relationship will have an important consideration in our simulation:

$$\beta_{2,2} = \beta_{2,1} \frac{L + \Delta z}{L}. \quad (15)$$

2.2. Time-Delayed UWB Generation. Figure 4 depicts another possible interferometer-based system, which is composed of two optical fiber arms with different lengths, two optical 3-dB couplers, and a π -phase shifting device. The delay loop element assures a delay τ between the two arms. Fourier transform of the expression (8) leads to

$$S_{\text{out}}(z, \omega) = (e^{-i\omega\tau} - 1)S(z, \omega), \quad (16)$$

where S and S_{out} are, respectively, the Fourier transforms of both the injected and the output pulses. The decomposition of (16) into Taylor basis would lead to (up to the first order)

$$S_{\text{out}}(z, \omega) \approx -i\omega\tau S(z, \omega). \quad (17)$$

From (17) we can make out that the output spectrum is identical to the initial spectrum modulated by a linear function of the frequency. Let us replace $S(z, \omega)$ by the following analytical expression:

$$S(z, \omega) = S(0, \omega) \exp\left(i\frac{\beta_2}{2}\omega^2 z\right), \quad (18)$$

where $S(0, \omega)$ can be calculated as [18]

$$S(0, \omega) = \sqrt{2\pi}T_0 \exp\left(-\frac{\omega^2 T_0^2}{2}\right). \quad (19)$$

Hence, by combining (18) and (19), the spectrum of the output signal becomes

$$\begin{aligned} S_{\text{out}}(z, \omega) & = \sqrt{2\pi}T_0 (e^{-i\omega\tau} - 1) \exp\left(i\frac{\beta_2}{2}\omega^2 z\right) \\ & \quad \times \exp\left(-\frac{\omega^2 T_0^2}{2}\right). \end{aligned} \quad (20)$$

TABLE 1: Doublet generation's parameters.

P_0	FWHM	CR1	CR2	l_1	l_2	$\beta_{2,1}$	$\beta_{2,2}$
0.95 mW	62.5 ps	0.3	0.1	720 m	720 m	$-7.34 \text{ ps}^2/\text{km}$	$-5.75 \text{ ps}^2/\text{km}$

TABLE 2: Monocycle generation's parameters.

P_0	FWHM	CR1	CR2	l_1	l_2	$\beta_{2,1}$	$\beta_{2,2}$
2 mW	46.875 ps	0.5	0.5	720 m	500 m	$-22.28 \text{ ps}^2/\text{km}$	$-22.28 \text{ ps}^2/\text{km}$

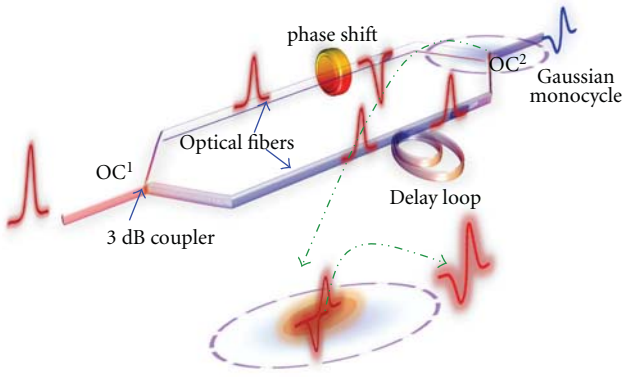


FIGURE 4: Time delay interferometer (OC: Optical Coupler).

Since the initial spectrum $S(0, \omega)$ is as large as that of the propagated signal $S(z, \omega)$, the bandwidth of the output signal (the extent of $S_{\text{out}}(z, \omega)$) does not depend on z .

In the two proposed systems, a π phase device must be inserted in one arm to implement the negative impulse function. The π -phase shift element design is not considered in our work; however, it can be implemented such as in [27] or [28].

3. Simulation Results

As a quick proof of concept, we have carried out simulations using the Photonic Transmission Design System (PTDS) simulator produced by Virtual Photonics Inc, known as VPISystems nowadays [29]. It is based on the Ptolemy open-source software [30]. Figure 5 describes a range of parameters that have been manipulated in the purpose of ensuring high-quality monocycle and doublet impulses. The injected impulse is characterized by its initial power (P_0) and its full width at half maximum (FWHM). The optical couplers control the amount of power through the interferometer by adjusting the coupling ratios CR1 and CR2. l_1 , l_2 , $\beta_{2,1}$, and $\beta_{2,2}$ are the lengths and GVD parameters of the two optical fiber arms, respectively. The semiconductor optical amplifier (SOA) gives a little amplification for the obtained impulse. In these simulations, it has been controlled through its injection current I_c . A photodetector performs a conversion from the optical to the electrical domain.

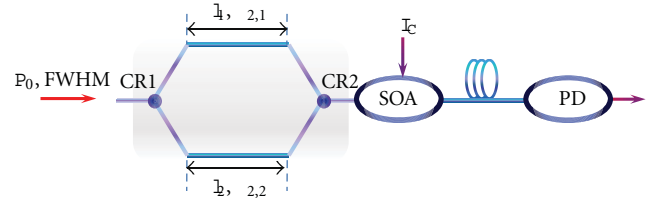


FIGURE 5: UWB pulse generation schema.

3.1. For the Space Approach. In this approach, the interferometer arms' lengths are chosen equal to 720 m (Figure 5) but with different dispersion parameters $-7.34 \text{ ps}^2/\text{km}$ and $-5.75 \text{ ps}^2/\text{km}$. A Gaussian pulse, with an FWHM of 62.5 ps, is injected via the first optical coupler which has a coupling ratio CR1 equal to 0.3. A Gaussian doublet has been generated and amplified with an SOA (biased at 150 mA). Table 1 summarizes the interferometer's parameters used for the doublet generation. A UWB doublet signal has been obtained with an FWHM of about 48.45 ps, as shown in Figure 6, with 10.7 GHz bandwidth (from 2.7 to 13.4 GHz) measured at -10 dB .

3.2. For the Time-Delay Approach. A 2 mW Gaussian pulse is launched to the interferometer system with an FWHM of about 47 ps (Figure 5). The arms' lengths are fixed to 720 m and 500 m with the same dispersion parameter of $-22 \text{ ps}^2/\text{km}$. The coupling ratios of the input and output couplers of our system are equal to 0.5 (See Table 2 for the interferometer's parameters). At the output of the second coupler, the optical monocycle pulse is amplified by a semiconductor optical amplifier (SOA) biased at 120 mA. Table 2 summarized the interferometer's parameters used for monocycle generation. After the photodetector, the resulted monocycle (Figure 7) measures an upper FWHM of about 40.625 ps and a lower FWHM of about 57.813 ps. It offers a -10 dB bandwidth of about 10.3 GHz from 2.3 to 12.6 GHz (Figure 7). The obtained spectrum respects well the requirements of the FCC spectral mask.

Both symmetry of the monocycle and the bandwidth of its spectrum can be adjusted by tuning the injection current in the SOA. The higher this current is, the more the symmetric pulse is ensured.

The time-delay approach offers a relatively broader spectrum than that obtained with the space approach. On the other hand, from a practical point of view, the latter

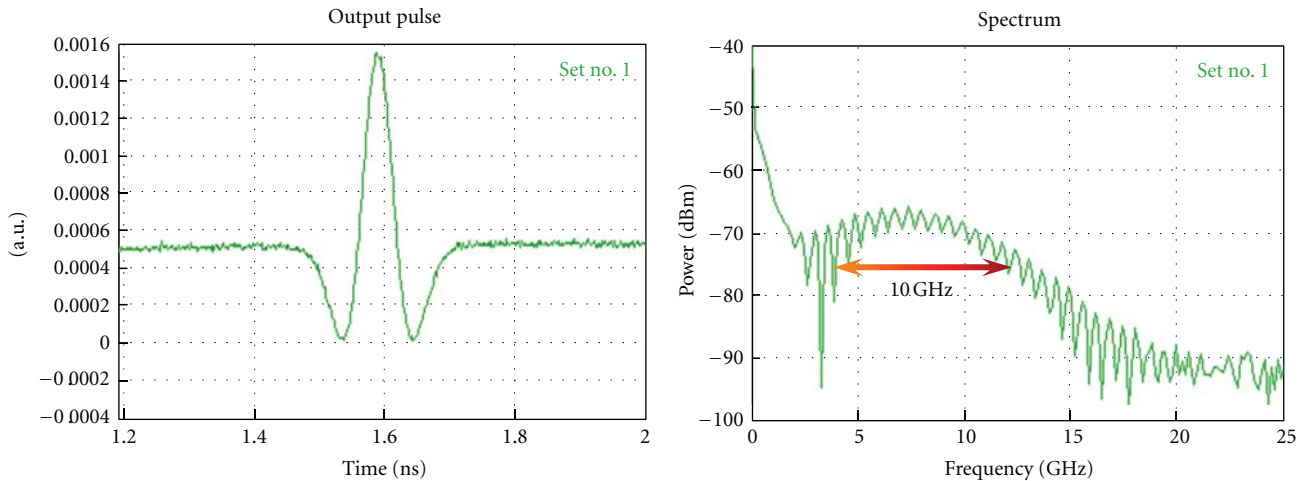


FIGURE 6: The generated doublet (a) and its spectrum (b).

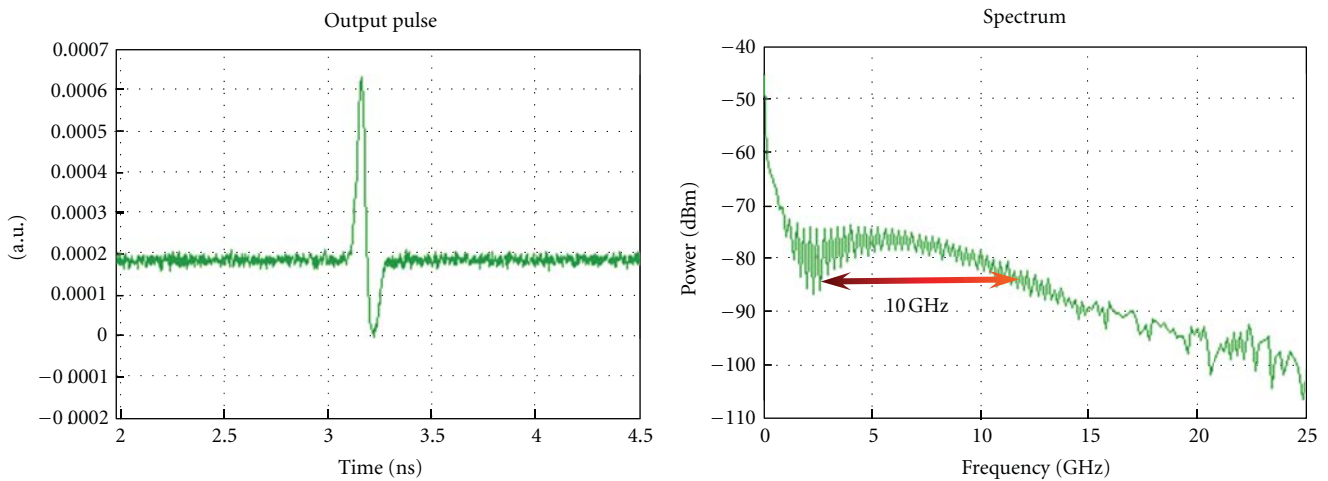


FIGURE 7: The generated monocycle (a) and its spectrum (b).

approach not only requires different and nonstandard dispersion parameters in both arms of the proposed system, but also imposes the use of fiber optic couplers with specific coupling ratios. Conversely, the former approach requires only standard fiber arms (e.g., a standard Corning SMF-28) with 50% fiber optic couplers. The time-delay approach is thus more simple and cost-effective solution for experimental investigation, albeit it shows comparative results with the other method.

4. Conclusion

New all-optical UWB pulses generation methods have been demonstrated and approved by simulations. While the first one is based on time-delay approach to generate monocycle pulse, the second approach has a spatial perspective where the chromatic dispersion is exploited to generate doublet pulse. Both methods use an interferometric architecture incorporating a π -device shift. Interesting bandwidths have

been obtained meeting the FCC requirements. With these methods, not only can UWB pulses be generated optically but also their propagation over optical networks is simply assured. Experimental assessment would be a key point as a future work.

References

- [1] G. R. Aiello, "Challenges for Ultra-wideband (UWB) CMOS integration," in *Proceedings of the IEEE MTT-S International Microwave Symposium Digest*, vol. 1, pp. 361–364, June 2003.
- [2] D. Porcino and W. Hirt, "Ultra-wideband radio technology: potential and challenges ahead," *IEEE Communications Magazine*, vol. 41, no. 7, pp. 66–74, 2003.
- [3] M. Ghavami, L. B. Michael, and R. Kohno, *Ultra WideBand Signals and Systems in Communication Engineering*, Wiley, West Sussex, UK, 2004.
- [4] X. Chen and S. Kiaei, "Monocycle shapes for ultra wideband system," in *Proceedings of the IEEE International Symposium on Circuits and Systems*, vol. 1, pp. 26–29, May 2002.

- [5] K. Marsden, H.-J. Lee, D. S. Ha, and H.-S. Lee, "Low power CMOS re-programmable pulse generator for UWB systems," in *Proceedings of the IEEE Conference on Ultra Wideband Systems and Technologies*, pp. 337–443, November 2003.
- [6] H. Kim, D. Park, and Y. Joo, "All-digital low-power CMOS pulse generator for UWB system," *Electronics Letters*, vol. 40, no. 24, pp. 1534–1535, 2004.
- [7] Y. Jeong, S. Jung, and J. Liu, "A CMOS impulse generator for UWB wireless communication systems," in *Proceedings of the IEEE International Symposium on Circuits and Systems*, pp. 129–132, May 2004.
- [8] B. Jung, Y. H. Tseng, J. Harvey, and R. Harjani, "Pulse generator design for UWB IR communication systems," in *Proceedings of the IEEE International Symposium on Circuits and Systems (ISCAS '05)*, pp. 4381–4384, May 2005.
- [9] W. P. Lin and J. Y. Chen, "Implementation of a new ultrawideband impulse system," *IEEE Photonics Technology Letters*, vol. 17, no. 11, pp. 2418–2420, 2005.
- [10] W. P. Lin and Y. C. Chen, "Design of a new optical impulse radio system for ultra-wideband wireless communications," *IEEE Journal on Selected Topics in Quantum Electronics*, vol. 12, no. 4, pp. 882–887, 2006.
- [11] J. Dong, X. Zhang, J. Xu, D. Huang, S. Fu, and P. Shum, "Ultra-wideband monocycle generation using cross-phase modulation in a semiconductor optical amplifier," *Optics Letters*, vol. 32, no. 10, pp. 1223–1225, 2007.
- [12] Q. Wang, F. Zeng, S. Blais, and J. Yao, "Optical ultrawideband monocycle pulse generation based on cross-gain modulation in a semiconductor optical amplifier," *Optics Letters*, vol. 31, no. 21, pp. 3083–3085, 2006.
- [13] H. Chen, M. Chen, C. Qiu, J. Zhang, and S. Xie, "UWB monocycle pulse generation by optical polarisation time delay method," *Electronics Letters*, vol. 43, no. 9, pp. 542–543, 2007.
- [14] J. Dong, X. Zhang, J. Xu, and D. Huang, "All-optical ultrawideband monocycle generation utilizing gain saturation of a dark return-to-zero signal in a semiconductor optical amplifier," *Optics Letters*, vol. 32, no. 15, pp. 2158–2160, 2007.
- [15] Q. Wang and J. Yao, "UWB doublet generation using nonlinearly-biased electro-optic intensity modulator," *Electronics Letters*, vol. 42, no. 22, pp. 1304–1305, 2006.
- [16] F. Zeng and J. Yao, "An approach to ultrawideband pulse generation and distribution over optical fiber," *IEEE Photonics Technology Letters*, vol. 18, no. 7, pp. 823–825, 2006.
- [17] T. Kawanishi, T. Sakamoto, and M. Izutsu, "Ultra-wide-band radio signal generation using optical frequency-shift-keying technique," *IEEE Microwave and Wireless Components Letters*, vol. 15, no. 3, pp. 153–155, 2005.
- [18] F. Zeng and J. Yao, "Optical generation and distribution of UWB signals," in *Proceedings of the International Conference on Communications, Circuits and Systems (ICCCAS '06)*, vol. 3, pp. 2024–2029, June 2006.
- [19] F. Zeng and J. Yao, "Ultrawideband impulse radio signal generation using a high-speed electrooptic phase modulator and a fiber-bragg-grating-based frequency discriminator," *IEEE Photonics Technology Letters*, vol. 18, no. 19, pp. 2062–2064, 2006.
- [20] F. Zeng, Q. Wang, and J. Yao, "All-optical UWB impulse generation based on cross-phase modulation and frequency discrimination," *Electronics Letters*, vol. 43, no. 2, pp. 119–121, 2007.
- [21] C. Wang, F. Zeng, and J. Yao, "All-fiber ultrawideband pulse generation based on spectral shaping and dispersion-induced frequency-to-time conversion," *IEEE Photonics Technology Letters*, vol. 19, no. 3, pp. 137–139, 2007.
- [22] J. Li, K. Xu, S. Fu et al., "Ultra-wideband pulse generation with flexible pulse shape and polarity control using a Sagnac-interferometer-based intensity modulator," *Optics Express*, vol. 15, no. 26, pp. 18156–18161, 2007.
- [23] G. P. Agrawal, *Nonlinear Fiber Optics*, Academic Press, 3rd edition, 2001.
- [24] M. Razzak, S. Guizani, H. Hamam, and Y. Bouslimani, "Optical post-equalization based on self-imaging," *Journal of Modern Optics*, vol. 53, no. 12, pp. 1675–1684, 2006.
- [25] X. Chen and S. Kiaei, "Monocycle shapes for ultra wideband system," in *Proceedings of the IEEE International Symposium on Circuits and Systems*, pp. 597–600, May 2002.
- [26] B. Hu and N. C. Beaulieu, "Pulse shapes for ultrawideband communication systems," *IEEE Transactions on Wireless Communications*, vol. 4, no. 4, pp. 1789–1797, 2005.
- [27] J. R. Kurz, K. R. Parameswaran, R. V. Roussev, and M. M. Fejer, "Optical-frequency balanced mixer," *Optics Letters*, vol. 26, no. 16, pp. 1283–1285, 2001.
- [28] O. Deparis, R. Kiyari, O. Pottiez et al., "Bandpass filters based on π -shifted long-period fiber gratings for actively mode-locked erbium fiber lasers," *Optics Letters*, vol. 26, no. 16, pp. 1239–1241, 2001.
- [29] VPISystems, <http://www.vpisystems.com/>.
- [30] Ptolemy Project, <http://www.ptolemy.eecs.berkeley.edu/index.htm>.

Research Article

UWB Localization System for Indoor Applications: Concept, Realization and Analysis

Lukasz Zwirello, Tom Schipper, Marlene Harter, and Thomas Zwick

Institut für Hochfrequenztechnik und Elektronik, Karlsruhe Institute of Technology (KIT), Kaiserstraße 12, 76131 Karlsruhe, Germany

Correspondence should be addressed to Lukasz Zwirello, lukasz.zwirello@kit.edu

Received 29 October 2011; Accepted 4 February 2012

Academic Editor: Baoyong Chi

Copyright © 2012 Lukasz Zwirello et al. This is an open access article distributed under the Creative Commons Attribution License, which permits unrestricted use, distribution, and reproduction in any medium, provided the original work is properly cited.

A complete impulse-based ultrawideband localization demonstrator for indoor applications is presented. The positioning method, along with the method of positioning error predicting, based on scenario geometry, is described. The hardware setup, including UWB transceiver and time measurement module, as well as the working principles is explained. The system simulation, used as a benchmark for the quality assessment of the performed measurements, is presented. Finally, the measurement results are discussed. The precise analysis of potential error sources in the system is conducted, based on both simulations and measurement. Furthermore, the methods, how to improve the average accuracy of 9 cm by including the influences of antennas and signal-detection threshold level, are made. The localization accuracy, resulting from those corrections, is 2.5 cm.

1. Introduction

In the recent decade, a growing interest in precise indoor locating systems could be observed. At the moment, several methods, based on different technologies, targeted for various environments are being investigated worldwide. They can be divided into acoustic [1, 2], optical [3], and radio frequency methods. The last type of methods can be divided into continuous wave (CW), for example, WLAN or RFID [4], and impulse signals. CW systems suffer however either from low accuracy, lack of immunity against multipath effects, or from requirement for large number of sensors. The short ultrawideband (UWB) pulses are ideal candidates for indoor localization applications. Their short duration assures the resistance against multipath effects and gives a supreme time resolution. Because of the fact that the UWB has a very strict power emission limits [5, 6], the short-range (e.g., indoor) applications are aimed for.

In this work, a complete process of designing a UWB positioning system is presented, starting from the choice of positioning method, through placement of access points, analysis of error sources in the UWB transceiver, and ending with simulation and measurement verification. The

transmitter and receiver architecture, as well as the hardware used during the localization experiments, are briefly described, and for more details, respective references are placed in the paper.

This paper is structured as follows: first, the positioning method is described in Section 2, and the best algorithm, in terms of accuracy and computational effort, for solving the TDoA equations is determined. In Section 3, the consideration of optimal placement of receivers is given. Based on this, the positioning accuracy limit is derived. Section 4 is dedicated to the description of the constructed UWB transceiver and used for measurement validation, as well as to the TDoA measurement setup. In access to this, the influence of the used antenna type on localization precision and signal digitizing units will be described in Section 5; the correction algorithms for compensation of those two effects will be proposed here as well. In Section 6, a model of the laboratory room is presented, which was used for determination of the system capabilities. In the same section, also the simulation-based result quality prediction method, along with the localization results, is presented. The last Section 7 summarizes the presented work, followed by the conclusions and finally improvement proposals for future implementations.

2. Positioning Method

In order to choose the best suited positioning method for a specific application, first the boundary conditions have to be known. The aimed application scenario for the UWB system is the localization of mobile users (MUs) in indoor scenarios like, for example, office rooms or industrial halls. In such scenarios, the only prerequisite would be the access points (APs) which are aware of their own position.

Depending on the kind of positioning method, a synchronization between APs and MUs may be required or not. In the given scope of applications, where no information about the MU is given, only the relative time methods such as the time difference of arrival (TDoA) or the angle of arrival (AoA) method are suitable.

The TDoA method requires information about the signal propagation time from the MU (transmitter) to all the APs (receivers). For a 3D positioning, there are at least four APs needed. The resulting set of nonlinear equations can be solved either by iterative or direct methods (more on this in Section 2.2). In the AoA approach, an antenna array is used in each AP. Behind each array element, a UWB receiver is placed, and the difference in receive times is measured. Based on this, the angle of arrival for a signal can be determined by a linear equation. In this method in every AP, an antenna array consisting of at least three elements, aligned not in line, is required for 3D localization, and a minimum of two APs need to be used.

In the experiment presented in this paper, the TDoA method was utilized. In future application, it is advisable to combine the TDoA and AoA to achieve synergy effects [7].

There are two ways of performing the TDoA measurement in a system consisting of multiple APs and MUs:

- (1) either the MU sends its user-specific information sequence, coded by UWB pulses, and it will be localized by a central processing unit (CPU), where the CPU synchronizes all the APs and collects the time measurement data,
- (2) or the APs will be used only as repeaters. In this case, the MU receives back the transmitted signal, in addition containing the information from which AP (coordinates) it came. In this concept the MU has to calculate its own location, based on relative distance information to the reference nodes (APs) [8, 9]. This is based on the *two-way-ranging* measurement principle.

In this work, the first of the two presented alternatives was chosen. The second method would be more practical for the end application, especially in larger scenarios, due to the highly reduced wiring effort. In the general case, the positioning accuracy is only dependent on the time measurement precision, what will be shown in Section 3.

In the TDoA system, the time difference must be calculated in relation to a certain base receiver (BR), assigned index "1" in this work for convenience. The positions of the APs $\vec{r}_{R_j} = [x_{R_j}, y_{R_j}, z_{R_j}]$ are given, and the position of the MU $\vec{r}_T = [x_T, y_T, z_T]$ is unknown. The range difference equation

between BR (R_1) and transmitter (T) and any other receiver (R_j) has the following form:

$$c \cdot \Delta t_{1j} = \Delta d_{1j} = \|\vec{r}_T - \vec{r}_{R_1}\| - \|\vec{r}_T - \vec{r}_{R_j}\|, \quad (1)$$

where the $j = 2, \dots, N$ and N is the total number of APs. As a consequence of this, $N - 1$ linearly independent TDoA equations can be written and combined in a vector matrix

$$\vec{\rho} = [\rho_{12} \dots \rho_{1N}]^T = [\Delta d_{12} \dots \Delta d_{1N}]^T. \quad (2)$$

Like this, the $\vec{\rho}$ is the square root function of the distance differences. The solution can be found by linearizing this function around a starting point $\vec{r}_{T,0}$. The method of choosing the starting point will be described in Section 2.2. After moving the constant terms of the linearized equation to the left side, the following is achieved:

$$\Delta \vec{\rho} = H \Delta \vec{r}. \quad (3)$$

The $\Delta \vec{\rho}$ is the vector of residues, $\Delta \vec{r}$ is the solution vector, and H is the mapping matrix, relating the measured time differences to the differences between starting and calculated position. The least squares solution is in this case

$$\Delta \vec{r} = (H^T H)^{-1} H^T \Delta \vec{\rho}. \quad (4)$$

This iterative method can be continued by using the calculated position as another starting point

$$\vec{r}_T = \vec{r}_{T,0} + \Delta \vec{r} \quad (5)$$

and reperforming this until a breakup criterion is met. This algorithm can only work properly if the equations are not correlated with each other. For a real measurement however, this criterion is not satisfied.

2.1. Problem of the Correlation between Measurements. The reason for the correlation of the TDoA equations is the noise (e.g., thermal noise, receiver noise, and digitization noise). As a result of noise influence, (1) changes to

$$\Delta \tilde{\rho}_{1,i} = \Delta \tilde{d}_{1,i} = (\|\vec{r}_T - \vec{r}_{R_1}\| + w_1) - (\|\vec{r}_T - \vec{r}_{R_j}\| + w_j), \quad (6)$$

where w_j denotes noise term on the j th AP. From this, it is obvious that the measurement noise from the BR is present in all other measurements. This is independent of which receiver is chosen as a reference. Due to this, before calculating the positioning solution, the decorrelation has to be performed first. The measure of the correlation between all the elements of vector $\vec{\rho}$ is its covariance matrix. In a system where all receivers have the same architecture and consist of identical components and the time measurements are performed by the same hardware, the equal noise standard deviation σ_t for all APs can be safely assumed. Under this condition, the covariance matrix is fully occupied

$$R_{\Delta t} = \begin{pmatrix} 2\sigma_t^2 & \sigma_t^2 & \dots & \sigma_t^2 \\ \sigma_t^2 & 2\sigma_t^2 & \dots & \sigma_t^2 \\ \vdots & \vdots & \ddots & \vdots \\ \sigma_t^2 & \sigma_t^2 & \dots & 2\sigma_t^2 \end{pmatrix}. \quad (7)$$

Should this fact be ignored, then for the same measurement a different positioning solution will be obtained every time the BR is changed. The decorrelation, also used in [10], can be done with the Cholesky decomposition of the covariance matrix

$$R_{\Delta t} = LDL^T. \quad (8)$$

The decorrelated matrix D results from the linear combination with L^{-1} ,

$$D = L^{-1}R_{\Delta t}L^{-1,T}, \quad (9)$$

and the measurement vector $\tilde{\rho}$ has to be transformed with the matrix L^{-1} as well,

$$\tilde{\rho}' = L^{-1}\tilde{\rho}. \quad (10)$$

At this point, the decorrelated equation set can be linearized around a starting point, and the new measurement and mapping matrix have the form

$$\tilde{\rho}' = L^{-1} \cdot \tilde{\rho}, \quad (11)$$

$$H' = L^{-1} \cdot H. \quad (12)$$

The solution of (12) with the weighted least squares has the following form:

$$\Delta \vec{r} = (H'^T D^{-1} H')^{-1} H'^T D^{-1} \cdot \Delta \tilde{\rho}' \quad (13)$$

and can be iteratively improved by applying (5). In this section, the method of decorrelating the TDoA measurements was presented with the subsequent solution with the Gauss-Newton algorithm. In the following one, the most efficient algorithm will be chosen.

2.2. Choice of the Best Suited Algorithm. To calculate the MU position from the measurement data, the error function (3) needs to be minimized. It is however not possible to investigate the value of this function for every input argument. Because of this, a number of dedicated algorithms for solving such a nonlinear problems were created. They all follow the same idea: first, a rough estimation of the solution is done, which then can be interpreted as a start point in the error landscape. From this point, a descent direction in the error landscape is calculated. The descent direction is calculated in a way that the reduction of the error function value is highly probable. Subsequently, a first step with a certain step width, from the starting point in the descent direction, is done. A new point is reached and serves as a new starting point to apply the same procedure again, until a stop criterion is met. This can be either the change in the error function or the change in the calculated position. If this value is small enough to assume the stationary condition, a global or local minimum is reached.

In this work, the following algorithms were implemented: Gauss-Newton (GN) with the *quadcubic*-line-search-procedure (qLSP), Levenberg-Marquardt (LM), trust-region-reflective algorithm (TRR), and the interior point (IP). The

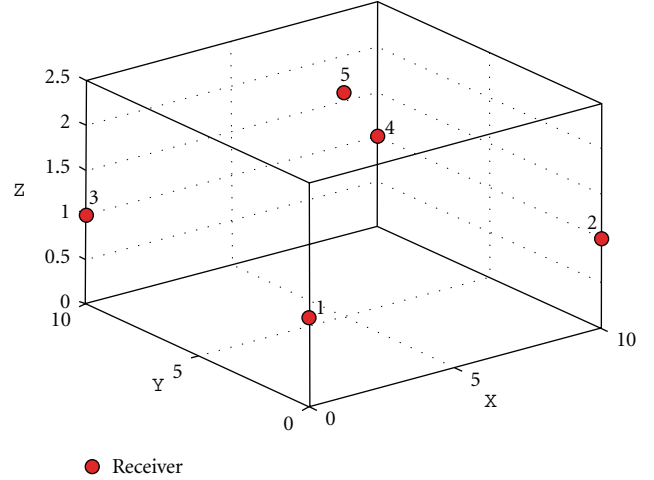


FIGURE 1: Scenario used for evaluation of localization algorithms.

modified Bancroft algorithm (BA) was used as described in [11]. Those algorithms shall now be compared against each other, to state which is the best for the final system. The criteria are the following:

- (i) the mean computation time, calculated as the average of computation times for a set of positions,
- (ii) the accuracy of the solution, where the quality factor is the average 3D positioning error, calculated according to

$$\text{mean 3D error} = \frac{1}{M} \sum_{k=1}^M \left\| \vec{r}_{T_k} - \hat{\vec{r}}_{T_k} \right\|. \quad (14)$$

Because of the fact that some of the evaluated algorithms do not have any additional constrains (e.g., volume in which the feasible solution should remain), large positioning errors can occur. This would largely afflict the average value. For this reason, in addition, the median value will be given.

For the evaluation, an imaginary room with dimensions 10 m/10 m/2.5 m with five APs was used. Four of the receivers were placed in 1 m height in the corners; the fifth one was placed in the middle point of the ceiling. This constellation is depicted in Figure 1. The reason for this AP distribution is explained in Section 3.

The TDoA data for the evaluation was obtained from (6). The measurement noise was modeled as normally distributed, with standard deviation $\sigma_t = 333$ ps (corresponding to $\sigma_d = 10$ cm). The assumption about homoscedasticity of the time error on every AP is made only for the sake of algorithm testing and does not apply during measurements. The MU positions were picked within the scenario boundaries, by a random function with equal distribution. The starting point for the iterative algorithms was chosen by the Bancroft algorithm, to see to which extent the positioning solution improvements are possible. The $M = 1000$ positions calculations were performed. The results are presented in Table 1. As a constraint for the interior-point and Bancroft

TABLE 1: Average 3D error and comutation times of various algorithms.

Algorithm	Average computation time [ms]	3D positioning error mean/median [m]
Bancroft	0.580	0.406/0.312
Gauss-Newton	31.85	0.386/0.276
Levenberg-Marquardt	15.41	0.386/0.276
Trust region reflective	40.96	0.386/0.276
Interior point	98.10	0.311/0.251

algorithms, it was implied that the solution has to be within the room.

The first impression is that the GN delivers good results; however, if the starting point would be picked in random manner and not by BA, the convergence problems occur. From the other algorithms that are left, the BA has the shortest computation time, and its accuracy is smaller than in case of iterative algorithms. The LM and TRR are both in the similar accuracy range; however, the LM requires less computation time. The IP delivers the most precise results; however, this advantage is achieved on cost of the longest computation time from all of the evaluated algorithms.

Based on this result, the best combination seems to be the starting point determination based on the BA and adjacent final calculation with LM. A similar conclusion was drawn in [12]. In case where the additional conditions regarding the geometry should be accounted for, the IP is a good choice.

3. Optimal Access Point Distribution and Accuracy Prediction

If a real system should be deployed, at some point the question about optimal AP placement has to be answered. In order to solve this issue, the question shall be rephrased: “How does an error in a time difference measurement maps to the positioning solution?” The covariance matrix of the measurement vector \vec{p} is defined by

$$R_p = H \cdot R_r \cdot H^T \quad (15)$$

and is related to the covariance matrix R_r of the positioning solution \vec{r}_T . H is the linearized mapping matrix from (3). When this is solved for R_r ,

$$R_r = (H^T H)^{-1} H^T \cdot R_p \cdot H (H^T H)^{-1}, \quad (16)$$

the general expression for mapping of the measurement uncertainty on the localization uncertainty is obtained [13]. In case the signal propagation time measurements have the same variance σ_d^2 , the covariance matrix of the measurement has the form of $R_p = \sigma_d^2 \cdot I$ and (16) reduces to

$$R_r = (H^T H)^{-1} \cdot \sigma_d^2. \quad (17)$$

This is however only valid for uncorrelated measurements. This can be corrected by employing the decorrelated

matrix H' from (12) [14]. The valid form for calculating the localization solution covariance matrix in the TDoA case has the following form:

$$R_r = (H'^T D^{-1} H')^{-1} \cdot \sigma_d^2, \quad (18)$$

where the $(H'^T D^{-1} H')^{-1} = Q$ and Q is due to the performed decorrelation a diagonal matrix. The entries of the diagonal give the DOP values in x -, y -, and z -direction. Those are called XDOP, YDOP, and VDOP (vertical dop). It is also possible to calculate the DOP values for 2D and 3D positions:

$$\text{HDOP} = \sqrt{\sigma_x^2 + \sigma_y^2} = \sqrt{Q_{11} + Q_{22}}, \quad (19)$$

$$\text{VDOP} = \sqrt{\sigma_z^2} = \sqrt{Q_{33}}.$$

The mutual dependence of those values is given by PDOP:

$$\text{PDOP} = \sqrt{\text{HDOP}^2 + \text{VDOP}^2}. \quad (20)$$

Additional information on PDOP can be found [15].

Like this, PDOP, being a function only of T - R coordinates, can be used as a quality measure of a conceptualized T - R constellation. In general, high DOP values indicate poor and small DOPs good T - R configuration. A following example is prepared to gain a better impression of the meaning of this fact. In Figure 2, the distribution of HDOP and VDOP values in a 20 m/20 m/6 m-sized area, for three different constellations of access points, are presented.

Configuration 1 shows 5 receivers placed in 4 m height. HDOP inside of the constellation is in the range of [1.1, ..., 3] and increases up to 9 outside of it. Concurrently, the VDOP stays in the range of [2.2, ..., 6].

The VDOPs can be improved by shifting the middle station out of the plane of all other receivers, for example, 1 m upwards. This situation is depicted in *configuration 2*. The VDOP became better [2.2, ..., 3.5], whereby HDOP did not undergo any significant change.

Another measure for improving the resolution in vertical direction is to involve additional station placed underneath all present receivers. This causes larger measured time differences between two neighbored transmitter positions. This is represented by *configuration 3*. Henceforth, the VDOP is in the range [1.5, ..., 2.3]. It is worth noticing that in all cases the system horizontal accuracy decreases rapidly as soon as the transmitter is outside the receiver constellation. In theory, almost infinite number of different configurations could be tested; however, when considering the practical aspects of base station placement in an average indoor scenario, additional constrains apply. As so, the lineups like in *configuration 3* from Figure 2 should be avoided. Although here the distribution of DOP values is most homogeneous, any station placed on the ground, or slightly above it, will be most likely not visible for MU due to shading effects caused by inside facilities. Because of the mentioned reasons, a similar distribution to this presented in *configuration 2* will be considered further. For practical reasons, during the measurements, a minor modification was undertaken, where the center top AP was shifted slightly to the side.

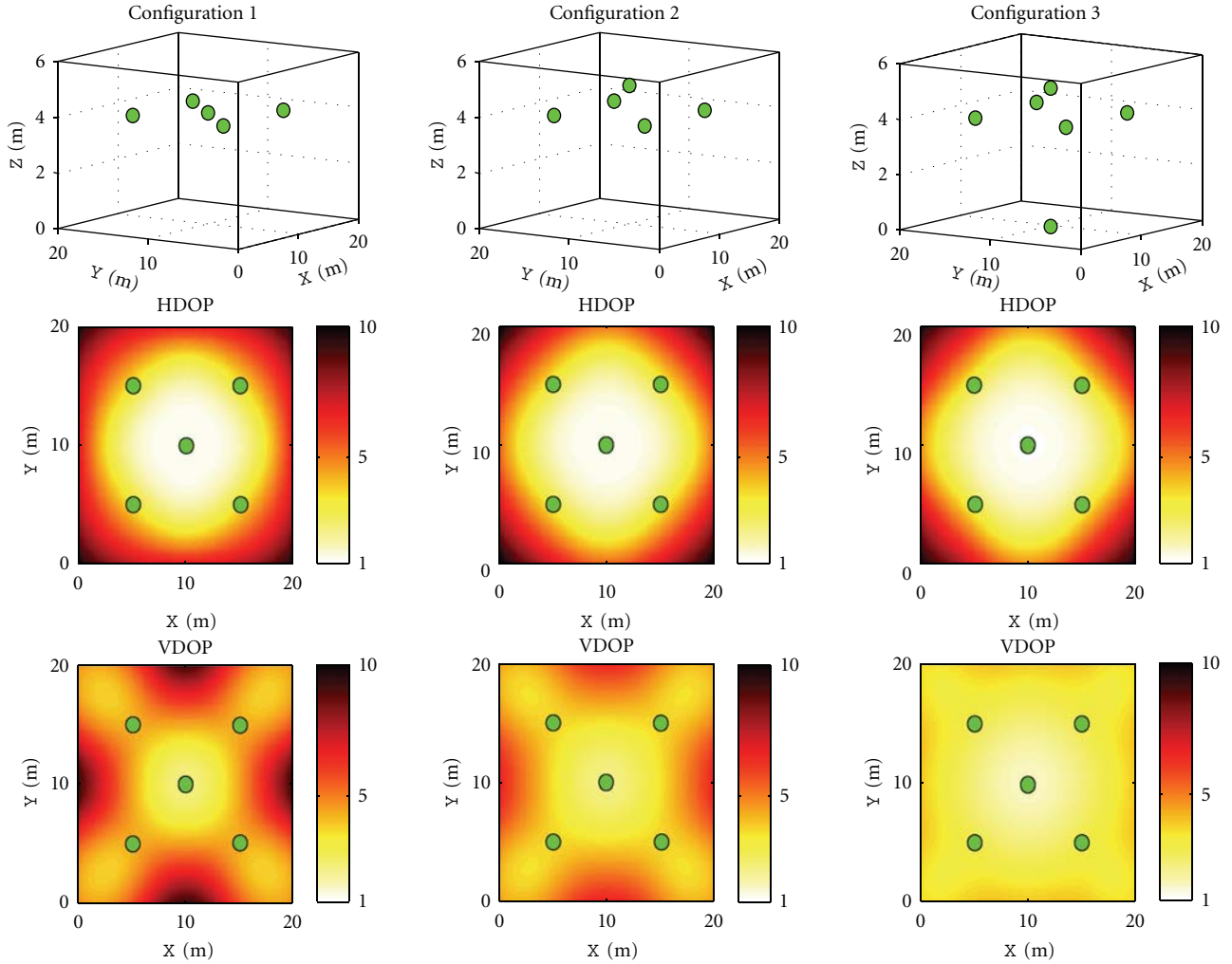


FIGURE 2: Spatial distribution of HDOP and VDOP values for three different access point configurations. The AP positions are marked with green dots.

It has to be mentioned that larger number of base stations would give a rise to more uniform distribution of DOPs and better performance in terms of shadowing; however, the cost of practical implementation would increase.

The very useful information that can be obtained from (20) is the influence of the TDoA measurement error on the localization solution. By knowing the standard deviation of time measurement (σ_{time}) and a PDOP value, the positioning accuracy can be predicted

$$\sigma_{\text{pos3D}} = \sigma_d \cdot \text{PDOP}, \quad (21)$$

where $\sigma_d = \sigma_{\text{time}} \cdot c$, and c stands for speed of light in air. This method can be used for localization quality assessment if the system parameters are known (receiver noise, jitter, and time measurement resolution). More details on the calculation procedure can be found in [16].

4. UWB Hardware and TDoA Setup

4.1. *UWB Demonstrator.* The UWB demonstrator, built for and used in this experiment, consists of an impulse radio

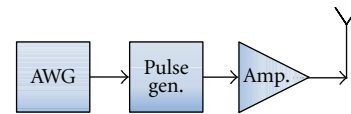


FIGURE 3: Block diagram of the IR-UWB transmitter module.

UWB (IR-UWB) transmitter (Tx) and an autocorrelation-based receiver (ACR). The generic transmitter module, presented in Figure 3, consists mainly of a custom pulse generation- (PG-) integrated circuit (IC) and an of-the-shelf amplifier. The PG can be directly fed with digital data, and each time a falling signal slope is present at its input, a UWB pulse is generated. For this architecture, the achievable data rates span from several kbps up to the lower Gbps region.

The hardware realization of the described transmitter is presented in Figure 4. In the picture, the following elements are visible (starting from the left side): UWB pulse generator [17], amplifier together with a bias tee, variable attenuator, and an omnidirectional antenna (planar monopole).



FIGURE 4: UWB transmit module realized in hardware.

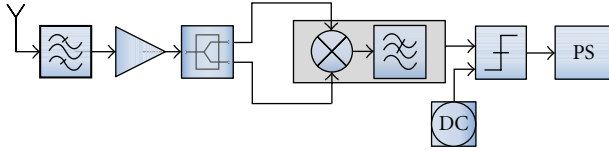


FIGURE 5: Block diagram of the energy detection receiver.

The variable attenuator module (not present in Figure 3) is used to flexibly adjust the amplitude of the transmitted signal, depending on the pulse repetition frequency, to match the FCC spectral emission mask [5].

The UWB receiver (Rx) is presented in Figure 5. After the receive antenna, the signal is band-pass filtered and amplified. Although the arrangement of the filter and the LNA influences the receiver noise figure in a bad manner, out-of-band interference has to be filtered out first to avoid the saturation of the following amplifier. Afterwards, the signal is equally divided and squared. The low-pass-filtered multiplier output is compared with DC threshold, generating a digital signal. The last block is responsible for the signal conditioning.

In Figure 6, the hardware realization of the ACR is illustrated. Starting from the left, the following components are depicted: the directive receive antenna (Vivaldi type), 7th-order microstrip FCC band-pass filter, wideband LNA [18], 3 dB power splitter, UWB correlator module (with an integrated base band amplifier) [19], variable threshold comparator, and the pulse stretcher.

The last module ensures that the receiver output signal (rectangular pulse) has always the same width and amplitude. This is essential for proper operation of the time-to-digital converter (see next section). More information about the performance of the transceiver single building blocks can be found in [20, 21].

4.2. TDC and TDoA Measurement Setup. For the precise time measurements, a time-to-digital converter (TDC) has been used. This device is used to measure the time elapsed between appearance of two (or more) signals at its input ports. First incoming signal generates a *start* and the following ones, the *stop* events. The device of choice for this experiment is the TDC produced by Acam, model ATMD-GPX. This model, depending on the operating mode, is capable of detecting two incoming digital signals with up to 27 ps resolution. A maximum of up to eight input ports can be used.

In Figure 7, a typical system setup for TDoA measurement is shown. The APs are interconnected to ensure



FIGURE 6: Hardware realization of a UWB autocorrelation receiver.

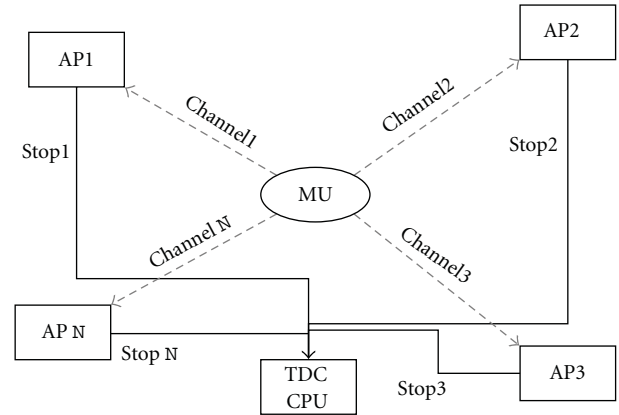


FIGURE 7: Typical TDoA localization system architecture. Synchronized APs receive UWB signals from an autonomous MU, which then are used to calculate its position.

synchronization and an autonomous MU equipped with an UWB tag transmits the impulses. The signals propagate through the scenario on physically different paths (channels) and reach the AP. The received signals from all APs are forwarded to the time measurement unit (TDC) through the synchronization network. The received signals undergo certain delays ($T_{stop N}$) before they trigger the time measurement at TDC. This can be described with

$$T_{meas N} = T_{channel N} + T_{Rx} + T_{stop N} + T_{offset}, \quad (22)$$

where the T_{Rx} stands for the AP-specific delay. T_{offset} originates from the fact that the MU is not synchronized with the APs, and the transmission time point is unknown. The first received impulse triggers the TDC measurement, and the differences to the following impulses are calculated. Such a system requires an initial calibration to determine the T_{Rx} and $T_{stop N}$. After substituting the $T_{meas N}$ into the TDoA equations, the T_{offset} is eliminated.

Due to the limited number of the UWB receivers available for this experiment, the measurements were conducted with one Tx and one Rx unit in a sequential manner. The time measurement procedure for the single MU-AP pair is demonstrated in Figure 8.

In this setup, the (22) is modified and the resulting measured time can be described by following relation:

$$T_{meas N} = T_{trig} + T_{Tx} + T_{channel N} + T_{Rx} + T_{stop} - T_{start}, \quad (23)$$

where the variables have the following meaning: T_{trig} is the delay caused by the triggering cable, T_{Tx} is the time between the trigger enters the Tx and the moment when

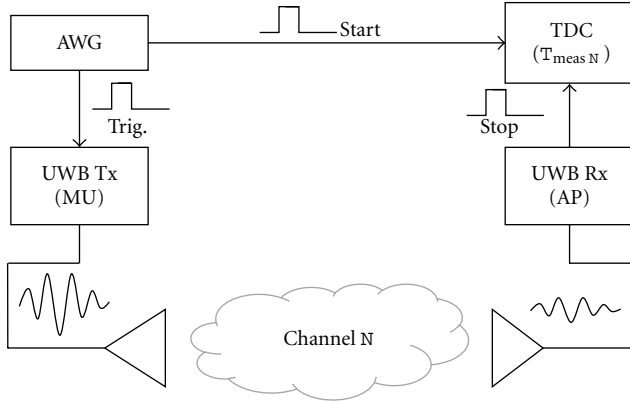


FIGURE 8: Setup for measuring the signal propagation time between MU and AP with the TDC module.

the UWB pulse reaches the transmit antenna, $T_{\text{channel } N}$ is the propagation time through the N th channel, T_{Rx} is the time required by the Rx to process the signal and convert it to digital domain, T_{stop} is the propagation time through a cable to the TDC unit, and finally, the T_{start} is the time after the signal reaches the TDC. In case where the same system components were used for measurements at each AP ($N = 1$ to 5), all the terms in (23), with exception of $T_{\text{channel } N}$, are constant. After building the time differences with $T_{\text{meas } N}$ according to (1), a true TDoA data set is obtained.

5. Sources of Timing Errors

In this section, the sources of inaccurate signal time of arrival measurements will be discussed. They can either originate from passive RF devices in the system or from active digital electronics. The two most critical time error contributions are discussed below.

5.1. Antenna Influence. In the recent years, a significant number of antennas were proposed for different UWB applications. The antenna is one of the most crucial devices in any wireless system. It is responsible for matching the 50 Ohm system impedance (most common) to the free-space impedance. In the ideal case, this would happen without any losses and distortion of the transmitted signal. In practice however, this is never the case. As reported in [22], the influence of the antennas in the UWB transmission cannot be neglected. The different types of broadband radiating devices introduce signal distortions, which in most cases are additionally angle dependent [23]. The parameter that describes the time domain characteristic is the antenna impulse response (AIR). The shape of the AIR and the delay of its maximum can cause an additional offset during the TDoA measurements. According to this, the localization accuracy of the MU will be additionally dependent on the relative angle under which the AP antenna is oriented with respect to the MU.

In the application scenario, described in Section 6, there is no initial information about the MU position. This implies that the signals should be sent/received to/from all directions with equal probability. To reach all APs, the MU antenna

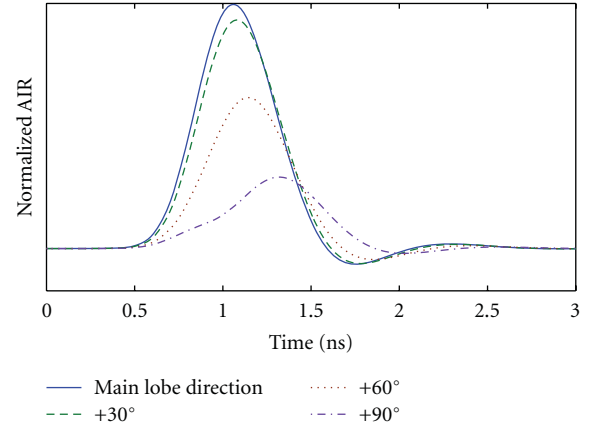


FIGURE 9: Simulation of the angle-dependent impulse response of the applied AP antenna.

should exhibit an omnidirectional radiation pattern. On the other hand, the AP antennas will preferably have a certain directive pattern, to illuminate only a certain part of the scenario.

In the conducted experiment, the mobile user is equipped with an omnidirectional antenna (planar *monopole*), having a uniform characteristic in the horizontal plane (equal pulse distortion). Due to the time difference approach, the influence of the MU antenna can be neglected, because the distortions are the same in each direction. For the AP, antennas with a directive radiation characteristic (*Vivaldi* type) were used. In Figure 9, the distortion of the AP AIR in dependency on angle is visualized. It can be observed that the time shift of the AIRs maximum, during the change of angle (horizontal plane) from the main radiation direction to the perpendicular position, equals 260 ps.

After analyzing the scenario depicted Figures 13 and 14, AP antennas can be oriented in a way that the 90° reception angle would not be needed. However, an additional time delay of up to 200 ps could be introduced, when operated in an angular range of $\pm 60^\circ$. This value corresponds to the distance of 6 cm in the free space. From this, it is obvious that this offset can greatly influence the accuracy of the overall system, aiming for lower subdecimeter accuracy. The method to eliminate the influence of the used antenna is based on an iterative approach and should be presented in the following. The only requirement for this algorithm is the knowledge about spatial orientation of the AP antennas. This can easily be assured during the system deployment phase. The flow chart of this algorithm is depicted in Figure 10.

After obtaining a valid TDoA measurement, the first step is the standard calculation of the positioning solution. This will lead to a first solution, which will serve as a starting point for the iteration. Knowing the approximate MU location, the relative angles between APs reference direction and estimated MU position can be calculated. For those angles, the time correction factors for each AP can be obtained from the lookup table (LUT). The LUT contains the information about the delay of the AIRs peak, relative to the reference direction (e.g., main lobe direction), for all angles.

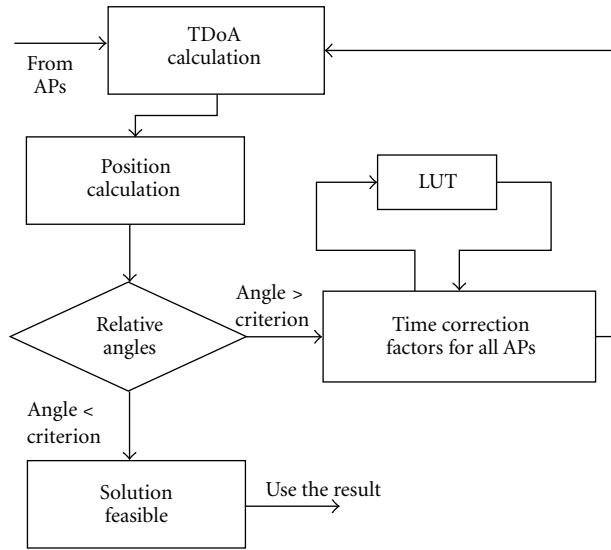


FIGURE 10: Schematic representation of the AIR influence correction algorithm.

After subtracting the correction factors from the original time differences, the new position can be calculated. This operation can be reperformed until a break criterion is met, for example, if the change in the relative angle between two iterations is smaller than a certain value. Other type of criterion would be the change in the calculated positioning solution. The resulting position can now be further used for applications like, for example, tracking.

5.2. Threshold Detection. In every system, there is an interface between analog and digital domain. At this place, both amplitude and time errors can appear. Depending on the digitizing device (comparator or ADC with more than one-bit resolution), the amplitude error will have different values. Obviously, the ADCs with 8 bits, or even more, are capable of transforming the signal into digital domain with only marginal amplitude distortion. The problem with high-resolution ADCs nowadays is their limited bandwidth. Therefore, and because of their cost and power consumption (e.g., pipe-line ADCs consume over 1 W), they will rather not find application in UWB systems for the mass market. Comparators are less accurate, but by far cheaper and seem to be a much better alternative for this application. These devices can achieve bandwidths close to 10 GHz and equivalent input signal rise times of 80 ps [24]. The problem that has to be addressed is the choice of the threshold level. In a scenario with large dynamic range, the trigger time dependency on signal level will play an important role. This is depicted in Figure 11. The use of an adaptive threshold would be the optimal solution; however, this is hardly realizable in practice [25].

The influence of the threshold level in a certain scenario can be mitigated in a similar way as in the case of the AIR. After calculating the initial positioning solution for the MU, the time corrections have to be made. Knowing the exact AP coordinates and the estimated coordinates of the MU,

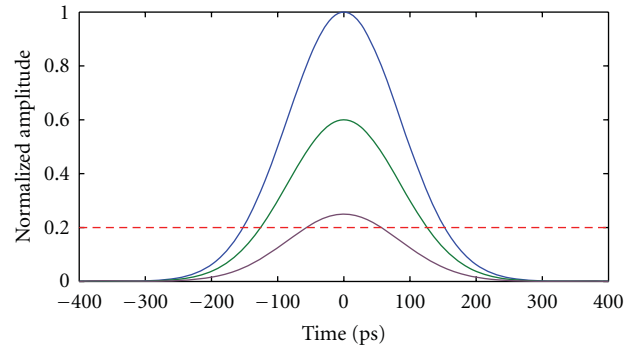


FIGURE 11: Random walk error-trigger time dependency on threshold level.

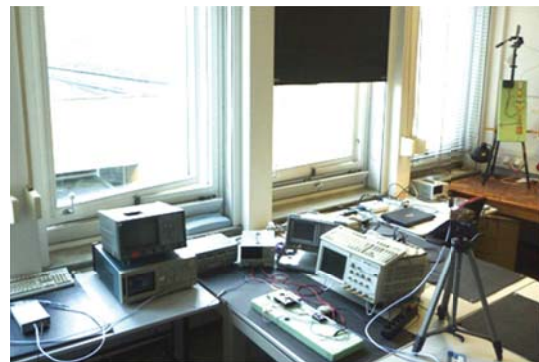


FIGURE 12: Measurement scenario in a laboratory room. An MU antenna placed on the tripod and the AP antenna in the background (top right).

the differences in distances between all AP-MU pairs can be extracted. Distances correspond to signal attenuation (e.g., based on free space path loss), and this is connected with the received signal amplitude. In the LUT, the estimated relative time trigger errors are saved, which are distance difference dependent. The rest of the correction procedure is the same as in Section 5.1.

The trigger time uncertainty of the comparator, caused by electronic jitter, can be modeled as a stochastic process with normal distribution. The influence of this can be minimized by performing averaging [24]. For similar distances, for example, if the MU is placed near to the center of the AP constellation, this effect is negligible. The reason for this is the TDoA procedure, which cancels all common time offsets.

6. Measurement Scenario and Result Analysis

For the measurement verification of the TDoA-based UWB localization system, the laboratory room at the IHE institute was chosen. The size of the room (W/D/H) is 6.3 m/5.9 m/3 m, and all objects, like furniture and lab equipment, were inside during the measurement, representing an average indoor scenario. The photograph of the scenario is shown in Figure 12.

In this environment, two experiments were conducted. The goal of the *experiment 1* (E1) was to determine

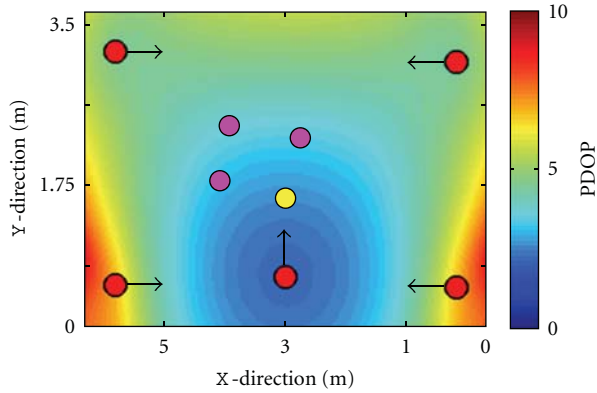


FIGURE 13: Distribution of the PDOP values (top view) in the simulation and measurement scenario. Red dots represent the AP positions. The yellow dot represents the position of the MU from E1, and magenta those from E2. The arrows show the alignment of the antennas in the E2.

TABLE 2: Positions of the T - R units in the scenario in E1.

Unit	x [m]	y [m]	z [m]
AP1	5.955	3.030	2.185
AP2	5.955	0.245	2.202
AP3	0.345	0.265	2.165
AP4	0.345	3.152	2.160
AP5	3.145	0.370	2.860
MU	2.985	1.700	1.400

TABLE 3: Predicted and calculated accuracy for scenarios in E1.

Scenario	Prediction	Accuracy
RT simulation	$5.1 \text{ ps} \cdot 3 \Rightarrow 0.45 \text{ cm}$	0.35 cm
Meas—no avg.	$127 \text{ ps} \cdot 3 \Rightarrow 11.4 \text{ cm}$	11.8 cm
Meas—avg. 50	$32 \text{ ps} \cdot 3 \Rightarrow 2.9 \text{ cm}$	3.6 cm

the achievable positioning accuracy in this environment, comparing the results with the simulation and to validate the method of accuracy prediction. The *experiment 2* (E2) was set up to investigate the influence of the proposed correction algorithms on the positioning accuracy.

6.1. Experiment 1. For validation of the accuracy prediction method, presented earlier in the paper, the system consisting of one MU and five APs was deployed. The positions of the units are listed in Table 2. The same positions were used for the measurement and for simulation.

Based on the positions of the APs, the distribution of the DOP values in the room was calculated. This is presented in Figure 13.

Knowing the method of accuracy prediction (21), a simulation is conducted, to serve as a benchmark for the later measurements. For this purpose, a 3D digital model of the scenario was created, including all the information about objects and their material parameters. In the scenario, the five APs and one MU were placed, at the positions listed in

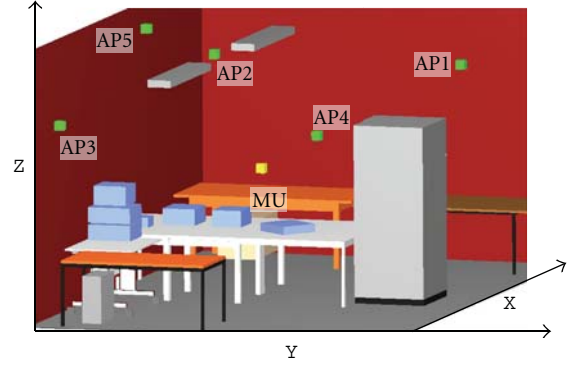


FIGURE 14: Wave propagation (ray tracer) model of the laboratory room, where the measurements were performed. The green points represent the APs, and the yellow one shows the position of the MU during E1.

Table 2. Both the scenario model and the deployed devices are shown in Figure 14. The UWB transmission between all Tx-Rx pairs was investigated by means of a three-dimensional wave propagation simulation based on geometric optics (a high-frequency approximation), which uses material parameters (permeability, permittivity, and surface roughness) (RT: ray tracing) [26]. The simulations provide channel impulse responses (CIRs) and are used to obtain the TDoA data.

The time discretization used during the RT simulation results in the CIR peak time determination inaccuracy σ_{time} of 5.1 ps. Multiplying this value with the calculated PDOP, an inaccuracy of 15 ps (corresponding to 4.5 mm distance) is predicted. The calculated solution exhibits an error of 3.5 mm, which lies close to the predicted limit.

In the performed measurement, the receive antennas were all pointing towards the MU. In the horizontal direction, a small alignment variation of $\pm 5^\circ$ was possible. This fact can lead to an additional positioning error, due to the described AIR angle dependency. The true position of the MU has been determined based on the relative distance measurements to all surrounding walls. This was performed with a laser-based distance measurement device with accuracy of 1 mm.

In the described setup, two data sets have been acquired:

- (i) 1023 unaveraged time measurements at each of the five APs. The measurement exhibited a standard deviation (σ_1) of 127 ps. This originates partially from the TDC performance and from the receivers' comparator;
- (ii) 1023 time measurements with 50 times averaging at each of the five APs. The standard deviation σ_2 of 32 ps is much closer to the specified performance of the TDC.

In Table 3, the summary of all simulations and measurements, performed up to this moment, is shown. The positioning error prediction is based on (21). The third column shows the mean calculated accuracy.

TABLE 4: Positions of the mobile units in E2.

Unit	x [m]	y [m]	z [m]
MU1	2.945	2.335	1.2
MU2	3.71	2.435	1.2
MU3	3.885	1.82	1.2

TABLE 5: Accuracy for no correction and AIR correction.

Unit	Direct TDoA data [m]	100 avg. [m]	100 avg. no outliers [m]	AIR correction [m]
MU1	0.0988	0.0642	0.0327	0.0284
MU2	0.0966	0.0700	0.066	0.0334
MU3	0.0735	0.0343	0.025	0.0135
Average	0.0896	0.0561	0.0412	0.0251

The significant improvement between scenarios 2 and 3 can be explained by the highly reduced comparator trigger error thanks to averaging of the acquired measurements. The reason why during the measurements the errors are slightly larger than predicted is the use of 1σ - and not 3σ -limit. In Figure 15, the calculated MU positions, for the case with averaged time acquisition, are shown. The inaccuracy, resulting from the mean of those solutions, is 3.6 cm.

Overall, this test shows the usefulness of the proposed method of predicting the positioning accuracy, based on PDOP and time acquisition quality.

6.2. Experiment 2. In the second experiment, the effectiveness of the AIR correction method shall be investigated. For this, the same positions of the APs as in the E1 were used. The MU was placed at three different positions in the room to observe the combined influence of antennas and the DOP distribution. The coordinates are listed in Table 4 and depicted in Figure 13. In the same figure, the spatial orientation of the AP antennas can be observed.

In Table 5, the positioning results for all three MUs are shown. In the second column, the solution for direct TDoA data evaluation is shown. In the third column, the positioning result is shown, where the 100-time averaged TDoA measurements were used for localization. In the fourth column, the outliers were removed: from the set of estimated positions the standard dev. was calculated and all values larger than 1σ were not considered. The last column shows the results with performed correction of the antenna influence.

Those results show the effectiveness of the proposed method. The average positioning accuracy improvement, without and with use of the antenna delay compensation method, is 36%. Obviously, the MU1-MU3 were localized with different accuracy; however, this originates solely from the distribution of the DOP values.

7. Summary and Conclusion

In this work, a complete UWB indoor localization demonstrator, dedicated for operation with a predeployed access

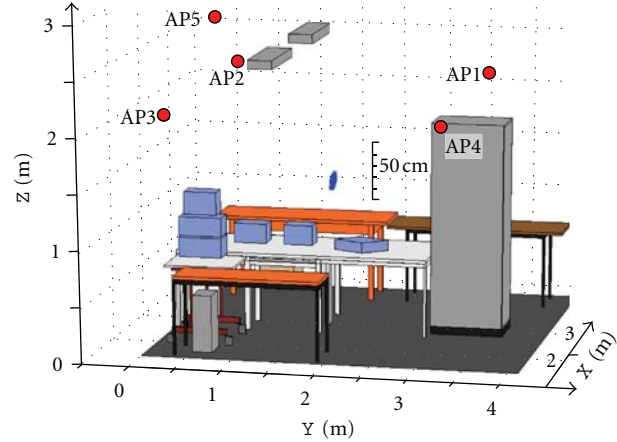


FIGURE 15: The localization solutions (cloud of blue points in the middle) are plotted into the scenario. The TDoA data comes from the measurements.

point infrastructure, has been presented. Different TDoA solution algorithms were implemented and evaluated. The combination consisting of modified Bancroft and Levenberg-Marquardt algorithms was identified as the most efficient one in terms of average computation time and accuracy. Following this, a method of the access point distribution and constellation quality assessment was proposed. Furthermore, a method for positioning accuracy prediction based on time measurement information was derived. The later was then verified based on simulation and experimental measurements in realistic indoor scenario. Additionally, the unwanted influence of the antenna and other system components was described, and algorithms for their mitigation were proposed. This has also been verified by measurement. By applying the methods presented in this paper, the original average accuracy of 9 cm was improved to a value of 2.5 cm. The proposed methods can be universally applied, and their implementation method assures an optimal localization performance, with low-to-moderate computational effort, what is of major importance for future real-time locating systems.

Acknowledgments

The authors would like to thank the Baden-Württemberg Stiftung for financing the work, under the research program “Werkzeuge für die flexible, adaptive Produktion 2007–2011, FKZ: Pro09” and the Institute of Electron Devices and Circuits at the University of Ulm for providing the prototypes of the UWB integrated circuits.

References

- [1] A. Ward, A. Jones, and A. Hopper, “A new location technique for the active office,” *IEEE Personal Communications*, vol. 4, no. 5, pp. 42–47, 1997.
- [2] AT&T Laboratories Cambridge, “Active Bat ultrasonic location system,” <http://www.cl.cam.ac.uk/research/dtg/attachive/bat/>.

- [3] S. Hann, J. H. Kim, S. Y. Jung, and C. S. Park, "White LED ceiling lights positioning systems for optical wireless indoor applications," in *36th European Conference and Exhibition on Optical Communication (ECOC '10)*, September 2010.
- [4] H. Liu, H. Darabi, P. Banerjee, and J. Liu, "Survey of wireless indoor positioning techniques and systems," *IEEE Transactions on Systems, Man and Cybernetics C*, vol. 37, no. 6, pp. 1067–1080, 2007.
- [5] Federal Communications Commission (FCC), "Revision of Part 15 of the Commissions Rules Regarding Ultra Wideband Transmission Systems," First Report and Order, ET Docket 98-153, FCC 02-48; Adopted: February 2002; Released: April 2002.
- [6] Electronic Communications Committee (ECC), "The harmonised conditions for devices using Ultra-Wideband (UWB) technology in bands below 10.6 GHz," Decision (06)04, Approved: March 2006.
- [7] Z. Xiao, G. Tan, R. Li, and K. Yi, "A joint localization scheme based on IR-UWB for sensor network," in *7th International Conference on Wireless Communications, Networking and Mobile Computing (WiCOM '11)*, September 2011.
- [8] G. Fischer, O. Klymenko, D. Martynenko, and H. Luediger, "An impulse radio UWB transceiver with high-precision TOA measurement unit," in *International Conference on Indoor Positioning and Indoor Navigation (IPIN '10)*, Zurich, Switzerland, September 2010.
- [9] A. De Angelis, M. Dionigi, A. Moschitta, R. Giglietti, and P. Carbone, "Characterization and modeling of an experimental UWB pulse-based distance measurement system," *IEEE Transactions on Instrumentation and Measurement*, vol. 58, no. 5, pp. 1479–1486, 2009.
- [10] R. Moenikes, *Verwendung differentieller GNSS-Trägerphasenmessungen zur integrierten hochgenauen Positionierung*, Dissertation, Universität Karlsruhe, Institut für theoretische Elektrotechnik (ITE), 2008.
- [11] L. Zwirello, M. Janson, and T. Zwick, "Ultra-wideband based positioning system for applications in industrial environments," in *3rd European Wireless Technology Conference (EuWiT '10)*, pp. 165–168, Paris, France, September 2010.
- [12] C. Mensing and S. Plass, "Positioning algorithms for cellular networks using TDoA," in *IEEE International Conference on Acoustics, Speech and Signal Processing (ICASSP '06)*, pp. 513–516, Toulouse, France, May 2006.
- [13] I. Sharp, K. Yu, and Y. J. Guo, "GDOP analysis for positioning system design," *IEEE Transactions on Vehicular Technology*, vol. 58, no. 7, pp. 3371–3382, 2009.
- [14] J. D. Bard and F. M. Ham, "Time difference of arrival dilution of precision and applications," *IEEE Transactions on Signal Processing*, vol. 47, no. 2, pp. 521–523, 1999.
- [15] R. B. Langley, "Dilution of Precision," GPS World, May 1999, <http://gauss.gge.unb.ca/papers.pdf/gpsworld.may99.pdf>.
- [16] H. Sairo, D. Akopian, and J. Takala, "Weighted dilution of precision as quality measure in satellite positioning," *IEE Proceedings: Radar, Sonar and Navigation*, vol. 150, no. 6, pp. 430–436, 2003.
- [17] B. Schleicher, J. Dederer, M. Leib et al., "Highly compact impulse UWB transmitter for high-resolution movement detection," in *IEEE International Conference on Ultra-Wideband (ICUWB '08)*, pp. 89–92, September 2008.
- [18] J. Dederer, S. Chartier, T. Feger, U. Spitzberg, A. Trasser, and H. Schumacher, "Highly compact 3.1–10.6 GHz UWB LNA in SiGe HBT technology," in *10th European Conference on Wireless Technology (ECWT '07)*, pp. 327–330, October 2007.
- [19] J. Dederer, B. Schleicher, A. Trasser, T. Feger, and H. Schumacher, "A fully monolithic 3.1–10.6 GHz UWB Si/SiGe HBT Impulse-UWB correlation receiver," in *IEEE International Conference on Ultra-Wideband (ICUWB '08)*, pp. 33–36, September 2008.
- [20] L. Zwirello, Ch. Heine, X. Li, and T. Zwick, "An UWB correlation receiver for performance assessment of synchronization algorithms," in *IEEE International Conference on Ultra-Wideband (ICUWB '11)*, Bologna, Italy, September 2011.
- [21] L. Zwirello, P. Pahl, Ch. Heine, and T. Zwick, "Status Report on the FCC-Compliant UWB Transceiver Implementation," in *6th UWB Forum on Sensing and Communication*, Graz, Austria, May 2011.
- [22] W. Wiesbeck, G. Adamiuk, and C. Sturm, "Basic properties and design principles of UWB antennas," *Proceedings of the IEEE*, vol. 97, no. 2, pp. 372–385, 2009.
- [23] E. Pancera, T. Zwick, and W. Wiesbeck, "Spherical fidelity patterns of UWB antennas," *IEEE Transactions on Antennas and Propagation*, vol. 59, no. 6, pp. 2111–2119, 2011.
- [24] J. Kolakowski, "Application of ultra-fast comparator for UWB pulse time of arrival measurement," in *IEEE International Conference on Ultra-Wideband (ICUWB '11)*, September 2011.
- [25] R. J. Fontana, "Ultra wideband receiver with high speed noise and interference tracking threshold," US Patent 005901172, 1999.
- [26] T. Fugen, J. Maurer, T. Kayser, and W. Wiesbeck, "Capability of 3-D ray tracing for defining parameter sets for the specification of future mobile communications systems," *IEEE Transactions on Antennas and Propagation*, vol. 54, no. 11, pp. 3125–3137, 2006.

Research Article

Performance Analysis of Ultra-Wideband Channel for Short-Range Monopulse Radar at Ka-Band

Naohiko Iwakiri,¹ Natsuki Hashimoto,² and Takehiko Kobayashi²

¹*Nano-Satellite Center, The University of Tokyo, Tokyo 113-8656, Japan*

²*Wireless Systems Laboratory, Tokyo Denki University, Tokyo 101-8457, Japan*

Correspondence should be addressed to Naohiko Iwakiri, iwakiri@nsat.t.u-tokyo.ac.jp

Received 28 October 2011; Accepted 2 February 2012

Academic Editor: Hsiao-Chin Chen

Copyright © 2012 Naohiko Iwakiri et al. This is an open access article distributed under the Creative Commons Attribution License, which permits unrestricted use, distribution, and reproduction in any medium, provided the original work is properly cited.

High-range resolution is inherently provided with Ka-band ultra-wideband (UWB) vehicular radars. The authors have developed a prototype UWB monopulse radar equipped with a two-element receiving antenna array and reported its measurement results. In this paper, a more detailed verification using these measurements is presented. The measurements were analyzed employing matched filtering and eigendecomposition, and then multipath components were extracted to examine the behavior of received UWB monopulse signals. Next, conventional direction finding algorithms based on narrowband assumption were evaluated using the extracted multipath components, resulting in acceptable angle-of-arrival (AOA) from the UWB monopulse signal regardless of wideband signals. Performance degradation due to a number of averaging the received monopulses was also examined to design suitable radar's waveforms.

1. Introduction

Ultra-wideband (UWB) vehicular radars, recently approved by governments of many countries, are expected to be instrumental in reducing traffic accidents [1]. In comparison with conventional vehicular sensing systems using ultrasound, visible and infra-red light, and millimeter waves, Ka-band UWB radar systems hold several advantages, such as no blind angle [2], high-resolution in ranging, weatherproof, and lower price than millimeter-wave radars. Since transmission power of UWB systems is restricted at a level low enough to avoid interference with conventional narrowband systems, UWB vehicular radars are used at short range for collision warning, blind spot detection, parking aid, and precrash control.

During the last decade, there has been much progress on UWB technologies. To understand the behavior of UWB signals, the UWB propagation channel is measured and characterized as described in [3]. Different channel models for practical UWB systems have been proposed in multipath environments [4–6]. Since UWB signals potentially have high resolution in ranging, the different UWB ranging

systems, in multipath environments, have been investigated in [7, 8].

The UWB signals for the vehicular radar have also been measured and modeled in some ways: a generic stochastic uniformly tapped delay line model of multipath UWB channel [9], outdoor channel modeling based on measurements by means of a vector network analyzer [10, 11], and a pulse-based UWB sensor [12]. However, it is insufficient to characterize the behavior of UWB channel signals for short-range monopulse radar at Ka-band, since these works focus on generic modeling below Ka-band. Ranging and direction finding are a key feature of UWB radar systems. Thus, we need to understand these characteristics for Ka-band using a practical analysis method based on measurements.

The authors have developed a prototype UWB monopulse radar equipped with a receive two-element antenna array. The performances of ranging and direction finding by delta-over-sigma (DOS) scheme were evaluated using measurements obtained in a radio anechoic chamber and outdoor environments [13]. However, several problems arise when analyzing the performance of this radar setup. First, the DOS scheme uses sum and differential signals impinging

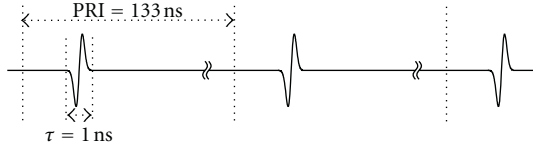


FIGURE 1: Train of transmitted monopulses.

on the two-element array. A predetermined broadside is required for the DOS scheme to estimate angle-of-arrival (AOA) even if the radar moves toward different directions. Moreover, the DOS scheme specialized to a two-element array makes it impractical as an implementation for general multielement antenna array.

Since the measurements were conducted with independent reception for DOA scheme at each of the two-element array, the prototype UWB monopulse radar could not be collected enough of received signals. We, therefore, developed an analysis technique to model UWB monopulse signals by focusing on two ways to understand characteristics of ranging and direction finding, regardless of some constraints. First, the measurements were analyzed to characterize the behavior of multipath components from a target contained in the received signals. Next, instead of applying the DOS scheme, conventional techniques of pulse compression for ranging and multiple signal classification (MUSIC) or minimum variance distortionless response (MVDR) algorithms for direction finding were adopted to evaluate the applicability in UWB vehicular radars. The obtained results provide insight into UWB monopulse radar design.

The rest of this paper is organized as follows: modeling multipath components is discussed in Section 2. Experimental verification of the prototype radar from measurements in a radio anechoic chamber is described in Section 3. Performance analysis of the UWB monopulse signals in outdoor environments is presented in Section 4. Finally, the conclusions are drawn in Section 5.

2. Modeling Multipath Components

The UWB monopulse radar can resolve more multipath components than conventional narrowband radar systems because of its high resolution in ranging. Moreover, the AOA of each of the components is obtained if multiple-element antennas are adopted and conventional direction finding algorithms are available. However, an optimum analysis scheme for the received signal is required to design reliable UWB radar systems with acceptable performance. We then derive the detection scheme for resolvable or nonresolvable multipath components within received UWB monopulse signals.

2.1. Resolvable Multipath Components. A train of transmitted monopulses demonstrated in this work is shown in Figure 1. There is a single monopulse in each pulse repetition interval (PRI). The signal impinging on the target and the reflected signal observed by the receive array are assumed to be

plane waves in a static channel. If M signals impinge on the L -element array from distinct AOAs, the received signal commonly used in array processing is given by [14]

$$\mathbf{x}(t) = \mathbf{A}(\boldsymbol{\theta})\mathbf{s}(t) + \mathbf{n}(t), \quad (1)$$

where a steering matrix $\mathbf{A}(\boldsymbol{\theta})$ and a vector of signal waveforms $\mathbf{s}(t)$ are defined by

$$\begin{aligned} \mathbf{A}(\boldsymbol{\theta}) &= [\mathbf{a}(\boldsymbol{\theta}_1), \dots, \mathbf{a}(\boldsymbol{\theta}_M)], \\ \mathbf{s}(t) &= [s(t), \dots, s_M(t)]^T. \end{aligned} \quad (2)$$

Assuming a uniform linear array (ULA) having interelement spacing of d , a steering vector $\mathbf{a}(\boldsymbol{\theta}_m)$ can be written by

$$\mathbf{a}(\boldsymbol{\theta}_m) = [a_1(\boldsymbol{\theta}_m), \dots, a_L(\boldsymbol{\theta}_m)]^T, \quad m = 1, \dots, M. \quad (3)$$

For the plane wave case, l -th elements at the AOA $\boldsymbol{\theta}_m$ are given by

$$a_l(\boldsymbol{\theta}_m) = e^{-j(l-1)(2\pi/\lambda)d \sin \theta_m}, \quad l = 1, \dots, L, \quad (4)$$

where λ is wavelength.

The received signals are assumed as discrete signals, and then the received signal matrix per PRI can be written as

$$\mathbf{X} = [\mathbf{x}(1), \dots, \mathbf{x}(N_{\text{pri}})], \quad (5)$$

where N_{pri} is a number of signal samples per PRI. A pulse compression can be carried out for each element output to detect multipath components passed through a matched filter. This output of l -th element is simply the inner product between received signals of l -th element and replica signals, namely, pulse compression [15], as given by

$$r_l(n) = \mathbf{X}_l(t_n) \cdot \mathbf{h}, \quad (6)$$

where $t_n = n+1, n+2, \dots, n+N_{\text{pri}}-N_{\text{seq}}, n = 0, 1, \dots, N_{\text{pri}}-N_{\text{seq}}$, and \mathbf{h} is a complex conjugate column vector of the replica signal with length of N_{rep} . Thus, all of the $N_{\text{pri}}-N_{\text{seq}}+1$ outputs are obtained for each PRI, and then the outputs of the l -th element are averaged over N_{ave} PRIs:

$$\bar{r}_l(n) = \frac{1}{N_{\text{ave}}} \sum_{a=1}^{N_{\text{ave}}} r_{l,a}(n). \quad (7)$$

Finally, k th multipath components can be extracted to choose the signal strength higher than the optimum threshold γ , as given by

$$|\bar{r}_l(n_k)| > \gamma, \quad k = 1, 2, \dots, K, \quad (8)$$

where n_k is a delay sample from the PRI boundary of the k -th multipath components. Therefore, for a static environment, the total of K peaks can be related to the resolvable multipath components.

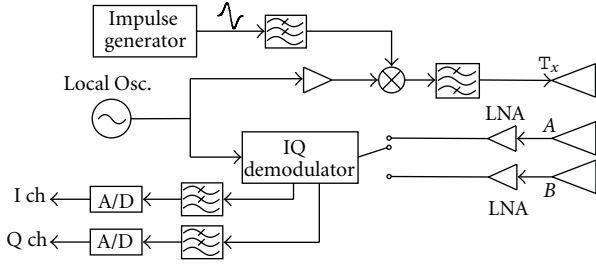


FIGURE 2: The block diagram of the prototype radar transmitter-receiver.

2.2. Nonresolvable Multipath Components. We next consider how to detect nonresolvable multipath components. The sample covariance matrix is calculated using $2N_{\text{smp}} + 1$ samples around k -th resolvable multipath components:

$$\mathbf{R}_k = \frac{1}{2N_{\text{smp}} + 1} \mathbf{X}(n_i) \mathbf{X}^H(n_i), \quad (9)$$

where $n_i = n_k - N_{\text{smp}}, n_k - N_{\text{smp}} + 1, \dots, n_k, \dots, n_k + N_{\text{smp}}$.

Up to this point, an arbitrary number of array elements have been discussed. In subsequent discussions, we focus on an $L = 2$ case since a two-element array was implemented in our prototype radar system. Two eigenvalues λ_1 and λ_2 can be obtained from eigendecomposition of \mathbf{R}_k , because \mathbf{R}_k is guaranteed positive definite due to Hermitian matrix. There are three types of eigenvalue distribution: $\lambda_1 \geq \lambda_2 > \sigma^2$ when two or more signals having different AOAs impinging on the receive array, or a single AOA cannot correctly resolve owing to inadequate accuracy of the elements in \mathbf{R}_k , where σ^2 is a noise variance; $\lambda_1 > \lambda_2 = \sigma^2$ when a single signal impinges on the receive array; $\lambda_1 = \lambda_2 = \sigma^2$ when none of signals is received.

Nonresolvable multipath components within each multipath component will be estimated from this classification because of the Nyquist rate. The basic idea is to find a criterion of nonresolvable multipath components from measurements collected in a single-path environment realized in radio anechoic chamber. The criterion can be obtained to apply the second type of eigenvalue distribution. Specifically, the nonresolvable multipath component can be estimated if λ_2 is larger than the boundary, since a boundary between resolvable and nonresolvable multipath components is determined from the distribution of λ_2 . Hence, the behavior of a multipath component in outdoor environments is characterized when using a passenger vehicle as a target. This criterion can be easily extended to an array having elements more than 2.

3. Anechoic Chamber Experiments

3.1. Experimental Setup. The block diagram of a prototype Ka-band UWB pulse radar is depicted in Figure 2, which is the same system as our previously published work [13], except that the received signals were directly input to an IQ demodulator without passing through a coupler. The experiment was set for a single-path environment in a

TABLE 1: Specification of experiments.

Waveform	Modulated Gaussian monopulse
Pulse duration	1 ns
Frequency bandwidth	24.0–29.0 GHz
Sampling rate	10 or 20 Gsps
Antennas	Slot antennas
Polarization	Vertical-vertical
Element spacing	5.4 mm
Spectrum density of average emission	< -44 dBm/MHz

radio anechoic chamber. The measurements were analyzed to obtain parameters required to characterize resolvable or nonresolvable UWB monopulse signals in outdoor environments. Gaussian monopulse has been widely adopted for UWB systems to satisfy FCC spectrum mask regulations [16]. Various practical monopulse design techniques have been developed in [17–19]. The performance of these design techniques has also been analyzed in different ways: principle of space-time array processing [20], target recognition reflected on different obstacles [21], and position estimation [22]. We also adopted Gaussian monopulse due to its ease of use with our analysis methods. An arbitrary waveform generator with a sampling rate of 25 GHz was used as an impulse generator.

In the first experiment, a trihedral corner reflector was used as a target, comprising three right-angled isosceles triangles with 210 mm long sides. Its radar cross section was approximately 191 m². The reflector was placed at a distance of 2.8 m from the radar. The radar was rotated from -30° to 30° in intervals of 1° , and then received signals were recorded. A direction of 0° was defined as broadside of the two receive antennas. Transmit and receive antennas were slot antennas with vertical polarization. The impulse generator outputs baseband Gaussian monopulse trains with monopulse duration of 1 ns occupying a bandwidth of 2 GHz, as shown in Figure 3. The trains are upconverted through RF modules by a carrier frequency of 26.5 GHz and emitted from the transmitting antenna. The spectrum density of the average emission in this band was selected less than -44 dBm/MHz to satisfy FCC regulations [1]. Each received signal impinging on the two-element array is down-converted to baseband by the IQ demodulator, analog-to-digital converted at a sampling rate of 10 or 20 Gsps, and then recorded in a digital storage oscilloscope (DSO). The transmitted and received UWB monopulse signals are shown in Figures 3(a) and 3(b), respectively. The latter is distorted due to mismatching in the RF components. Major parameters of the experiment are listed in Table 1.

The above setup is capable of collecting data of the single path impinging on a horizontally placed two-element array with half-wavelength element spacing. The received signal performance and the results for analyzing the measurements are described in the next section.

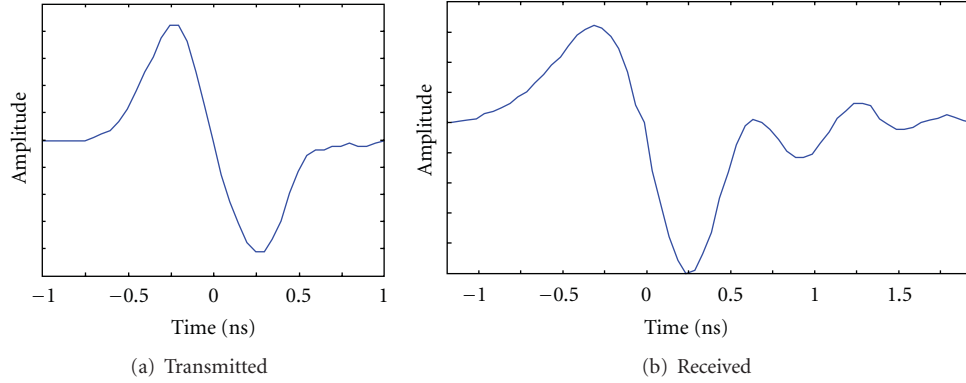


FIGURE 3: Baseband monopulse waveforms.

A received signal power typically attenuates as the distance between the radar and the target increases. Hence, resolution accuracy of ranging and direction finding will depend on the received power. A technique that averages received monopulses is useful to increase received signal gain without increasing transmit power. We then estimated the resolution accuracy by evaluating the different numbers of averaging monopulses at the receiver. The result is discussed in Section 4.5.

3.2. Performance Analysis. Received multipath components, after averaging over 10^4 PRIs, were extracted by pulse compression, as given by (7). The reference signals of the matched filter used for both the I and Q channels were the received monopulse signal shown in Figure 3(b). The pulse-compressed output when the radar is directed to 0° is shown in Figure 4, where a single sharp peak is observed. The plot shows that the number of averaging 10^4 PRI is sufficient to extract a single peak from the noisy received signals, and the outputs directed to the other angles also have a single peak. However, since the antenna pattern is not isotropic, the peak strength decreases as the direction moves away from broadside. The peak strength from -30° to 30° is shown in Figure 5.

Next, the covariance matrix \mathbf{R} and its eigenvalues were calculated for each extracted peak, as described in Section 2.2. To collect more samples around the peak, $N_{\text{smp}} = 2$ (total 5 samples) was selected for 20 Gsps sampling. The obtained 61 pairs of eigenvalues λ_1 and λ_2 were then normalized by λ_1 . The eigenvalue distribution shown in Figure 6 revealed that all the λ_2 are sufficiently smaller than unity regardless of direction. It is thus concluded that λ_1 is a signal or resolvable component and λ_2 is a noise or nonresolvable component, and its boundary is 10^{-1} . This boundary will be used as the criterion of detection of nonresolvable multipath components in the outdoor experiments, as described in Section 4.2.

Finally, the AOA was estimated for each of the extracted peaks using MUSIC algorithm [14] to verify its applicability to the UWB monopulse signals. The obtained AOAs are plotted in Figure 7. The two regression curves corresponding

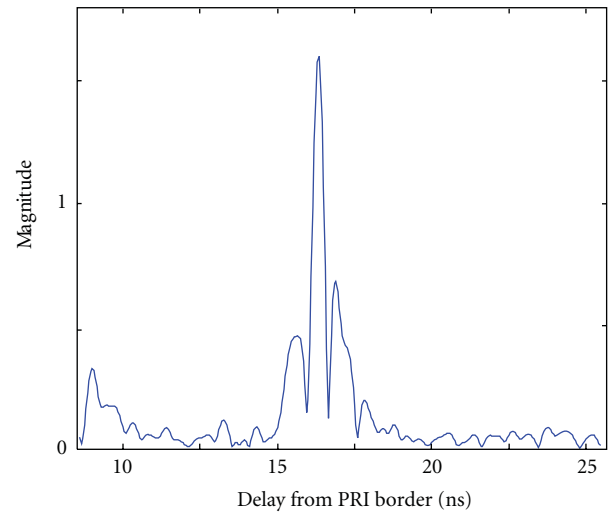


FIGURE 4: Pulse-compressed output signals from broadside in anechoic chamber experiments.

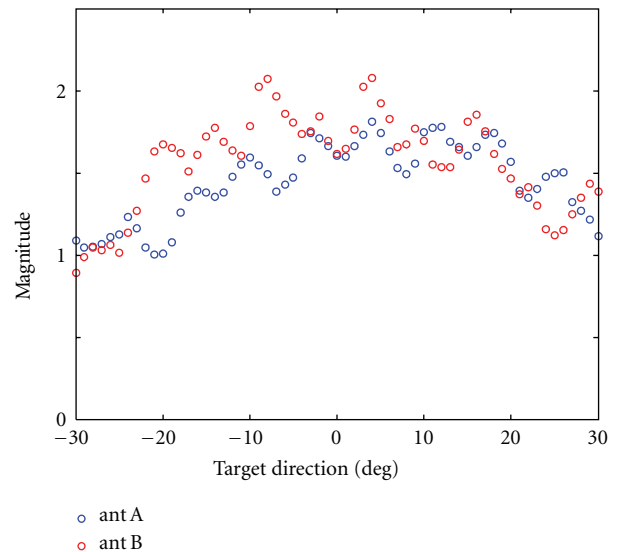


FIGURE 5: Magnitude of extracted multipath components corresponding to different angles in anechoic chamber experiments.

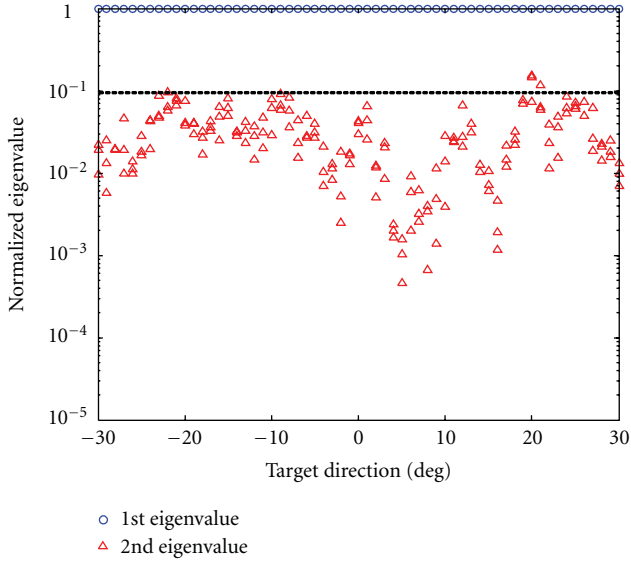


FIGURE 6: Normalized eigenvalue distribution derived from the measurements in anechoic chamber experiments.

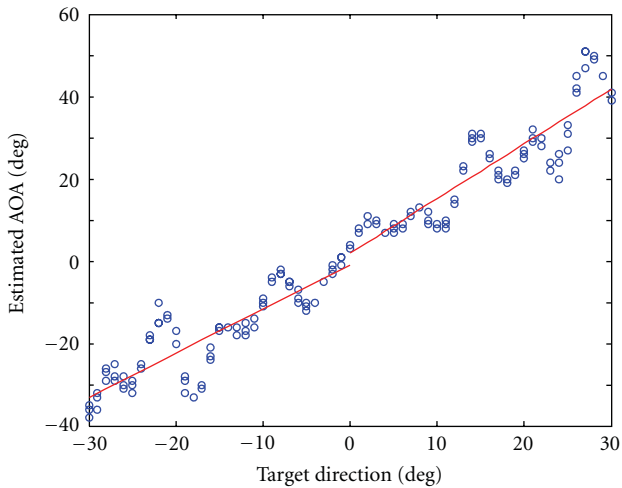


FIGURE 7: Estimated AOA by MUSIC derived from the measurements in anechoic chamber experiments.

to plus and minus angles are also plotted by solid lines. The plot shows that the MUSIC algorithm can be utilized for UWB signal with monopulse duration of 1 ns and carrier frequency of 26 GHz. This result can prove that the carrier-to-baseband frequency ratio of 26 is sufficient for the conventional direction finding algorithm regardless of the UWB signals.

4. Outdoor Experiments

4.1. *Experimental Setup.* The next experiment was conducted in outdoor environments. A four-door sedan, 4.73 m long, 1.80 m wide, and 1.44 m high, was used as a radar target in the outdoor experiment. The vehicle, parked on a broadside, is shown in Figure 8. The different locations



FIGURE 8: A radar target on a broadside in outdoor experiments.

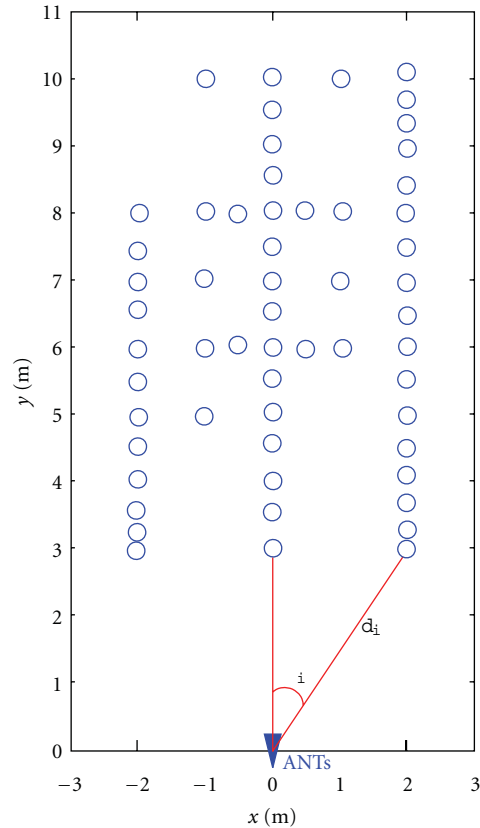


FIGURE 9: 57 locations of a target vehicle in outdoor experiments.

of the target vehicle are illustrated in Cartesian coordinates (x, y) in Figure 9. Placing the radar at the origin of the center lane, the vehicle was parked at 57 locations between the left, center, and right lanes. The 57 locations were corresponded to a target direction with an azimuth angle θ_i between -42° and $+42^\circ$ and a target distance d_i from 2.9 m to 10 m away from the origin, where $i = 1, \dots, 57$. The center of the rear bumper was used to define the target direction and distance, since the transmitted signals mainly impinged on the back of the target vehicle. The height of the radar antennas was

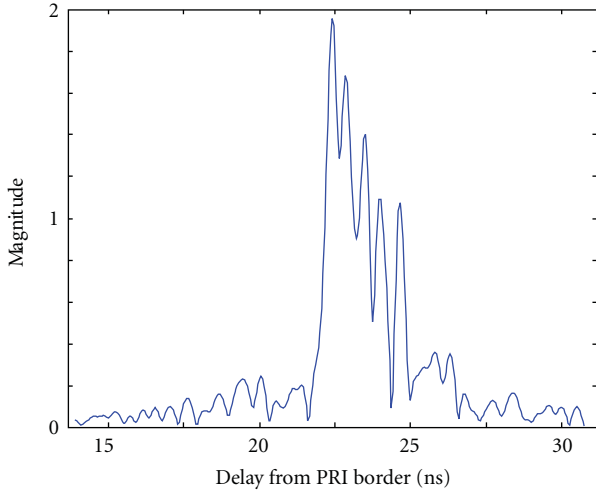


FIGURE 10: Pulse-compressed output signals from broadside in outdoor experiments.

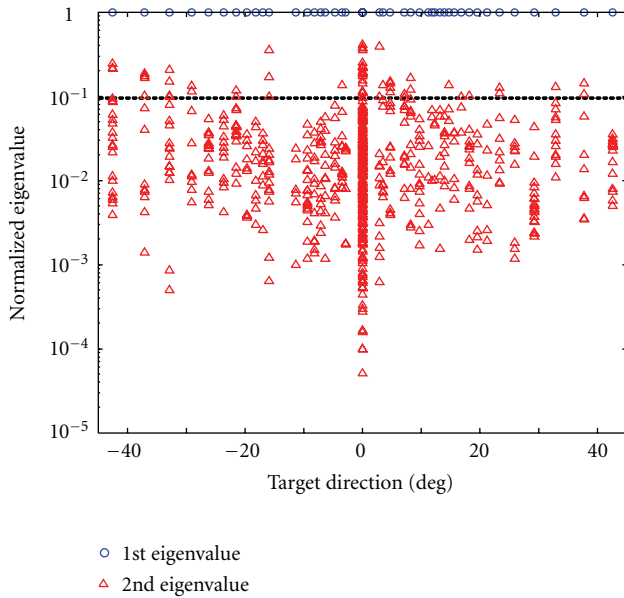


FIGURE 11: Normalized eigenvalue distribution derived from the measurements in outdoor experiments.

0.6 m, which was the same as that of the rear bumper. Effects of surrounding trees and buildings were negligible because the signals reflected from the vehicle were dominant in this setup.

Since there were no obstructions between the radar and the target vehicle, the channel model associated with this setup is line-of-sight (LOS) channel. Assuming a narrow-band signal, the LOS path is given by a single propagation path because of low time resolution that is less than the inverse of the signal bandwidth. Whereas for the UWB signal, multipath components reflected from the target can be resolvable, so that every resolvable delay bin does not contain multipath components [3]. Moreover, the multipath components impinging on the antenna array are confined to

small angle and delay corresponding to the target vehicle. This implies that the collected measurements are no longer treated as the specific channel models. We then characterize the UWB channel as the delay bin having either resolvable or nonresolvable multipath components, as described in the next section.

4.2. Resolvable/Nonresolvable Multipath Components. Multipath components were extracted for received signals by pulse compression given by (7). The obtained pulse-compressed output from the broadside and at a distance of 3.6 m, namely, power delay profile, is shown in Figure 10. The resolvable multipath components were extracted to select the K largest peaks as in (8) and then classified as three regions with respect to the lane of the parked vehicle: the left with minus angle, the center with the broadside, and the right with plus angle. The extracted number of multipath components was averaged over each region. The mean value on the broadside was the largest value at 5.1, while those in the left and right regions were, respectively, 3.0 and 4.1. This is because when the multipath components arriving from different directions have the same delay, the signal strength on the broadside is higher than that in the other regions, as shown in Figure 5. Therefore, the number of extracted peaks, depending on signal strength, decreases as the target direction moves away from the broadside.

Next, the nonresolvable multipath components within the extracted resolvable multipath components were evaluated. Setting $N_{\text{smp}} = 2$ and calculating the covariance matrix \mathbf{R} as described in Section 2.2, two eigenvalues λ_1 and λ_2 were obtained by eigendecomposition of \mathbf{R} . The eigenvalue distribution normalized with λ_1 is illustrated in Figure 11. It is observed that some of eigenvalues λ_2 are larger than 10^{-1} ; the detection boundary was described in Section 3.2. Thus, the resolvable multipath component having λ_2 larger than 10^{-1} can be defined as a nonresolvable multipath component, as described in Section 2.2.

The number of nonresolvable components was also averaged in each region, and then the ratio of the number of nonresolvable components to that of resolvable components was calculated. The obtained ratios in the left region, on the broadside, and in the right region were 7.6%, 8.7%, and 6.9%, respectively. The nonresolvable multipath components are observed to concentrate on the broadside. This is because the multipath components, having a smaller delay than the monopulse duration of 1 ns, tend to impinge on the receive array when the array is placed parallel to the four sides of the vehicle. In this experiment, a vehicle located on the broadside is parallel to the receive array, as shown in Figure 8.

4.3. AOA Estimation. The AOA was also estimated for each extracted peak using the MUSIC and the MVDR algorithms [8] used in the second experiment. The AOAs for the MUSIC versus the target direction are illustrated in Figure 12. A similar plot is obtained by MVDR algorithm. The two regression curves calculated from the anechoic chamber experiments are also plotted by solid lines. Note that the AOAs from the right region have an offset from the regression

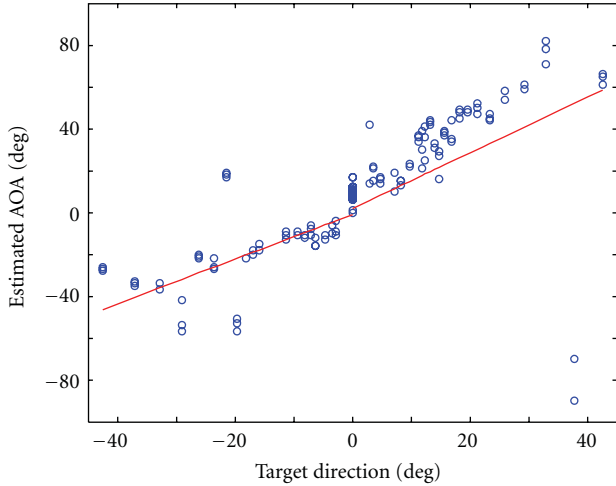


FIGURE 12: Estimated AOA by MUSIC derived from the measurements in outdoor experiments.

curve; this may be attributed to antenna misalignment. It can be seen that the AOAs from the target direction between -20° and $+20^\circ$ are close to the regression curves. Because of the resolution limitation caused by the two-element array and the anisotropic antenna radiation pattern, the number of outliers increases as the target angle moves away from the broadside.

4.4. Ranging and Multipath Spread. A UWB signal enables precision ranging capabilities because of a time resolution on the order of 1 ns [23]. The ranging of each location is obtained by finding the largest peak in the measured power delay profile. This approach is similar to a threshold-based energy detector-based time-of-arrival estimator [7] because a preamble structure resembles the transmitted pulse trains as shown in Figure 1. Since the delay from the PRI boundary to the largest peak is round-trip time between the origin and the target vehicle, the ranging is obtained from half of the delay time, as given by

$$\hat{d}_i = \frac{cT_i}{2}, \quad i = 1, 2, \dots, 57, \quad (10)$$

where c is the light velocity and T_i is the delay bin of the i th location. Each reference distance between the origin and the i th location was measured from the receive array to the center of the vehicle on the rear bumper. The standard deviation of the ranging errors at each location versus the target distance is shown in Figure 13. The ranging resolution of 0.15 m corresponding to the monopulse duration of 1 ns is also plotted in a solid line. A single outlier more than the ranging resolution of 0.15 m is observed regardless of the shortest target distance. This phenomenon is also explained by the magnitude of extracted multipath component, as shown in Figure 5. Since the magnitude decreased as the target direction moved away from the broadside, the multipath component corresponding to the rear bumper center could not be precisely extracted at the location with the largest target direction. In other words, the largest peak of measured

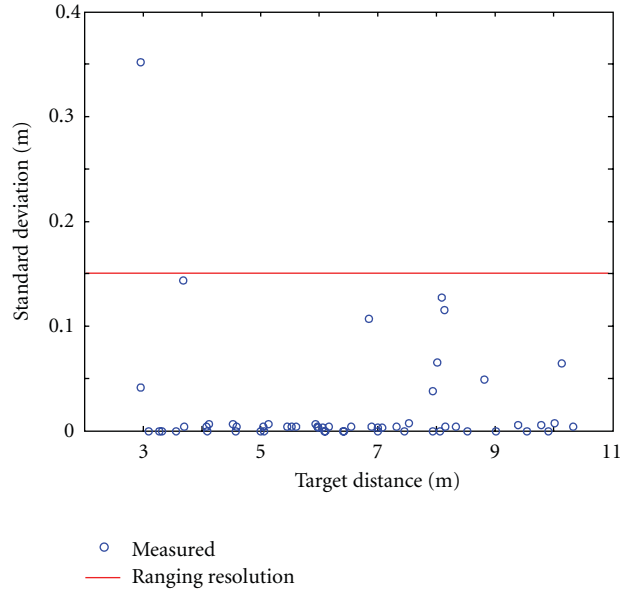


FIGURE 13: Standard deviation of ranging errors in outdoor experiments.

power delay profile did not always arrive from the rear bumper center when the target vehicle moved away from the broadside.

Thus, it seems intuitive that the obtained power delay profile from the target vehicle contains mostly reflected path components around the rear bumper center. We next estimate the propagation paths arriving from the target vehicle, and then define a multipath spread of the profile as a difference between the shortest and the largest arrival distances of multipath components to estimate the reflection point corresponding to each multipath component. The multipath spread of each target location is a plotted 3D graph, as shown in Figure 14. The resulting spread on the broadside ranges from 0.29 to 0.5 [m], so the distance is too long to generate the power delay profile from only directly reflected path components from the rear bumper. Therefore, from the rear surface of the vehicle shown in Figure 8, the reflection points of multipath components may include the pillar and roof as well as the bumper and the ground reflection path as well as the direct path. On the other hand, the multipath spread in the left and right regions tend to decrease as the target distance increases and target angle moves away from the broadside. This is mainly due to two reasons. First, since the side of the vehicle enables to contribute the reflection, the width of probable reflection surface increases as target angle moves away from the broadside. Second, the width of probable reflection surface on the vehicle decreases in proportion to distance and then more than one multipath component with almost the same delay tends to fall in a single peak.

4.5. Effect of Number of Averaging PRIs. The analyses so far has used the measurements with the averaging of 10^4 PRIs and a sampling rate of 20 Gsps. The number of PRIs is an

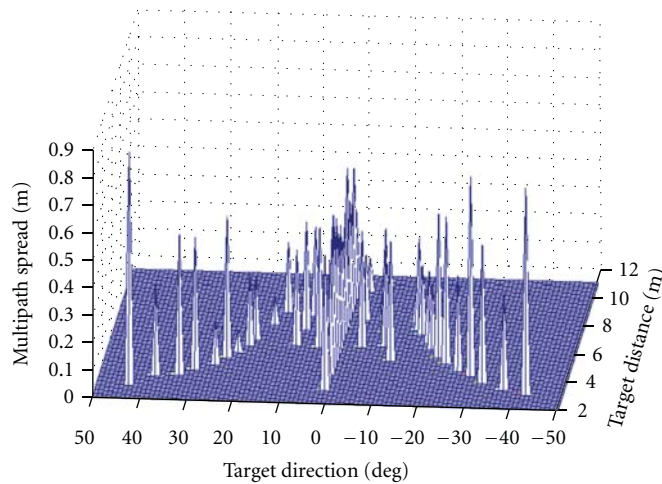


FIGURE 14: Multipath spread from a target vehicle in outdoor experiments.

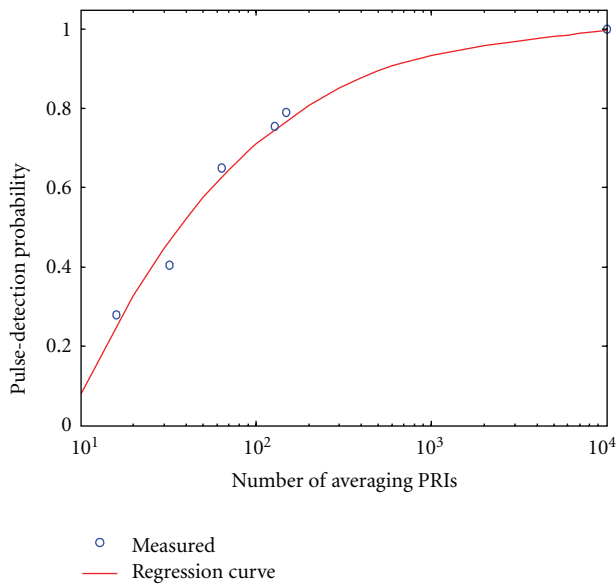


FIGURE 15: Pulse-detection probability versus number of averaging PRIs in outdoor experiments.

important parameter to improve accuracy of practical radar systems. The signals of each PRI were also recorded on the DSO with a sampling rate of 10 Gsps at the locations, as shown in Figure 9. The recorded signals were averaged over N_{ave} PRIs, where $N_{ave} = 16, 32, 64, 128,$ and 149 , since the maximum number of PRIs was 149 owing to the limitation of memory size on the DSO with 10 Gsps sampling. Note that when calculating \mathbf{R} , $N_{smp} = 1$ (total 3 samples) was selected for 10 Gsps sampling.

For the measurements of 20 Gsps sampling, the ranging accuracy was verified as described in Section 4.4. We then define a ratio of correctly estimated ranging at each location as a pulse-detection probability. For example, the pulse-detection probability for averaging of 10^4 PRIs was unity, since the estimated ranging error was zero. The resulting

pulse-detection probability versus the averaging N_{ave} is plotted in Figure 15. The regression curve is also plotted. The probability increases with N_{ave} because of improvement of signal-to-noise ratio by averaging. The AOAs were next evaluated using only the multipath components corresponding to the correctly estimated ranging. However, almost all AOAs are not accurately estimated for N_{ave} less than or equal to 128. These results show that the level of the extracted peak after the pulse compression is generally below that of noise and thus; time average cannot converge to the true mean value.

5. Conclusions

This paper has presented the multipath resolution and direction findings of a UWB monopulse radar equipped with a two-element array. We cannot perform more detailed analyses owing to experimental limitations, such as the number of array elements, the number of monopulses per PRI, the received monopulse distortion, and measuring in static environment only. However, since the obtained results are useful parameters for performance analysis by computer simulation, a more practical UWB monopulse radar with multiple-element array will be designed. Moreover, the proposed estimation methods for resolvable/nonresolvable multipath components will be a valuable tool for any other UWB monopulse radars. The number of averaging monopulses is an important parameter for accuracy of ranging and direction finding. However, the observations must be corrected in static or quasistatic environments. Therefore, for practical use, a number of monopulses per PRI, sampling rate, and multiple-element array must be considered to increase the number of observations as quickly and accurately as possible.

Acknowledgment

This paper was supported in part by Grant-in-Aid for Scientific Research (C) KAKENHI 22560430.

References

- [1] I. Gresham, A. Jenkins, R. Egri et al., "Ultra-wideband radar sensors for short-range vehicular applications," *IEEE Transactions on Microwave Theory and Techniques*, vol. 52, no. 9, pp. 2105–2122, 2004.
- [2] T. Kobayashi, N. Takahashi, M. Yoshikawa, K. Tsunoda, and N. Tenno, "Measurement of automobile UWB radar cross sections at Ka band," in *Ultra-Wideband, Short-Pulse Electromagnetics 7*, F. Sabath, E. L. Mokole, U. Schenk, and D. Nitsch, Eds., pp. 586–592, Springer, New York, NY, USA, 2007.
- [3] A. F. Molisch, "Ultra-wide-band propagation channels," *Proceedings of the IEEE*, vol. 97, no. 2, pp. 353–371, 2009.
- [4] Q. T. Zhang and S. H. Song, "Parsimonious correlated nonstationary models for real baseband UWB data," *IEEE Transactions on Vehicular Technology*, vol. 54, no. 2, pp. 447–455, 2005.
- [5] R. C. Qiu, "A study of the ultra-wideband wireless propagation channel and optimum UWB receiver design," *IEEE Journal on Selected Areas in Communications*, vol. 20, no. 9, pp. 1628–1637, 2002.
- [6] J. Adeane, W. Q. Malik, I. J. Wassell, and D. J. Edwards, "Simple correlated channel model for ultrawideband multiple-input multiple-output systems," *IET Microwaves, Antennas and Propagation*, vol. 1, no. 6, pp. 1177–1181, 2007.
- [7] D. Dardari, A. Conti, U. Ferner, A. Giorgetti, and M. Z. Win, "Ranging with ultrawide bandwidth signals in multipath environments," *Proceedings of the IEEE*, vol. 97, no. 2, pp. 404–425, 2009.
- [8] S. H. Song and Q. T. Zhang, "Multi-dimensional detector for UWB ranging systems in dense multipath environments," *IEEE Transactions on Wireless Communications*, vol. 7, no. 1, pp. 175–183, 2008.
- [9] P. A. Bello, "Evaluation of mobile ultra wideband modems in dense multipath-part 1: channel model," *IEEE Transactions on Wireless Communications*, vol. 6, no. 11, pp. 4145–4153, 2007.
- [10] T. Santos, F. Tufvesson, and A. Molisch, "Modeling the ultra-wideband outdoor channel: model specification and validation," *IEEE Transactions on Wireless Communications*, vol. 9, no. 6, pp. 1987–1997, 2010.
- [11] J. Choi, N. G. Kang, Y. S. Sung, and S. C. Kim, "Empirical ultra wide band channel model for short range outdoor environments," in *65th Vehicular Technology Conference (VTC '07)*, pp. 1579–1583, April 2007.
- [12] J. Y. Lee, "UWB channel modeling in roadway and indoor parking environments," *IEEE Transactions on Vehicular Technology*, vol. 59, no. 7, pp. 3171–3180, 2010.
- [13] H. Enkoji, N. Hashimoto, H. Aoki, N. Iwakiri, and T. Kobayashi, "Evaluation of a UWB phase-comparison monopulse short-range radar," in *International Conference on Space, Aeronautical and Navigational Electronics (ICSANE '10)*, October 2010.
- [14] H. Krim and M. Viberg, "Two decades of array signal processing research: the parametric approach," *IEEE Signal Processing Magazine*, vol. 13, no. 4, pp. 67–94, 1996.
- [15] B. R. Mahafza, *Radar Systems Analysis and Design Using MATLAB*, Chapman & Hall/CRC, New York, NY, USA, 2005.
- [16] P. Withington, "Impulse radio overview," Time Domain Corp., <http://user.it.uu.se/~carle/Notes/UWB.pdf>.
- [17] X. Luo, L. Yang, and G. B. Giannakis, "Designing optimal pulse-shapers for ultra-wideband radios," *Journal of Communications and Networks*, vol. 5, no. 4, pp. 344–353, 2003.
- [18] R. Xu, Y. Jin, and C. Nguyen, "Power-efficient switching-based CMOS UWB transmitters for UWB communications and radar systems," *IEEE Transactions on Microwave Theory and Techniques*, vol. 54, no. 8, pp. 3271–3277, 2006.
- [19] R. G. Bosisio, Y. Y. Zhao, X. Y. Xu et al., "New wave radio," *IEEE Microwave Magazine*, vol. 9, no. 1, pp. 89–100, 2008.
- [20] M. G. M. Hussain, "Principles of space-time array processing for ultrawide-band impulse radar and radio communications," *IEEE Transactions on Vehicular Technology*, vol. 51, no. 3, pp. 393–403, 2002.
- [21] L. Sakkila, A. Rivenq, C. Tatkeu, Y. El Hillali, J. P. Ghys, and J. Rouvaen, "Methods of target recognition for UWB radar," in *IEEE Intelligent Vehicles Symposium (IV '10)*, pp. 949–954, San Diego, Calif, USA, June 2010.
- [22] S. Gezici and H. V. Poor, "Position estimation via ultra-wide-band signals," *Proceedings of the IEEE*, vol. 97, no. 2, pp. 386–403, 2009.
- [23] R. J. M. Cramer, R. A. Scholtz, and M. Z. Win, "Evaluation of an ultra-wide-band propagation channel," *IEEE Transactions on Antennas and Propagation*, vol. 50, no. 5, pp. 561–570, 2002.

Review Article

Ultrawideband Technology in Medicine: A Survey

R. Chávez-Santiago,^{1,2,3} I. Balasingham,^{1,2,3} and J. Bergsland^{1,2}

¹The Intervention Center, Oslo University Hospital, Sognsvannsveien 20, 0027 Oslo, Norway

²Institute of Clinical Medicine, University of Oslo, 0316 Oslo, Norway

³Department of Electronics and Telecommunications, Norwegian University of Science and Technology (NTNU), 7491 Trondheim, Norway

Correspondence should be addressed to R. Chávez-Santiago, raul.chavez-santiago@rr-research.no

Received 30 November 2011; Accepted 1 February 2012

Academic Editor: Hsien-Chin Chiu

Copyright © 2012 R. Chávez-Santiago et al. This is an open access article distributed under the Creative Commons Attribution License, which permits unrestricted use, distribution, and reproduction in any medium, provided the original work is properly cited.

The utilization of wireless technology in traditional medical services provides patients with enhanced mobility. This has a positive effect on the recovery speed of a person after major surgical procedures or prolonged illness. Ultrawideband (UWB) radio signals have inherent characteristics that make them highly suitable for less invasive medical applications. This paper surveys our own and related recent research on UWB technology for medical sensing and communications. Some research perspectives in the aforementioned topics are suggested too.

1. Introduction

In recent years there has been an increasing interest in using *ultra wideband* (UWB) technology for short-range wireless communication interfaces [1]. The IEEE 802.15.4a standard has adopted UWB as one of the interfaces for robust low-data-rate transmission in wireless personal networks (WPANs) with precision ranging capabilities [2]. UWB signals have an inherent noise-like behavior due to their extremely low maximum effective isotropically radiated power (EIRP) spectral density of -41.3 dBm/MHz. This makes them difficult to detect and robust against jamming, potentially rescinding the need for complex encryption algorithms in tiny transceivers. Owing to these characteristics, UWB has emerged as a solution for the radio communication interface in medical *wireless body area networks* (WBANs) [3]. Additionally, UWB signals do not cause significant interference to other systems operating in the vicinity and do not represent a threat to patients' safety [4]. *Impulse radio* (IR) transceivers have simple structure and very low power consumption, which facilitates their miniaturization [5–7].

Another promising application of UWB as wireless communication interface is in *capsule endoscopy*. A capsule endoscope is a camera with the size and shape of a pill that is swallowed in order to visualize the gastrointestinal tract. They

originally were devised to transmit still images of the digestive tract for subsequent diagnosis and detection of gastrointestinal diseases. Nevertheless, real-time video imaging of the digestive tract is feasible using an UWB radio interface [8, 9]. Although capsule endoscopy is an invasive technique, its use is significantly more comfortable to the patient than traditional endoscopy and colonoscopy. Capsule endoscopes have demonstrated the ability to detect diseases in the small intestine in cases in which other techniques cannot [10–12].

Besides being used as wireless communication interface, UWB technology has many other possible applications in healthcare systems [13]. For instance, the IR-UWB radar has the potential to detect, noninvasively, tiny movements inside the human body [14]. Thereby, it is entirely possible to monitor cardiovascular physiological parameters using movement detection of the aorta [15–18] or other parts of the arterial system. Such parameters include heart rate (HR), respiration motion, blood pressure (BP), and so forth. Due to the architecture of the UWB radar, it is feasible to use the same electronics for both radar sensing and IR-UWB communications [7].

Imaging of surface and more deeply located structures such as breast tissue for cancer diagnosis is another promising application of UWB technology [19–25]. This has the potential of taking over the role of X-ray mammography. The

great advantage of UWB is the absence of harmful effects due to long exposure to ionizing radiation. However, this application is not reviewed in here.

The rest of the paper is organized as follows. Section 2 describes the use of UWB as the communication interface for medical sensors in a WBAN. Section 3 is devoted to the use of UWB for capsule endoscopy. Section 4 surveys the research on UWB radar for medical sensing, particularly BP sensing. Finally, our conclusions are summarized in Section 5.

2. Wireless Body Area Networks

The integration of on-body medical sensors, in-body sensors, and UWB radars into a single network requires a carefully planned architecture in order to guarantee proper operation without mutual interference between the different devices. The Federal Communication Commission (FCC) has allocated the 3.1–10.6 GHz frequency band for UWB communications in the United States [26]. It is important to notice, however, that a large part of this spectrum is strictly regulated in Europe and might not be available for new UWB radio systems. According to the European regulations [27, 28], only the 6–8.5 GHz part of the spectrum is readily available for UWB transmissions without the use of interference mitigation techniques. Transmissions in 3.4–4.2 GHz and 8.5–9 GHz are allowed for devices implementing the detect-and-avoid (DAA) interference mitigation technique. Beyond December 31, 2010, the 4.2–4.8 GHz portion of the spectrum can be used if both DAA and low-duty-cycle (LDC) transmissions are implemented. Below is a description of a viable communication configuration of WBAN using different portions of the UWB spectrum.

2.1. Communication Interface for Implanted Sensors. Our research on UWB radio propagation inside the human body [29] revealed higher signal attenuation at higher frequencies. Since miniaturization and power consumption are the most important design constraints for in-body sensors, the signal attenuation through living tissues must be the minimal possible. Therefore, the 3.4–4.8 GHz frequency band is the most appropriate for these devices [30]. Although the regulations request the implementation of DAA and LDC in this portion of the spectrum, it is very unlikely that radio signals radiated from inside the human body at extremely low power can cause interference to other NB systems. In the case of full-duplex links, DAA and LDC can be implemented in the on-body transceiver where more complex circuitry can be afforded. We have developed UWB propagation models for the communication of implanted sensors. One of these models provides the mathematical expression for the attenuation of a UWB channel between 1 and 6 GHz in the chest [31], as shown below

$$L_{[\text{dB}]}(d) = 10_{[\text{dB}]} + 0.987(d)^{0.85} + \mathcal{N}(0, \sigma), \quad (1)$$

where d is the depth from the skin in millimeters ($1 < d < 120$) and \mathcal{N} is a Gaussian-distributed random variable with zero mean $\mu = 0$ and standard deviation $\sigma = 7.84$ that models the scattering around $L_{[\text{dB}]}(d)$. In the same vein, an

expression for the attenuation in the abdomen is given in [32] as

$$L_{[\text{dB}]}(d) = 3.55_{[\text{dB}]} + 2.46(d) + \mathcal{N}(\mu(d), \sigma(d)), \quad (2)$$

where $1 < d < 150$ mm. The values of $\mu(d)$ and $\sigma(d)$ are found in [32] for different depths.

The mathematical expressions of the statistical characterization for the channel impulse response (CIR) in both cases are provided in [31, 32], respectively. These models facilitate the reproduction of distorted UWB pulses after propagating through human tissues, which is essential for the design and evaluation of implanted transceivers.

2.2. Communication Interface for On-Body Sensors. On-body medical sensors (motes) operate on or in very close proximity to the patient's skin (typically less than 2 centimeters). Typical data rate requirements for common on-body medical sensing devices are given in [3]; electromyography (EMG) sensing is the most throughput-demanding application (up to 1500 kbps). However, it is important to note that continuous EMG monitoring is not necessary as is the case of electrocardiogram (ECG) and electroencephalogram (EEG) that require 10–100 kbps and 10–200 kbps, respectively. The IEEE 802.15.6 task group (<http://www.ieee802.org/15/pub/TG6.html>) has produced the first standard draft that details the characteristics of the UWB wireless interface for on-body sensors. IR-UWB on-body transceivers in the lower part of the UWB spectrum, that is, 3.4–4.8 GHz, are expected to be used. Experimental prototypes of these devices have already been developed [28, 33, 34]. On-body channels are more prone to experience fading and larger RMS delay spread than in-body channels [35]; thus, IR-UWB on-body transceivers are expected to support low data rate only [36].

Because of the complex geometry of the human body, it is likely that some on-body nodes require the relaying of their data when a single-hop link cannot be established because of extremely high signal attenuation. A *relay node* (RN) fulfils this task [28], although it is possible to include relaying capabilities in each mote's transceiver to ensure the establishment of multihop links whenever is required. Moreover, an implanted sensor needs a RN to transmit their data to a network controller for processing and displaying. This special RN is referred to as *gateway node* (GN).

2.3. Network Controller and Patient Monitor. The information collected by the low data rate sensors is gathered by a device known as *body area network controller* (BNC). The on-body sensors are connected to the BNC in a simple star network topology [37] using the IR-UWB 3.4–4.8 GHz on-body interface (Figure 1). The BNC can be devised as a personal digital assistant (PDA) that executes a MAC protocol, for example, [38], in order to ensure that all the sensors transmit their information in an organized and fair way.

For in-home healthcare, the BNC can display several basic vital signals such as temperature, heart rate (HR), blood

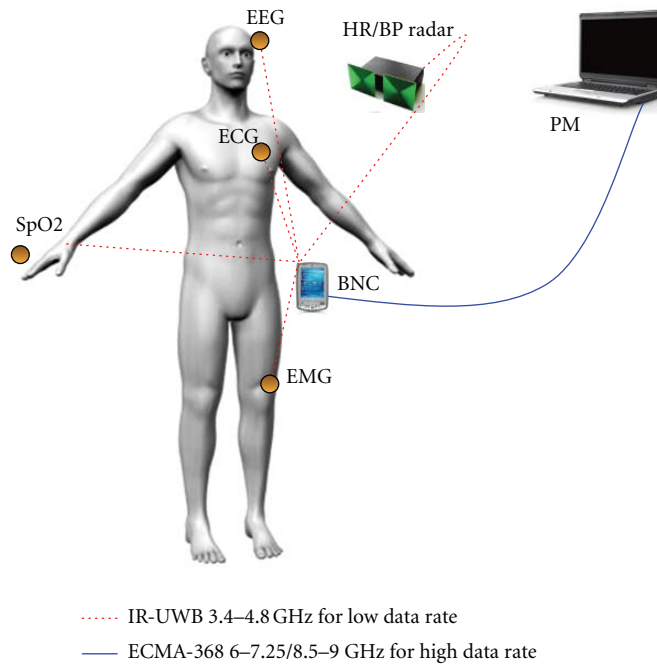


FIGURE 1: Network Topology of an UWB-WBAN.

pressure (BP), and oxygen saturation (SpO_2). However, for in-hospital healthcare and during surgery in an operating room (OR), a more powerful computer is necessary to display more complex signals such as ECG. This computer is referred to as *patient monitor* (PM) and is connected to the BNC through a high-data-rate UWB interface, namely, the ECMA-368 radio interface [39]. This interface, based on multiband orthogonal frequency division multiplexing (MB-OFDM), can support 480 Mbps within distances of up to 3 m and 110 Mbps up to 10 m. The link between the BNC and the PM can operate in the 6–7.25 GHz and 8.5–9 GHz, which roughly translates into subbands 7, 8, and 11, of the 14 subbands in which the UWB spectrum is divided according to the ECMA-368 standard. Other high-data-rate devices such as imaging medical radars can be connected to the PM using the same interface.

As seen, the BNC must support both IR-UWB in 3.4–4.8 GHz and ECMA-368 in 6–7.25 GHz and 8.5–9 GHz. Since DAA is required in 8.5–9 GHz, this part of the spectrum must be occupied mainly for temporary transmissions. The inherent capability for frequency agility of the ECMA-368 interface can be exploited to ensure the electromagnetic compatibility (EMC) of the WBAN with other electronic devices in the OR. The core of an OFDM transceiver is an inverse/direct fast Fourier transform (IFFT/FFT) engine. It has been demonstrated that the FFT engine can be effectively used as a spectrum analyzer with a frequency resolution of 4.125 MHz thereby facilitating the implementation of DAA algorithms [40, 41]. The architecture of a BNC with *cognitive radio* [42] capabilities for the BNC of a medical WBAN has been presented in [43].

3. Capsule Endoscopy

Traditional medical practice for the diagnosis of patients with disorders such as anal bleeding, Crohn's disease, Celiac disease, and intestinal tumors relies on the insertion of flexible tubes containing cameras to examine hard-to-reach parts of the digestive tract. This technique, however, can examine the upper portion of the digestive tract only, while colonoscopes help to visualize the lower part (colon). There is a large portion (approx. 6 m) of the small intestine that cannot be inspected with these techniques. Capsule endoscopes help to fill this gap with significantly less discomfort for the patient.

State-of-the-art capsule endoscopes are swallowed with water, after which the patient puts a recorder belt on the waist. Some hours later (typically eight), medical staff look for abnormalities by reviewing a video created from the still images transmitted wirelessly from the capsule endoscope to the recorder belt. Adding the capability to transmit and analyze high-definition (HD) video in real time can provide further advantages to the medical staff for an accurate diagnosis. This additional capability, however, might increase the complexity of the circuitry and hence the power consumption of the capsule endoscope. The power consumption of a capsule endoscope must be as low as possible (in the order of 1 mW) with a mandatory small physical size (around 300 cubic millimeters). Transmitting real-time video requires a high-transmission-rate communication link, for example, 73.8 Mbps for uncompressed VGA data [37]. All these requirements are difficult to meet using narrowband (NB) systems that operate in the medical implant communication

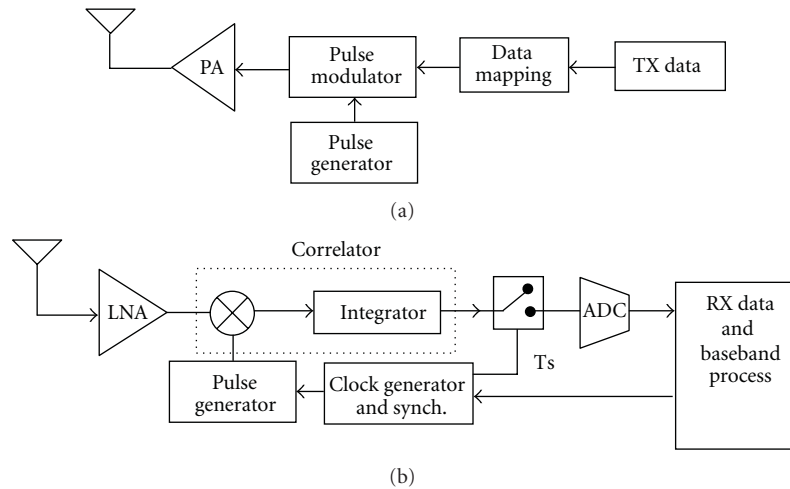


FIGURE 2: (a) In-body transmitter and (b) on-body receiver block diagrams for a capsule endoscope UWB communication system.

systems (MICS) frequency band of 401–406 MHz. In contrast, UWB technology has the potential to fulfill them all. In [9] we proposed the IR-UWB communication system for a capsule endoscope with high-data-rate capabilities. The UWB channel was characterized for the frequency range of 1–5 GHz using computer simulations. Nevertheless, we have recently developed a statistical UWB propagation model for capsule endoscope communications in 1–6 GHz [44].

3.1. In-Body Communication System Architecture. Due to the limitations at the in-body transmitter that include power consumption, size, system cost, and complexity, its communication architecture must be as simple as possible (Figure 2(a)). A pulse generator provides the UWB pulse that is subsequently modulated, amplified, and transmitted. The shape of the transmitted pulse determines the signal bandwidth. We used the fifth derivative of a Gaussian pulse to cover a bandwidth of approximately 1–5 GHz. The power spectral density (PSD) of the transmitted pulse is shown in Figure 3.

The generated data from the electrooptical circuitry of the capsule endoscope is directly modulated without further processing thereby simplifying the transmitter architecture. We considered the biphasic pulse amplitude modulation (BPAM) scheme, in which the data bits are expressed by the polarity of the transmitted pulses. The resulting signal is then amplified and transmitted. The transmitter antenna must cover the entire frequency range with little pulse distortion. The design of a compact UWB antenna for the in-body transmitter is a challenging task, but some designs are available in the literature [45, 46].

3.2. On-Body Communication System Architecture. For the on-body receiver we proposed a novel architecture, which uses a single branch correlator (including a multiplier and an integrator) for recovering the transmitted signal. The block diagram of the receiver is depicted in Figure 2(b).

The UWB antenna at the receiver can be placed on the skin or at some distance away. By placing the receiving

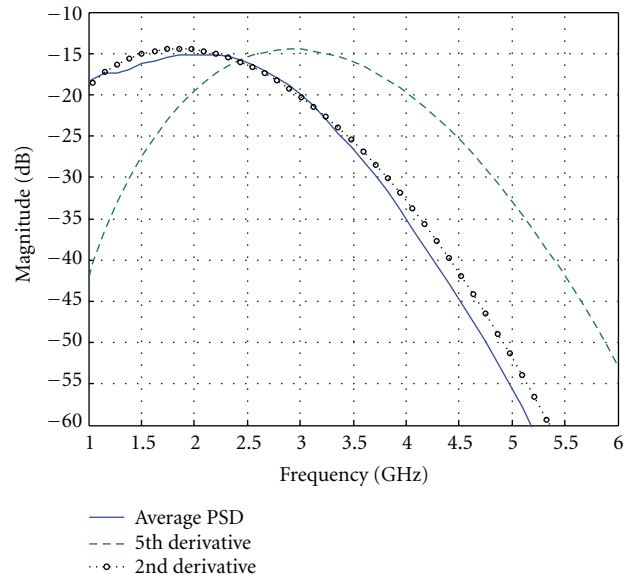


FIGURE 3: PSD of the transmitted Gaussian pulse (fifth derivative), the averaged PSD of the in-body channel, and the second derivative Gaussian pulse signal fitted to the average PSD.

antenna on the body surface, the nonradiative near-field components can be collected by the antenna thus improving the link quality significantly. We have found an improvement of 6 dB due to near-field coupling in UWB in-body links [47]. The practical implementation of the receiver antenna requires a special structure since it must cover a relatively wide body area (abdominal torso) [48]. Commonly, a spatial-diversity antenna array around the torso is embedded in a recorder belt, which is worn by the patient while the capsule endoscope operates.

The low-noise amplifier (LNA) increases the power of the received pulses to a suitable level for signal processing and to overcome noise in subsequent electronic stages. The data are subsequently recovered by the correlator. The correlation operation can be implemented in either analog

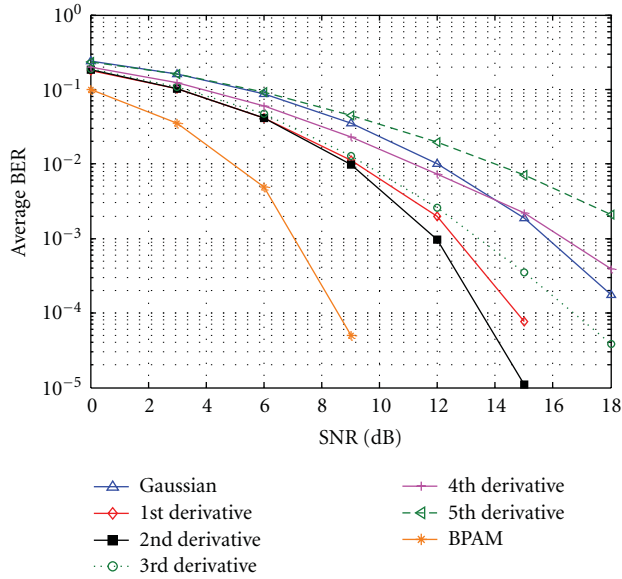


FIGURE 4: Averaged BER performance using different templates.

or digital circuits. Using an all-digital receiver requires highly sophisticated receiver processors with an analog-to-digital converter (ADC) with sampling rate of 2 or 4 times that of the pulse bandwidth and resolution of 4–6 bits. A hybrid analog and digital receiver can reduce the system complexity and cost by decreasing the sampling rate and resolution of the ADC [49]. The correlator output is then sampled, and the ADC converts the analog-demodulated signal into digital form. The digital baseband circuitry provides control for the clock generation, synchronization, and data processing.

One might think that the receiver can take advantage of multipath signals by creating a bank of correlators (rake receiver structure). This idea has been applied to IR-UWB links in dispersive channels with large number of correlators and a more complicate system. However, the imperfect correlations resulting from distorted received pulses reduce the system performance. An optimal way to correct this problem is using a template-match detection technique that performs a matched filter operation with a series of template waveforms. However, the system complexity increases significantly, and channel estimation is required. Hence, we propose using a *single branch correlator* with an optimized predefined template that guarantees maximum energy recovery. The associated delay of the template is adjusted so that maximum correlator output at one branch is generated. The short root-mean-square (RMS) delay spread of in-body channels (in the order of 1 ns) [29] enables this simple architecture.

The design of the pre-defined template depends on the propagation channel characteristics. By multiple electromagnetic (EM) simulations of UWB signals propagating through the abdomen, the normalized average PSD of the “digestive” radio channel was obtained (see Figure 3). The second derivative of a Gaussian pulse can approximate fairly well the PSD of the channel and therefore was chosen as the pre-defined template. It is important to mention, however, that this template pulse choice is optimal for the ideal case that we considered, that is, when the antenna effects are

disregarded. Taking this into account, the antenna effects would have a considerable impact on the optimal template. In such case, the EM simulations must include the particular antenna specifications in order to select the most appropriate template for any other specific design.

3.3. Performance Evaluation. The average bit-error-rate (BER) performance (averaged over 90 arbitrary channel realizations) for different templates in an additive white Gaussian noise environment is compared in Figure 4. The worst performance is observed using the fifth derivative of the Gaussian pulse as template. The reduced BER performance reveals significant distortion of the transmitted pulse while propagating through the body tissues. The best BER performance is obtained for the second derivative, which collects more signal energy from the distorted pulses. For a typical BER of 10^{-3} , a mismatch loss of 5 dB is observed with respect to the ideal case. Using the first and the third derivatives provides almost similar BER performance.

3.4. Ongoing Research. We recently carried out an experiment that demonstrated the feasibility of transmitting high-data-rate video (H.264/1280 × 720 pixels at 30 frames/s) through the living tissues of a porcine surgical model. The in-body to on-body communication was done using an ECMA-368 link in 4.2–4.8 GHz. Proper video transmission at 80 Mbps was achieved at depths from the skin of up to 35 mm. Further improvement is expected using lower frequencies and an implantable antenna [46]. Moreover, if the data from the electrooptical circuitry of the capsule endoscope is properly encoded [50], significant reduction of the required transmission rate can be obtained thereby improving the communication conditions. These speculations will be verified in future experiments.

One of our goals is the development of a full-duplex communication link for capsule endoscopy. This means integrating not only a transmitter but also a receiver (transceiver architecture) in the capsule endoscope. This will allow transmitting external commands (movement, optical focus on specific areas, etc.) to the capsule endoscope thereby adding more control and flexibility to the device. The same transceiver can be used to remotely control microrobotic multifunctional endoscopic devices, capable of performing several diagnostic and therapeutic operations such as biopsy, electrocautery, laser microsurgery, and so forth, with a retractable arm [51].

Accurate tracking of the capsule is required for all the aforementioned applications. However, the tracking problem is rather complicate due to the highly nonhomogeneous structure of the human body. Nevertheless, our research has demonstrated that the use of multimodel (MM) target tracking methods can provide accuracy in-body tracking in the millimeter scale [52, 53].

4. Medical Radar

Heart rate, respiration rate (RR), and heart movements recording have already been proved feasible using IR-UWB

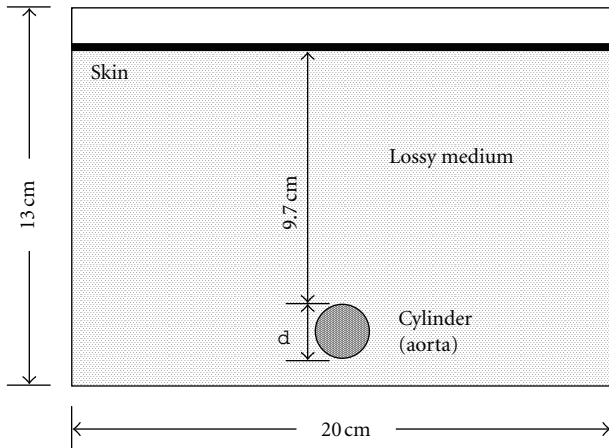


FIGURE 5: 2D simulation model for aorta's diameter estimation.

radar [54, 55]. Several other possible medical applications of UWB radar include ambulatory cardiac output monitoring, blood vessel movement recording, blood pressure celerity measurement, and shock diagnosis in emergency patients. Similar technology can obviously be applied to pneumology and polysomnography for apnoea monitoring in infants, obstructive sleep apnoea monitoring, allergy and asthma crisis monitoring, and so forth. The application of UWB radar in obstetrics as a replacement for ultrasound has also been proposed [14], but this idea has been looked upon cautiously because of the great concern regarding radiofrequency (RF) safety for the newborn. Nevertheless, UWB radar can offer the medical staff and patients several advantages over ultrasound, such as noncontact operation, no need for cleaning after use, remote and continuous operation, lower cost, and easier operation.

4.1. Blood Pressure Measurement. Noninvasive measurements of BP exist such as sphygmomanometer, photoplethysmograph [56], tonography [57], and pulse transit time [58]; however, they all rely on peripheral measurement points. This may constitute a problem in certain situations such as when flow redistribution to central parts of the body (heavy injury, temperature) degrades these measurements; another situation where central measurements may prove advantageous is in the presence of strong movement of the peripheral locations, which affects pressure measurements [59].

The use of radar techniques to measure BP may draw upon ideas from these fields, as well as from ground-penetrating radar (GPR), yet is different enough to merit a specific approach. In particular, the complexity of geometry and stronger attenuation are more significant in BP measurement compared with detection of breast cancer and HR and RR, which are essentially based on shallow reflections.

Estimating BP using radar techniques is necessarily indirect; pressure only affects propagation through the geometry and not material dielectric properties, contrarily to medical imaging using UWB radar for early breast cancer detection. The latter involves transmitting an extremely short pulse through the breast tissues and then recording the backscattered signal from different locations. The basis for

detecting and locating a cancerous tumor is the different dielectric properties of healthy and malignant breast tissue. Healthy tissue is largely transparent to microwaves, whereas tumors, which contain more water and blood, scatter them back to the probing antenna array [22]. However, in the case of the aortic BP, two effects may relate aorta diameter (geometry) to its pressure:

- (i) using the linear relationship between percentage changes in instantaneous BP and diameter, shown for carotid artery pressure in [60];
- (ii) estimating the elasticity of the aorta (local compliance or incremental elastic modulus) and relating this to BP [58, 59, 61] without being explicit with respect to the functional relationship.

In both approaches, the radar-based method aims at detecting the aorta walls and estimates the diameter as a function of time.

From a medical point of view, central measurements are better than peripheral ones. Therefore, we pursued the measurement of BP through movement detection of the aorta. In order to understand the principles of using UWB radar to measure aorta diameter variations, a simple model was constructed for EM simulations [15]. Our model combines a voxel representation of the human body with the material dielectric properties proposed in [62]. It is based on a 2D simplified geometry: a cylinder of diameter d (representing the aorta) immersed in a lossy medium (Figure 5). The lossy medium approximates average living tissue dielectric properties, except for the skin and aorta, the properties of which were taken from [62]. Further details of the model and the EM simulations can be found in [15].

With diameter variations in the order of 2 mm, a set of simulations with aorta diameter ranging from 20 mm to 26 mm in steps of 0.4 mm were conducted in a simulation space with a resolution of 0.1 mm. The current source signal in the simulations was the seventh derivative of a Gaussian pulse with energy centered around 4.5 GHz. This relatively high-order derivative was used for compensating, to a certain extent, the frequency-dependant attenuation in the simulations.

The analysis of the resulting transfer function and the time-domain echoes led to the conclusion that the backscattered signal from the aorta contains necessary information for distinguishing front and rear walls of the aorta thereby making the estimation of its diameter feasible. However, due to strong attenuation in living tissues, feasibility is essentially hinged on a viable power budget. In the simulations, an upper bound on received power in the 0.8–5 GHz range shows a 40 dB loss at the lower end increasing to about 120 dB at the upper end where material loss is dominant.

There are several tradeoffs involved in achieving BP measurements with UWB radar: high-frequency content versus SNR at the receiver as tissues generally severely attenuate the signals; high-frequency versus resolution (and signal-to-clutter reduction) for the same reason. A criterion

for the best selection of bandwidth and center frequency was presented in [16, 17]. Even with a more realistic simulation scenario than that in Figure 5, the feasibility of estimating the aorta radius with the use of UWB radar has been demonstrated [18].

Another key issue that needs to be addressed is whether the use of an antenna array improve measurements, and if so, how much and in which way should this best be implemented. Potentially, the use of an array introduces spatial selectivity and may improve the signal-to-clutter ratio.

Our ongoing research toward the demonstration of BP measurements using UWB radar is focused on measurements with a phantom model that mimics a complex geometry for the estimation of the aorta diameter with sets of static measurements. This will allow for direct comparison between theoretic and practical results.

5. Conclusions

Ultra wideband technology has many potential applications in medicine for less invasive medical diagnosis and monitoring. The UWB radar can potentially be used in novel non-invasive sensing and imaging techniques owing to its high temporal resolution for detecting backscattered signals. We have described our current research on the application of this technology to noninvasive measurement of blood pressure.

The other application of UWB is as low-power wireless communication interface. Particularly, impulse radio seems to perfectly fit the communication requirements of tiny medical sensors, including in-body ones. Our research in this area was presented through the case study of a capsule endoscope system. Additionally, medical sensors and radars can be interconnected using UWB interfaces thereby enhancing the mobility of patients during surgery or intensive therapy. We described the integration architecture of all these systems into a single wireless body area network. One major issue to consider while interconnecting several medical devices using UWB radio interfaces is the possibility of mutual interference with other systems that already operate in the 3.1–10.6 GHz frequency band. Therefore, new interference avoidance techniques and frequency agility such as cognitive radio have to be investigated.

These two aspects of UWB (radar and wireless communication interface) for medical applications are being investigated in Norway by the MELODY Project (<http://www.melody-project.info/>); MELODY stands for “medical sensing, localization, and communications using ultra wideband technology.” The ultimate objective of this project is the improvement of current wireless health systems and the possible development of novel medical applications based on UWB technology.

Acknowledgment

This work is part of the MELODY Project, which is funded by the Research Council of Norway under the Contract no. 187857/S10.

References

- [1] C. C. Chong, F. Watanabe, and H. Inamura, “Potential of UWB technology for the next generation wireless communications,” in *Proceedings of the 9th IEEE International Symposium on Spread Spectrum Techniques and Applications (ISSSTA '06)*, pp. 422–429, Manaus, Amazon, Brazil, August 2006.
- [2] J. Zhang, P. V. Orlik, Z. Sahinoglu, A. F. Molisch, and P. Kinney, “UWB systems for wireless sensor networks,” *Proceedings of the IEEE*, vol. 97, no. 2, pp. 313–331, 2009.
- [3] P. Gandolfo, D. Radović, M. Savić, and D. Simić, “IEEE 802.15.4a UWB-IR radio system for telemedicine,” in *Proceedings of the IEEE International Conference on Ultra-Wideband (ICUWB '08)*, vol. 3, pp. 11–14, Hannover, Germany, September 2008.
- [4] M. Hämäläinen, P. Pirinen, J. Iinatti, and A. Tapparugssana-gorn, “UWB supporting medical ICT applications,” in *Proceedings of The IEEE International Conference on Ultra-Wideband (ICUWB '08)*, vol. 3, pp. 15–16, Hannover, Germany, September 2008.
- [5] A. P. Chandrakasan, F. S. Lee, D. D. Wentzloff et al., “Low-power impulse UWB architectures and circuits,” *Proceedings of the IEEE*, vol. 97, no. 2, pp. 332–352, 2009.
- [6] J. Ryckaert, C. Desset, A. Fort et al., “Ultra-wide-band transmitter for low-power wireless body area networks: design and evaluation,” *IEEE Transactions on Circuits and Systems I*, vol. 52, no. 12, pp. 2515–2525, 2005.
- [7] C. Y. Lee and C. Toumazou, “Ultra-low power UWB for real time biomedical wireless sensing,” in *Proceedings of the IEEE International Symposium on Circuits and Systems (ISCAS '05)*, pp. 57–60, Kobe, Japan, May 2005.
- [8] M. M.-O. Lee, E. -M. Lee, B. L. Cho, K. Eshraghian, and Y. -H. Kim, “The UTCOMS: a wireless video capsule nanoendoscope,” in *Endoscopic Microscopy*, vol. 6082 of *Proceedings of SPIE*, pp. 60820F.1–60820F.10, San Jose, Calif, USA, January 2006.
- [9] A. Khaleghi, R. Chávez-Santiago, and I. Balasingham, “Ultra-wideband pulse-based data communications for medical implants,” *IET Communications*, vol. 4, no. 15, pp. 1889–1897, 2010.
- [10] J. M. Herrerías, A. Caunedo, M. Rodríguez-Téllez, F. Pellicer, and J. M. Herrerías, “Capsule endoscopy in patients with suspected Crohn’s disease and negative endoscopy,” *Endoscopy*, vol. 35, no. 7, pp. 564–568, 2003.
- [11] M. Mylonaki, A. Fritscher-Ravens, and P. Swain, “Wireless capsule endoscopy: a comparison with push enteroscopy in patients with gastroscopy and colonoscopy negative gastrointestinal bleeding,” *Gut*, vol. 52, no. 8, pp. 1122–1126, 2003.
- [12] PHYSorg.com, “Capsule endoscopy turning up undiagnosed cases of Crohn’s disease,” October 2007, <http://www.physorg.com/pdf111757757.pdf>.
- [13] Y. Xu, Y. Lu, H. Zhang, and Y. Wang, “An overview of ultra-wideband and technique application for medial engineering,” in *Proceedings of the IEEE/ICME International Conference on Complex Medical Engineering (CME '07)*, pp. 408–411, Beijing, China, May 2007.
- [14] E. M. Staderini, “UWB radars in medicine,” *IEEE Aerospace and Electronic Systems Magazine*, vol. 17, no. 1, pp. 13–18, 2002.
- [15] L. E. Solberg, I. Balasingham, S. E. Hamran, and E. Fosse, “A feasibility study on aortic pressure estimation using UWB radar,” in *Proceedings of the IEEE International Conference on Ultra-Wideband (ICUWB '09)*, pp. 464–468, Vancouver, Canada, September 2009.

- [16] L.-E. Solberg and I. Balasingham, "Candidate estimators for aorta diameter estimation using bistatic radar," in *Proceedings of the 5th International Conference on Body Area Networks (BodyNets '10)*, Corfu, Greece, September 2010.
- [17] L. E. Solberg, S. E. Hamran, T. Berger, and I. Balasingham, "Minimum variance signal selection for aorta radius estimation using radar," *EURASIP Journal on Advances in Signal Processing*, vol. 2010, Article ID 682037, 13 pages, 2010.
- [18] L.-E. Solberg, S.-E. Hamran, and I. Balasingham, "Realistic simulations of aorta radius estimation," in *Proceedings of the IEEE 4th Int Symposium on Applied Sciences in Biomedical and Communication Technologies (ISABEL '11)*, Barcelona, Spain, October 2011.
- [19] W. Liu, H. M. Jafari, S. Hranilovic, and M. J. Deen, "Time domain analysis of UWB breast cancer detection," in *Proceedings of the 23rd Biennial Symposium on Communications*, pp. 336–339, Kingston, Canada, May–June 2006.
- [20] Y. Chen, E. Gunawan, Y. Kim, K. S. Low, C. B. Soh, and L. L. Thi, "UWB microwave breast cancer detection: generalized models and performance prediction," in *Proceedings of the 28th Annual International Conference of the IEEE Engineering in Medicine and Biology Society (EMBS '06)*, pp. 2630–2633, New York, NY, USA, August–September 2006.
- [21] C. Yifan, E. Gunawan, K. Yongmin, L. Kaysoon, and S. Cheongboon, "UWB microwave imaging for breast cancer detection: tumor/clutter identification using a time of arrival data fusion method," in *Proceedings of the IEEE Antennas and Propagation Society International Symposium (APS '06)*, pp. 255–258, Albuquerque, NM, USA, July 2006.
- [22] W. C. Khor and M. E. Bialkowski, "Investigations into an UWB microwave radar system for breast cancer detection," in *Proceedings of the IEEE Antennas and Propagation Society International Symposium (AP-S '07)*, pp. 2160–2163, Honolulu, Hawaii, USA, June 2007.
- [23] X. Xiao and T. Kikkawa, "Early breast cancer detection by ultrawide band imaging with dispersion consideration," *Japanese Journal of Applied Physics*, vol. 47, no. 4, pp. 3209–3213, 2008.
- [24] X. Xiao and T. Kikkawa, "Influence of the organism interface on the breast cancer detection by UWB," *Applied Surface Science*, vol. 255, no. 2, pp. 597–599, 2008.
- [25] S. A. AlShehri and S. Khatun, "UWB imaging for breast cancer detection using neural network," *Progress in Electromagnetic Research C*, vol. 7, pp. 79–93, 2009.
- [26] FCC, "First report and order, revision of part 15 of the commission's rules regarding ultra-wideband transmission systems," ET Docket 98-153, FCC, 2002.
- [27] E. Faussurier, "Spectrum management and ultra-wideband (UWB)," September 2008, http://www.icuwb2008.org/files/files/pdf/Article-IEUWB_EFA-12sept2008.pdf.
- [28] H.-B. Li, "Body area network—standardization and technology," in *Proceedings of the 2nd International Symposium on Applied Sciences in Biomedical and Communication Technologies (ISABEL '09)*, Bratislava, Slovak Republic, November 2009.
- [29] A. Khaleghi, R. Chávez-Santiago, X. Liang, I. Balasingham, V. C. M. Leung, and T. A. Ramstad, "On ultra wideband channel modeling for in-body communications," in *Proceedings of the IEEE 5th International Symposium on Wireless Pervasive Computing (ISWPC '10)*, pp. 140–145, Modena, Italy, May 2010.
- [30] Q. Wang, K. Masami, and J. Wang, "Channel modeling and BER performance for wearable and implant UWB body area links on chest," in *Proceedings of the IEEE International Conference on Ultra-Wideband (ICUWB '09)*, pp. 316–320, Vancouver, Canada, September 2009.
- [31] A. Khaleghi, R. Chávez-Santiago, and I. Balasingham, "Ultra-wideband statistical propagation channel model for implant sensors in the human chest," *IET Microwaves, Antennas & Propagation*, vol. 5, no. 15, pp. 1805–1812, 2011.
- [32] S. Støa, R. Chavez-Santiago, and I. Balasingham, "An ultra wideband communication channel model for the human abdominal region," in *Proceedings of the IEEE Global Communication Conference (GLOBECOM '10)*, pp. 246–250, Miami, Fla, USA, December 2010.
- [33] O. Lauer, D. Barras, M. Zahner, and J. Fröhlich, "Investigations of an IR-UWB based hardware demonstrator for wireless patient monitoring," in *Proceedings of the Asia-Pacific Symposium & Exhibition on Electromagnetic Compatibility (APEMC '11)*, Jeju Island, South Korea, May 2011.
- [34] J. Shi and J. Wang, "A feasibility study of in-body to on-body transmission with IR-UWB transceiver," in *Proceedings of the Asia-Pacific Symposium & Exhibition on Electromagnetic Compatibility (APEMC '11)*, Jeju Island, South Korea, May 2011.
- [35] IEEE P802.15-08-0780-09-0006, "Channel Model for Body Area Network (BAN)," April 2009.
- [36] I. Dotlić and R. Miura, "Low data-rate ultra-wideband impulse radio communications for wireless medical body area networks," in *Proceedings of the 4th International Symposium on Applied Sciences in Biomedical and Communication Technologies (ISABEL '11)*, Barcelona, Spain, October 2011.
- [37] R. Chávez-Santiago, A. Khaleghi, I. Balasingham, and T. A. Ramstad, "Architecture of an ultra wideband wireless body area network for medical applications," in *Proceedings of the 2nd International Symposium on Applied Sciences in Biomedical and Communication Technologies (ISABEL '09)*, Bratislava, Slovak Republic, November 2009.
- [38] L. Kynsijärvi, L. Goratti, R. Tesi, J. Iinatti, and M. Hämäläinen, "Design and performance of contention based MAC protocols in WBAN for medical ICT using IR-UWB," in *Proceedings of the IEEE International Symposium on Personal, Indoor and Mobile Radio Communications (PIMRC '10)*, pp. 107–111, Istanbul, Turkey, September 2010.
- [39] ECMA-368 Standard, "High Rate Ultra Wideband PHY and MAC Standard," December 2008.
- [40] A. Batra, S. Lingam, and J. Balakrishnan, "Multi-band OFDM: a cognitive radio for UWB," in *Proceedings of the IEEE International Symposium on Circuits and Systems (ISCAS '06)*, pp. 4094–4097, Island of Kos, Greece, May 2006.
- [41] J. Lansford, "The WiMedia UWB radio: is it the ideal cognitive radio processor?" in *Proceedings of the IEEE International Conference on Ultra-Wideband (ICUWB '08)*, vol. 2, pp. 173–176, Hannover, Germany, September 2008.
- [42] N. Devroye, M. Vu, and V. Tarokh, "Cognitive radio networks: highlights of information theoretic limits, models, and design," *IEEE Signal Processing Magazine*, vol. 25, no. 6, pp. 12–23, 2008.
- [43] R. Chávez-Santiago and I. Balasingham, "Cognitive radio for medical wireless body area networks," in *Proceedings of the IEEE 16th International Workshop on Computer Aided Modeling and Design of Communication Links and Networks (CAMAD '11)*, pp. 148–152, Kyoto, Japan, June 2011.
- [44] S. Støa, R. Chavez-Santiago, and I. Balasingham, "An ultra wideband communication channel model for capsule endoscopy," in *Proceedings of the 3rd International Symposium on Applied Sciences in Biomedical and Communication Technologies (ISABEL '10)*, Rome, Italy, November 2010.

- [45] T. Dissanayake, M. R. Yuce, and C. Ho, "Design and evaluation of a compact antenna for implant-to-air UWB communication," *IEEE Antennas and Wireless Propagation Letters*, vol. 8, pp. 153–156, 2009.
- [46] Q. Wang, K. Wolf, and D. Plettemeier, "An UWB capsule endoscope antenna design for biomedical communications," in *Proceedings of the 3rd International Symposium on Applied Sciences in Biomedical and Communication Technologies (ISABEL '10)*, Rome, Italy, November 2010.
- [47] A. Khaleghi and I. Balasingham, "Improving in-body ultra wideband communication using near-field coupling of the implanted antenna," *Microwave and Optical Technology Letters*, vol. 51, no. 3, pp. 585–589, 2009.
- [48] Q. Wang, R. Hahnel, H. Zhang, and D. Plettemeier, "Wearable Vivaldi UWB planar antenna for in-body communication," in *Proceedings of the 4th IEEE International Symposium on Applied Sciences in Biomedical and Communication Technologies (IEEE ISABEL '11)*, Barcelona, Spain, October 2011.
- [49] R. Gharpurey and P. Kinget, *Ultra Wideband: circuits, Transceivers and Systems*, Springer, New York, NY, USA, 2008.
- [50] A. N. Kim, T. A. Ramstad, and I. Balasingham, "Very low complexity low rate image coding for the wireless endoscope," in *Proceedings of the 4th IEEE International Symposium on Applied Sciences in Biomedical and Communication Technologies (IEEE ISABEL '11)*, Barcelona, Spain, October 2011.
- [51] M. O. Schurr, S. Schostek, C. N. Ho, F. Rieber, and A. Menciassi, "Microtechnologies in medicine: an overview," *Minimally Invasive Therapy and Allied Technologies*, vol. 16, no. 2, pp. 76–86, 2007.
- [52] B. Moussakhani, R. Chávez-Santiago, and I. Balasingham, "Multi model tracking for localization in wireless capsule endoscope," in *Proceedings of the 4th IEEE International Symposium on Applied Sciences in Biomedical and Communication Technologies (IEEE ISABEL '11)*, Barcelona, Spain, October 2011.
- [53] B. Moussakhani, J. T. Flâm, S. Støa, I. Balasingham, and T. A. Ramstad, "On localization accuracy inside human abdomen region," *IET Wireless Sensor Systems*, vol. 2, no. 1, pp. 9–15, March 2012.
- [54] C. G. Bilich, "Bio-medical sensing using ultra wideband communications and radar technology: a feasibility study," in *Proceedings of the 1st International Pervasive Health Conference and Workshops, PervasiveHealth*, pp. 1–9, November–December 2006.
- [55] A. Lazaro, D. Girbau, and R. Villarino, "Analysis of vital signs monitoring using an IR-UWB radar," *Progress in Electromagnetics Research*, vol. 100, pp. 265–284, 2010.
- [56] G. Parati, G. Ongaro, G. Bilo et al., "Non-invasive beat-to-beat blood pressure monitoring: new developments," *Blood Pressure Monitoring*, vol. 8, no. 1, pp. 31–36, 2003.
- [57] K. Matthys and P. Verdonck, "Development and modelling of arterial applanation tonometry: a review," *Technology and Health Care*, vol. 10, no. 1, pp. 65–76, 2002.
- [58] J. Y. A. Foo and S. L. Chu, "Pulse transit time as an indirect marker for variations in cardiovascular related reactivity," *Technology and Health Care*, vol. 14, no. 2, pp. 97–108, 2006.
- [59] G. Sharwood-Smith, J. Bruce, and G. Drummond, "Assessment of pulse transit time to indicate cardiovascular changes during obstetric spinal anaesthesia," *British Journal of Anaesthesia*, vol. 96, no. 1, pp. 100–105, 2006.
- [60] M. Sugawara, K. Niki, H. Furuhashi, S. Ohnishi, and S. Suzuki, "Relationship between the pressure and diameter of the carotid artery in humans," *Heart and Vessels*, vol. 15, no. 1, pp. 49–51, 2000.
- [61] J. Lass, K. Meigas, D. Karai, R. Kattai, J. Kaik, and M. Rossmann, "Continuous blood pressure monitoring during exercise using pulse wave transit time measurement," in *Proceedings of the 26th Annual International Conference of the IEEE Engineering in Medicine and Biology (IEMBS '04)*, vol. 1, pp. 2239–2242, San Francisco, Calif, USA, September 2004.
- [62] C. Gabriel and S. Gabriel, "Compilation of the dielectric properties of body tissues at RF and microwave frequencies," Tech. Rep. WC2R 2LS, Department of Physics, King's College, London, UK, June 1996.

Research Article

Ranging Performance of the IEEE 802.15.4a UWB Standard under FCC/CEPT Regulations

Thomas Gigl,¹ Florian Troesch,² Josef Preishuber-Pfluegl,³ and Klaus Witrals¹

¹ Signal Processing and Speech Communication Laboratory, Graz University of Technology 8010 Graz, Austria

² Communication Technology Laboratory, Swiss Federal Institute of Technology (ETH), 8092 Zurich, Switzerland

³ CISC Semiconductor, Design and Consulting GmbH, 9020 Klagenfurt, Austria

Correspondence should be addressed to Thomas Gigl, thomas.gigl@gmail.com

Received 25 October 2011; Accepted 29 January 2012

Academic Editor: Hsien-Chin Chiu

Copyright © 2012 Thomas Gigl et al. This is an open access article distributed under the Creative Commons Attribution License, which permits unrestricted use, distribution, and reproduction in any medium, provided the original work is properly cited.

The IEEE 802.15.4a standard for wireless sensor networks is designed for high-accuracy ranging using ultra-wideband (UWB) signals. It supports coherent and noncoherent (energy detector) receivers, thus the performance-complexity-tradeoff can be decided by the implementer. In this paper, the maximum operating range and the maximum allowed pathloss are analyzed for ranging and both receiver types, under FCC/CEPT regulations. The analysis is based on the receiver working points and a link budget calculation assuming a freespace pathloss model. It takes into consideration the parameters of the preamble, which influence the transmit power allowed by the regulators. The best performance is achieved with the code sequences having the longest pulse spacing. Coherent receivers can achieve a maximum operating range up to several thousand meters and energy detectors up to several hundred meters.

1. Introduction

Real-time locating systems (RTLs) and sensor networks are challenging topics for research and development. Novel applications, such as the tracking of fire fighters in emergencies [1, 2] and the tagging of cars in the manufacturing process, need very precise and reliable localization in multipath intensive environments. Common approaches as, for example, the global positioning system (GPS) or WLAN fail in such situations, because the signals are unable to penetrate the roof and the walls and/or they get disturbed by multipath propagation. Thus, researchers have focused on new radio frequency (RF) technologies in recent years, in particular ultra-wideband (UWB). UWB shows robustness against multipath interference and allows for highly accurate positioning [3–9].

IEEE 802.15.4a [10] is a standard for wireless sensor networks with submeter ranging accuracy in indoor environments. The physical layer is designed for bidirectional communications using amplitude and position modulated, bandpass-type UWB signals. It thus supports high-complexity coherent receivers and low-complexity energy detectors. A two-way time of arrival ranging scheme is

proposed. The first part of each transmission is a pulse sequence with known codes, called the preamble, which is used for signal detection, synchronization, and the estimation of the channel impulse response (CIR) that is needed to obtain the time-of-arrival. The preamble sequences show perfect autocorrelation properties for both receiver types [11]. Energy detectors promise low cost and low power consumption, but a performance loss occurs [12] and more vulnerability is unavoidable with respect to interfering signals [13]. Sub-Nyquist-rate sampling can further reduce the complexity, but also the ranging performance [7, 14].

The IEEE 802.15.4a standard has a large number of system parameters that influence the achievable ranging performance [15–17]. Based on the results in [18], the maximal allowed transmit power is analyzed in this paper taking into account the regulations of the Federal Communication Commission (FCC) [19] and the Conférence Européenne des Postes et Télécommunications (CEPT) [20]. The system performance is evaluated with respect to the achievable operating range and the maximum allowed pathloss for a coherent receiver and an energy detector. Our analysis shows the parameter settings and frequency channel selection for maximizing the performance.

TABLE 1: Preamble characteristic.

N_s	L	N_{pr}	T_{chip} (ns)	T_{pr} (μ s)	PRF (MHz)	MRF (MHz)	ERF (MHz)	N_{1ms}
31	16	16	≈ 2	15.9	31.2	16.1	0.256	16
31	16	64	≈ 2	63.6	31.2	16.1	1.024	64
31	16	256	≈ 2	254.4	31.2	16.1	4.096	256
31	16	1024	≈ 2	1017.4	31.2	16.1	16.1	1006
31	16	4096	≈ 2	4069.7	31.2	16.1	16.1	1006
31	64	16	≈ 2	63.6	7.8	4.03	0.256	16
31	64	64	≈ 2	254.4	7.8	4.03	1.024	64
31	64	256	≈ 2	1017.4	7.8	4.03	4.03	251
31	64	1024	≈ 2	4069.7	7.8	4.03	4.03	251
31	64	4096	≈ 2	16279.0	7.8	4.03	4.03	251
127	4	16	≈ 2	16.3	124.8	62.89	1.024	16
127	4	64	≈ 2	65.1	124.8	62.89	4.096	64
127	4	256	≈ 2	260.5	124.8	62.89	16.384	256
127	4	1024	≈ 2	1042.1	124.8	62.89	62.89	982
127	4	4096	≈ 2	4168.2	124.8	62.89	62.89	982

The paper is organized as follows. Section 2 presents the signal models according to the 802.15.4a standard, a signal-to-noise ratio (SNR) analysis, and the performance metric definition. The FCC and CEPT regulations are discussed in Section 3, and the link budget is introduced in Section 4. This is followed by performance results and conclusions in Sections 5 and 6.

2. Problem Statement

An (indoor) ranging system needs to find the line-of-sight (LOS) component in the channel response, because the detection of a reflection or a noise component may lead to very large errors. Thus, the ranging performance can be characterized by the quality of the channel estimation at the receiver output. An appropriate performance metric is the receiver output SNR of the LOS component (LSNR), as it correlates strongly with the ranging performance [21]. It is defined as

$$\text{LSNR} = \frac{|y_s[n_{\text{LOS}}]|^2}{\text{var}\{\hat{h}[n]\}}, \quad (1)$$

where $y_s[n_{\text{LOS}}]$ is the LOS sample n_{LOS} of the receiver output and $\text{var}\{\hat{h}[n]\}$ is the noise variance of the estimated channel response $\hat{h}[n]$.

To study the operating range, it is necessary to relate the output SNR to the input SNR of the receiver. The input SNR is given by the transmit power regulations, the link budget, and the channel. The output SNR furthermore depends on the receiver structure, the hardware components, and—in case of a noncoherent receiver—also on the preamble parameters, as analyzed below. The input SNR is defined by the energy of the despread LOS component over the noise spectral density E_{LOS}/N_0 with $E_{\text{LOS}} = M_1 E_{\text{LOS}}^{(1)}$, where $E_{\text{LOS}}^{(1)}$ is the received energy for the LOS component of a single pulse and M_1 is the number of transmitted pulses.

2.1. Signal Models. This section introduces the signal models for the IEEE 802.15.4a physical layer and the receivers.

2.1.1. IEEE 802.15.4a. The most important signal part for ranging is the preamble. It employs a code sequence \mathbf{c}_s of length $N_s = 31$ or 127 [10] that consists of ternary elements $\{-1, 0, 1\}$. The preamble code vector \mathbf{c}_{sp} is created as

$$\mathbf{c}_{sp} = \mathbf{1}_{N_{pr}} \otimes \mathbf{c}_s \otimes \boldsymbol{\delta}_L = \mathbf{c} \otimes \boldsymbol{\delta}_L, \quad (2)$$

where \otimes denotes the Kronecker product, $\boldsymbol{\delta}_L$ is a unit vector with a one at the first position and length L to extend the spacing between the preamble chips, and $\mathbf{1}_{N_{pr}}$ denotes a vector of ones to repeat the preamble sequence N_{pr} times. The vector \mathbf{c} is the periodically repeated preamble code. The transmitted signal $s(t)$ is defined as

$$\begin{aligned} s(t) &= \Re \left\{ \sqrt{E_p} \sum_{m=0}^{M-1} c_m w(t - mL T_{\text{chip}}) e^{j\omega_c t} \right\} \\ &= \sqrt{E_p} \sum_{m=0}^{M-1} c_m \tilde{w}(t - mL T_{\text{chip}}), \end{aligned} \quad (3)$$

where E_p is the energy per pulse, c_m is the m -th element of \mathbf{c} , $w(t)$ is the energy-normalized pulse shape, M is the number of code elements in the preamble, ω_c is the carrier frequency, T_{chip} is the chip duration, and $\tilde{w}(t)$ is the upconverted pulse assuming the carrier and the pulse are phase synchronous.

Table 1 shows the timing characteristics of the preamble, where T_{pr} is the total duration of the preamble, PRF is the peak pulse repetition frequency, MRF is the mean pulse repetition frequency, and N_{1ms} is the number of preamble sequences within 1 ms. ERF is the effective pulse repetition frequency according to the regulations (see Section 3).

The transmitted signal (3) is sent over a multipath channel with channel impulse response $h_c(t)$, where also the effects of the antenna are contained for simplicity.

Furthermore, $h_c(t)$ is assumed to be constant during T_{pr} . Thus, the analog received signal is obtained from

$$r_a(t) = s(t) * h_c(t) + \nu(t), \quad (4)$$

where $\nu(t)$ is modeled as additive white Gaussian noise and $*$ is the convolution. Next, the receiver architectures are described.

2.1.2. Coherent Receiver. Figure 1 shows the system model of the coherent receiver. The signal is received by a UWB antenna and filtered by the transmit pulse shape $\tilde{w}(t)$. Thus, a matched filtering to the pulse shape is applied. The signal is converted to complex baseband using the Hilbert transform $h_{\text{hilb}}(t)$ and carrier demodulation by the estimated frequency $\hat{\omega}_c$. The complex baseband signal is given by

$$r_b(t) = [r_a(t) * \tilde{w}(t) * h_{\text{hilb}}(t)]e^{-j\hat{\omega}_c t + \varphi}, \quad (5)$$

where φ is the unknown carrier phase. Assuming synchronization and known carrier frequency, an estimated sampled channel response is obtained after despreading,

$$\hat{h}[n] = M_1 h[n] + \sum_{q=0}^{N_{pr}-1} \sum_{m=0}^{N_s-1} c_m \nu_b[n + (m + qN_s)LN_{\text{chip}}], \quad (6)$$

because the preamble codes have perfect circular autocorrelation properties, thus interpulse interference (IPI) is canceled. (For this assumption it is necessary that the maximal excess delay $\tau_{\text{max}} \leq LN_s T_{\text{chip}} = T_s$, where T_s is the period of the spread preamble sequence. The IEEE 802.15.4a standard has a $T_s \geq 1 \mu\text{s}$, which is usually sufficient for IPI free processing in indoor environments.) The despreading is first performed sequencewise (\sum_m) and then over the sequence repetitions (\sum_q). Since $c_m^2 = 1$ for the nonzero code elements, it follows that \sum_q and \sum_m simply the number of nonzero code elements in the preamble $M_1 = ((N_s+1)/2)N_{pr}$, that is, the number of transmitted pulses. The number of samples within a chip is defined by $N_{\text{chip}} = T_{\text{chip}}/T$. The noise $\nu_b[n]$ is the band-limited input noise $\nu_b[n] = \nu[n] * w[n]$ in complex baseband. A detailed derivation of the equations can be found in [15].

This receiver architecture needs high sampling rates according to the Nyquist theorem. Another disadvantage of this concept is the required synchronization of the carrier frequency and phase, which is critical for its performance. The energy detector is based on a different method for the downconversion that prevents these two problems. Thus, a low-complexity solution is obtained.

2.1.3. Energy Detector. The energy detector works as shown in Figure 2. The signal is again received by a UWB antenna and filtered by a bandpass filter, which ideally is matched to the pulse shape. Next, the signal is squared and integrated for short-time windows T_I . The length of T_I also defines the sampling period. It causes a mean absolute error (MAE) of ranging greater or equal $T_I/4$ [7], which limits T_I to a few ns

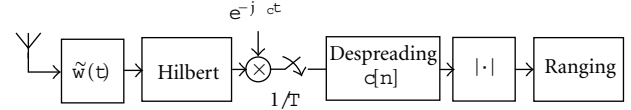


FIGURE 1: Coherent receiver.

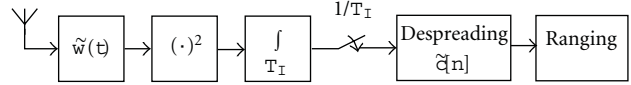


FIGURE 2: Energy detector.

for highly accurate ranging. The signal model after sampling is given by

$$\begin{aligned} x[n] &= \int_{nT_I}^{(n+1)T_I} (r_a(t) * \tilde{w}(t))^2 dt \\ &= \int_{nT_I}^{(n+1)T_I} \left(\sum_{m=0}^{M-1} c_m g(t - mL T_{\text{chip}}) + \nu_f(t) \right)^2 dt, \end{aligned} \quad (7)$$

where $\nu_f(t)$ is the passband filtered noise and the channel response $g(t) = \sqrt{E_p} \phi_{\tilde{w}}(t) * h_c(t + mL T_{\text{chip}})$ and $\phi_{\tilde{w}}(t)$ is the autocorrelation function of $\tilde{w}(t)$. The estimated channel response $y[n]$ is obtained by despreading $x[n]$,

$$\begin{aligned} y[n] &= \sum_{q=0}^{N_{pr}-1} \sum_{i=0}^{N_s-1} \tilde{c}_i x[n + iL\tilde{N}_{\text{chip}} + qN_sL\tilde{N}_{\text{chip}}] \\ &= y_{ss}[n] + y_{sv}[n] + y_{vv}[n], \end{aligned} \quad (8)$$

where $\tilde{N}_{\text{chip}} = T_{\text{chip}}/T_I$. The code despreading is performed sequencewise with \sum_q and \sum_i with the despreading code \tilde{c}_i . In contrast to the coherent receiver, the noncoherent receiver uses a different despreading code \tilde{c} than the spreading code to obtain perfect circular correlation properties for the squared sequences. This code is created by squaring c and setting all zeros to -1 [11]. The output of the energy detector comprises a signal-by-signal term $y_{ss}[n]$, a linear signal-by-noise term $y_{sv}[n]$, and a quadratic noise-by-noise term $y_{vv}[n]$. The code correlation can completely cancel the IPI in the signal term $y_{ss}[n]$ but not for the cross-term $y_{sv}[n]$. A longer pulse spacing leads to less IPI such that it becomes negligible in indoor environments with a spacing of $L \geq 16$ [15, 16]. The full derivation of the equations can also be found in these references.

2.2. Input-to-Output SNR Relation. The input-to-output SNR relation for the coherent receiver is given by [15]

$$\text{LSNR}_{\text{CR}} = \frac{E_{\text{LOS}}}{N_0}. \quad (9)$$

For the energy detector, the relation is given by [15, 16]

$$\text{LSNR}_{\text{ED}} = \frac{2(E_{\text{LOS}}/N_0)^2}{4(E_{\text{LOS}}/N_0) + N_s N_{pr} T_I W_{\text{RRC}}}, \quad (10)$$

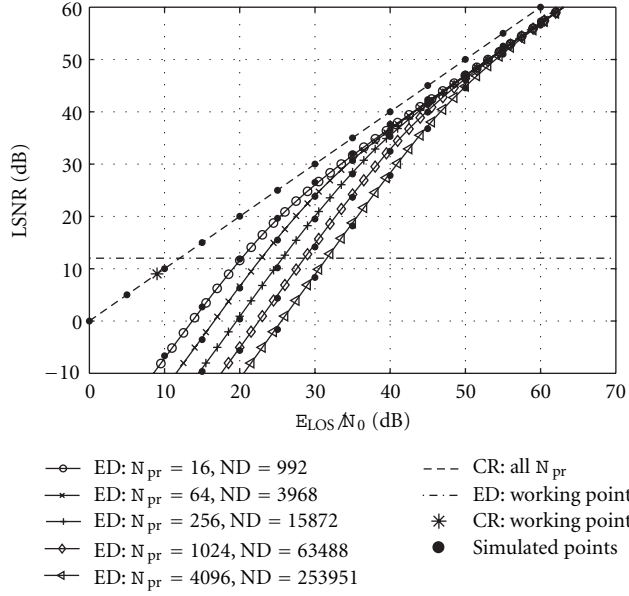


FIGURE 3: Relation between input SNR (E_{LOS}/N_0) and output SNR (LSNR) with respect to the noise dimensionality $\text{ND} = N_s N_{\text{pr}} T_I W_{\text{RRC}}$ for the energy detector (ED) and the coherent receiver (CR). The fixed parameters are $N_s = 31$, $T_I = 2.0032$ ns, and $W_{\text{RRC}} = 1$ GHz.

where W_{RRC} is an equivalent bandwidth defined as $W_{\text{RRC}} = \int \phi_w^2(\mu) d\mu$. The first and second terms of the denominator correspond to the variance of the linear and the quadratic noise terms, respectively. The quadratic noise term depends on the receiver parameters that can be combined to the noise dimensionality $\text{ND} = N_s N_{\text{pr}} T_I W_{\text{RRC}}$ [13]. For practical values of ND, the output SNR is proportional to $(E_{\text{LOS}}/N_0)^2$, while it shows a linear relation to E_{LOS}/N_0 for the coherent receiver.

Figure 3 shows the relation of the detector input SNR E_{LOS}/N_0 and the output LSNR based on (9) and (10). The specific curves for the energy detector (ED) are obtained by increasing ND by factors of four. The depicted curves correspond to $N_{\text{pr}} = [16, 64, 256, 1024, 4096]$, $N_s = 31$, $T_I = 2$ ns, and $W_{\text{RRC}} = 1$ GHz. Note that $N_{\text{pr}} = 256$ is not included in the standard. The curves are separated if the quadratic noise term dominates and they merge if the linear noise term is dominant. Increasing E_{LOS}/N_0 by 6 dB leads to LSNR +12 dB in the quadratic part and to +6 dB in the linear one. The horizontal line illustrates the LSNR at the working point $\text{LSNR}_{\text{WP}} = 12$ dB for the energy detector (cf. [16]). At this working point, 80% of the range estimates are within 1 m. The coherent receiver shows a working point $\text{LSNR}_{\text{WP}} = 9$ dB (cf. [21]). Both working points have been determined by extensive simulations (see [15]). It can be seen for the energy detector that 3 dB more E_{LOS}/N_0 are required when N_{pr} , the number of sequence repetitions, is increased by a factor of four. Note that the quadratic noise term dominates at this working point. As observable from (9), the LSNR for the coherent receiver is independent of the number of the pulses. It depends only on the transmitted energy. In other words, it does not matter if this energy is transmitted in one

TABLE 2: Link budget.

Parameter		Values
Pulse energy (incl. G_{TX})	E_p	-116.38 dBWs
Preamble energy	E_{pr}	-74.31 dBWs
Free space loss at 1 meter	L_{fs}	-45.5 dB
Receiver antenna gain	G_{RX}	0 dBi
Received LOS component energy	\tilde{E}_{LOS}	-119.81 dBWs
Noise spectral density	N_0	-198.93 dBW/Hz
Implementation loss	L_{imp}	4 dB
Fading margin	M_F	3 dB
Receiver input SNR	$E_{\text{LOS}}/N_0(1 \text{ m})$	72.12 dB

pulse or in a sequence of pulses. The coherent receiver shows an advantage ≥ 11 dB in the working point in comparison to the noncoherent receiver.

2.3. *Maximal Operating Distance.* As N_0 is constant in the scenario, E_{LOS}/N_0 for the maximal operating distance d_{max} is obtained from the well-known pathloss model

$$\frac{E_{\text{LOS}}}{N_0}(d_{\text{max}})_{\text{dB}} = \frac{E_{\text{LOS}}}{N_0}(d_0)_{\text{dB}} - 10\eta \log\left(\frac{d_{\text{max}}}{d_0}\right), \quad (11)$$

where η is the pathloss exponent and d_0 is a reference distance. The maximal operating distance for the coherent receiver is obtained from (9) and (11):

$$d_{\text{max}} = \left(\frac{(E_{\text{LOS}}/N_0)(1 \text{ m})}{(E_{\text{LOS}}/N_0)(d_{\text{max}})}\right)^{1/\eta} = \left(\frac{(E_{\text{LOS}}/N_0)(1 \text{ m})}{\text{LSNR}_{\text{WP}}}\right)^{1/\eta}, \quad (12)$$

where the reference distance d_0 is assumed to be 1 m. It follows for the energy detector

$$d_{\text{max}} = \left(\frac{(E_{\text{LOS}}/N_0)(1 \text{ m})}{\text{LSNR}_{\text{WP}} + \sqrt{\text{LSNR}_{\text{WP}}(\text{LSNR}_{\text{WP}} + \text{ND}/2)}}\right)^{1/\eta} \quad (13)$$

using (10) in (11).

2.4. *Maximal Allowed Pathloss PL_{max} .* A more general look at the achievable range is given by the maximal allowed pathloss, which is independent of the channel model, fading margins, or implementation losses. The pathloss model can be rewritten with (9) to obtain PL_{max} for the coherent receiver

$$PL_{\text{max,dB}} = \frac{\tilde{E}_{\text{LOS}}}{N_0}(1 \text{ m})_{\text{dB}} - \text{LSNR}_{\text{WP,dB}}, \quad (14)$$

where \tilde{E}_{LOS} is the energy of the received LOS component at 1 m, which does not take fading margins or implementation losses into account (see Table 2).

For the energy detector follows, using (10) and (11),

$$\begin{aligned} PL_{\max, \text{dB}} &= \frac{\tilde{E}_{\text{LOS}}}{N_0} (1 \text{ m})_{\text{dB}} \\ &\quad - 10 \log \left(\text{LSNR}_{\text{WP}} + \sqrt{\text{LSNR}_{\text{WP}} \left(\text{LSNR}_{\text{WP}} + \frac{\text{ND}}{2} \right)} \right). \end{aligned} \quad (15)$$

$E_{\text{LOS}}/N_0(1 \text{ m})$ and $\tilde{E}_{\text{LOS}}/N_0(1 \text{ m})$ are defined by the transmitted preamble energy E_{pr} (see Section 3) and the link budget (see Section 4).

3. FCC Regulations

In this section, the maximal allowed transmit power is calculated with respect to the FCC regulations [19]. In principle, the same regulations have been adopted by the CEPT in Europe for the band between 6 and 8.5 GHz [20]. In the band between 3.1 and 4.8 GHz, the CEPT requires detect and avoid (DAA) or low duty cycle (LDC) mitigation additionally, which does not influence this analysis. This analysis is done in accordance to [18].

The FCC constraints essentially consist of an average and a peak power limit. In any band of bandwidth $B_{\text{av}} = 1 \text{ MHz}$, the average transmit power is limited to $P_{\text{av}}^{\text{FCC}} = -41.3 \text{ dBm}$ for an averaging window of $T_{\text{av}} = 1 \text{ ms}$. The peak power within the bandwidth $B_{\text{pk}} = 50 \text{ MHz}$ is restricted to $P_{\text{pk}}^{\text{FCC}} = 0 \text{ dBm}$. Both peak and average transmit power are defined by the equivalent isotropically radiated power (EIRP).

The 802.15.4a preamble is a sequence of nonuniformly spaced pulses whose polarities are chosen pseudorandomly by the codes. According to [18], its average and peak power are determined by ERF and PRF, respectively. The pulse energy spectral density (ESD) $E_{p,\text{av}}|W(f_c)|^2$ for the average power limit is given by

$$E_{p,\text{av}}|W(f_c)|^2 = \begin{cases} \frac{T_{\text{av}} P_{\text{av}}^{\text{FCC}}}{2B_{\text{av}}}, & \text{ERF} \leq \frac{1}{T_{\text{av}}}, \\ \frac{P_{\text{av}}^{\text{FCC}}}{2B_{\text{av}} \text{ERF}}, & \text{ERF} \geq \frac{1}{T_{\text{av}}}, \end{cases} \quad (16)$$

where $E_{p,\text{av}}$ is the pulse energy limited by the average power limit and $W(f_c)$ is the spectrum of the normalized pulse $w(t)$ at the center frequency f_c . ERF is defined as

$$\text{ERF} = \begin{cases} \text{MRF} \frac{T_{\text{pr}}}{T_{\text{av}}} = \frac{M_1}{T_{\text{av}}} & T_{\text{pr}} < T_{\text{av}} \\ \text{MRF} & T_{\text{pr}} \geq T_{\text{av}} \end{cases} \quad (17)$$

where $M_1 = (N_s + 1)/2$ is the number of code elements not equal to zero. ERF is the compressed MRF due to stretching the preamble over the averaging time $T_{\text{av}} = 1 \text{ ms}$ (FCC). If T_{pr} is greater than T_{av} , then it is MRF. The mean power is limited by the number of pulses within 1 ms ($N_{1 \text{ ms}}$) (see Table 1).

The peak power limit is defined by the PRF, where the sequenced pulses within an observation window

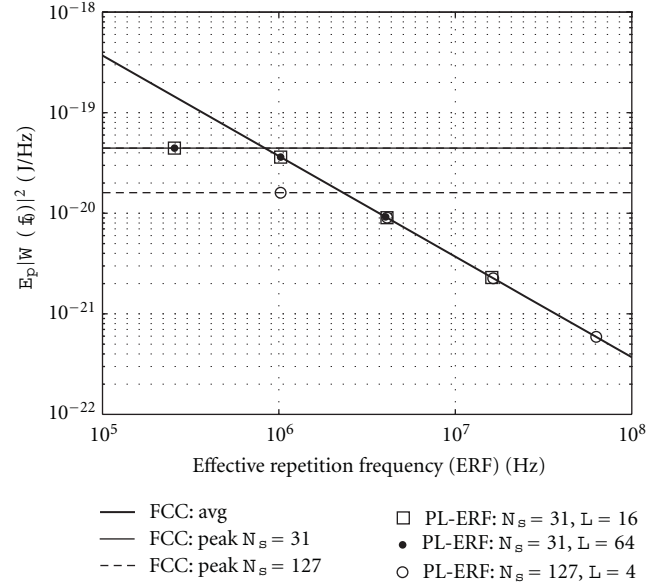


FIGURE 4: Pulse energy spectral density.

$1/B_{\text{pk}} = 20 \text{ ns}$ are added. The ESD $E_{p,p}|W(f_c)|^2$ for the peak power limit is obtained by

$$E_{p,p}|W(f_c)|^2 = \begin{cases} \frac{P_{\text{pk}}^{\text{FCC}}}{9B_{\text{pk}}^2}, & \text{PRF} \leq \left(\frac{3}{2}\right)B_{\text{pk}}, \\ \frac{P_{\text{pk}}^{\text{FCC}}}{4\text{PRF}^2}, & \text{PRF} \geq \left(\frac{3}{2}\right)B_{\text{pk}}, \end{cases} \quad (18)$$

where $E_{p,p}$ is the pulse energy limited by the peak power limit.

The maximal FCC compliant pulse ESD with respect to peak and average power is shown in Figure 4. To find the active ESD for a specific preamble, the smaller value between ESD_{pk} at PRF and ESD_{av} at ERF is considered. The peak power limit for the short preamble symbols with $L = 16$ and $L = 64$ is the same, while, for the long preamble sequences it is lower due to higher PRF. It can be observed that only the preamble sequences with $N_{\text{pr}} = 16$ are peak power limited. However, it is reported in [22] that the supply voltage limits the transmit power in low-data-rate systems and the peak power limit cannot be exploited for low supply voltages.

Assuming a pulse with rectangular spectrum, the energy per pulse $E_p = 2BE_p|W(f_c)|^2$, where B is the pulse bandwidth. Thus, the achievable preamble SNR can be calculated as shown in Figure 5. At $N_{\text{pr}} = 16$, all preamble codes are limited by the peak power limit. The long preamble symbols contain approximately 2 dB more energy in four times more pulses. Increasing the number of pulses does not necessarily lead to a preamble energy improvement, if $T_{\text{pr}} \leq 1 \text{ ms}$, because the long preamble symbols and the short codes with spreading $L = 16$ are mean power limited between $N_{\text{pr}} = 64$ and 1024. $N_{\text{pr}} = 4096$ leads to an improvement, because $T_{\text{pr}} > 4 \text{ ms}$, which means the preamble is more than four times longer than T_{av} . The short preamble codes with spreading 64 imply a four times longer preamble in contrast to the others, thus a gain of up to 6 dB can be achieved.

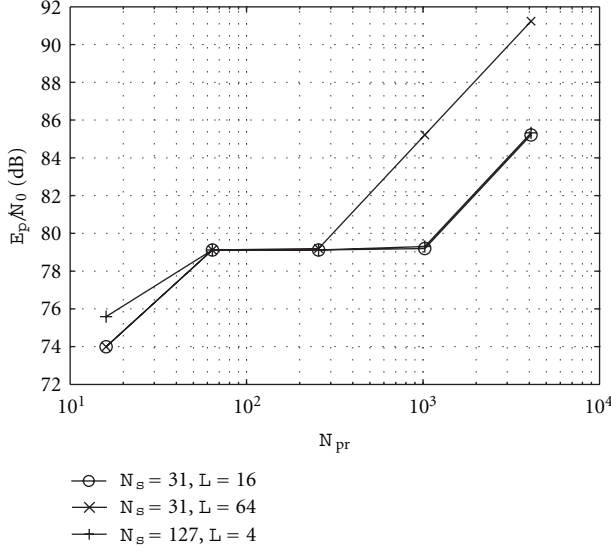


FIGURE 5: Achievable preamble energies.

4. Link Budget

As mentioned before, $E_{LOS}/N_0(1m)$ is the input SNR of the receiver at 1 m which depends on the link budget. Table 2 shows an example link budget calculation for 802.15.4a channel (ch) 3, using $N_{pr} = 1024$, $N_s = 31$, $L = 16$, $f_c = 4.4928$ GHz, and a bandwidth of 499.2 MHz. In that case, the average power limit of the FCC regulations applies and E_p is calculated from (16), where also the antenna gain is included. E_p is limited for 1006 sequences due to averaging over 1 ms (see Table 1). The preamble energy $E_{pr} = E_p M_1$, the free space loss L_{fs} at 1 m is given by 45.5 dB using Friis' equation [23], and the receiver antenna gain G_{RX} is defined by 0 dBi. These values yield the received preamble energy without multipath components, meaning the energy of the line of sight component \tilde{E}_{LOS} at 1 m. Assuming the input structure of the receiver is linear, the noise spectral density is given by $N_0 = kT_0F$ [23], where the Boltzmann constant $k = 1.38 \times 10^{-23}$ Joule/Kelvin [J/K], the temperature of the environment $T_0 = 293$ K, and the noise figure of the receiver input structure $F = 5$ dB (cf. [24]). Implementation losses of 4 dB and a LOS fading margin of 3 dB are assumed. Thus, $E_{LOS}/N_0(1m)$ is obtained and can be used to calculate the maximal operating range according to (11) and (13).

5. Results

The maximal operating distance and the maximal acceptable pathloss are analyzed in this section. The maximal operating distance is based on the free-space link budget, because the LOS component is needed for accurate ranging. The maximal acceptable pathloss is shown as a more general value, which allows the implementer to analyze the effect of specific channel models, for example, NLOS scenarios, or specific system parameters, for example, lower noise figures.

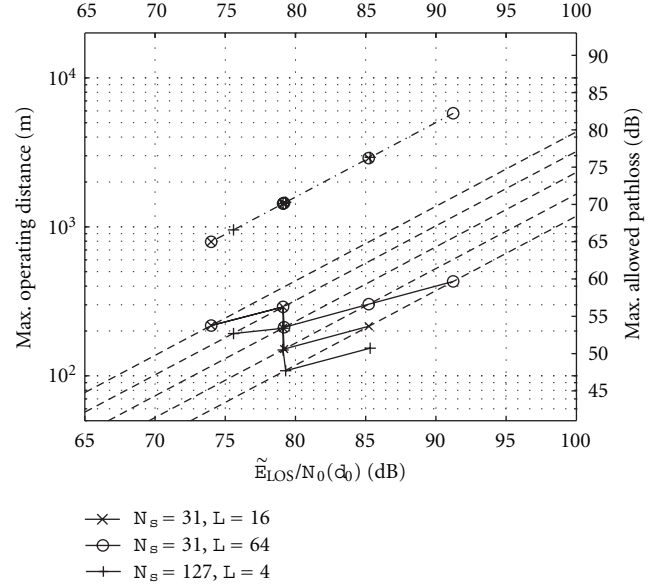


FIGURE 6: Code sequence analysis on the maximal operating distance and the maximal allowed pathloss, where the solid lines correspond to the energy detector, the dashed-dotted lines belong to the coherent receiver, and the dashed lines indicate constant noise dimensionality for the energy detector. The values are given for $N_{pr} = [16, 64, 256, 1024, 4096]$ (from left to right).

5.1. Effect of Codes. Figure 6 shows the maximal operating distance d_{max} and the maximal allowed pathloss PL_{max} with respect to the length N_{pr} of the preamble sequences. The coherent receiver is directly proportional to E_p/N_0 , which means that the operating distance is related to the preamble energy discussed in Figure 5. By contrast, the ED suffers from noncoherent combining losses, thus the noise dimensionality including the number of transmitted pulses is important for the final performance (see (13)). A change of E_p/N_0 without changing the noise dimensionality, for example, using a different noise figure or pulse energy, leads to a shift of the curves along the dashed lines, but the shape of the curves does not change. Thus, the general conclusions are still valid, while d_{max} and PL_{max} need to be recalculated according to the new link budget.

In the overall performance there is a big gap between the CR and the ED. The CR achieves a maximal operating distance up to several thousand meters and the ED achieves only several hundred meters. However, an operating distance of several hundred meters is usually sufficient for (low-complexity) indoor localization systems and sensor networks.

As expected from Section 3, the best performance is achieved by the short preamble with long spreading ($L = 64$) which has the highest transmitted energy. A maximal operating distance of approximately 6000 m ($PL_{max} \approx 82$ dB) is achieved by the CR, and ≈ 430 m ($PL_{max} \approx 60$ dB) is achieved by the ED. The CR reaches approximately half of that distance (≈ 3000 m; $PL_{max} \approx 76$ dB) for the other two codes. As mentioned before, the energy detector shows a more specific behavior, which is discussed in detail in the rest

of this paragraph. As observable, the increasing of N_{pr} does not necessarily lead to a better performance. A performance degradation is seen at around $\tilde{E}_{LOS}/N_0(d_0) \approx 79$ dB for increasing numbers of transmitted pulses due to constant transmitted energy (cf. Figure 5). This effect also harms the performance of the long preamble codes ($N_s = 127$) significantly and leads to the lowest performance achieved. The performance of the short preamble sequences ($N_s = 31$) with spreading $L = 16$ and the long preamble sequences ($N_s = 127$) is best at $N_{pr} = 64$, where a distance of ≈ 300 m ($PL_{max} \approx 56$ dB) and ≈ 200 m ($PL_{max} \approx 53$ dB) is reached, respectively. The preamble sequences with $L = 64$ show a local optimum for $N_{pr} = 64$ with the same performance as the $L = 16$ sequence. This performance is also obtained for a much longer preamble with $N_{pr} = 1024$ repetitions and slightly improved with $N_{pr} = 4096$ at the cost of increased preamble energy (cf. Figure 5), much longer signals (see Table 1), and much higher processing effort. From these results, it seems inefficient for EDs to choose extremely long preambles with $N_{pr} \geq 1024$.

The IEEE 802.15.4a standard also defines different channels with specific bandwidths and carrier frequencies. An analysis of the various channels is given in the next section.

5.2. Effect of Frequency Channels. The IEEE 802.15.4a standard defines 16 channels in three frequency bands, the subgigahertz band (<1 GHz), the low band (3.2–4.8 GHz), and the high band (5.9–10.3 GHz). The channel bandwidths B range from 499.2 to 1354.97 MHz. As mentioned in Section 3, keep in mind that the CEPT allows only the usage of the frequency bands 3.1–4.8 and 6–8.5 GHz for UWB, where, for LDC, the signals have to be shorter than 5 ms. Thus, the short preamble symbol with spreading $L = 64$ and $N_{pr} = 4096$ is not allowed for LDC transmission. It is well known that a higher carrier frequency f_c causes higher losses and thus less received signal strength according to Friis' equation. A larger bandwidth leads to a higher allowed transmit power (see Section 3). To evaluate this tradeoff, six channels are analyzed in this paper, using the short preamble codes with $L = 64$.

Figure 7 shows the relation between input and output SNR for the specific channels. As seen from (9), the CR is again independent of the channel bandwidths. For the ED, variations occur due to the different pulse and receiver bandwidths. It can be observed that the channels with the large bandwidths need up to 1.5 dB more E_p/N_0 in the working point to achieve the same LSNR.

Figure 8 shows the allowed preamble energies for the specific channels. The larger bandwidths of the preambles allow a gain of up to 4 dB, which is sufficient to compensate the SNR loss of the ED shown in Figure 7. This is also seen from (10), where the equivalent bandwidth W_{RRC} influences LSNR linearly and the additional energy improves the SNR quadratically in the working point. Thus, a gain of up to 2.5 dB can be achieved. For the CR, the additional energy will directly improve the performance.

Figure 9 shows the maximal operating distance and the maximal allowed pathloss for the specific channels. It can

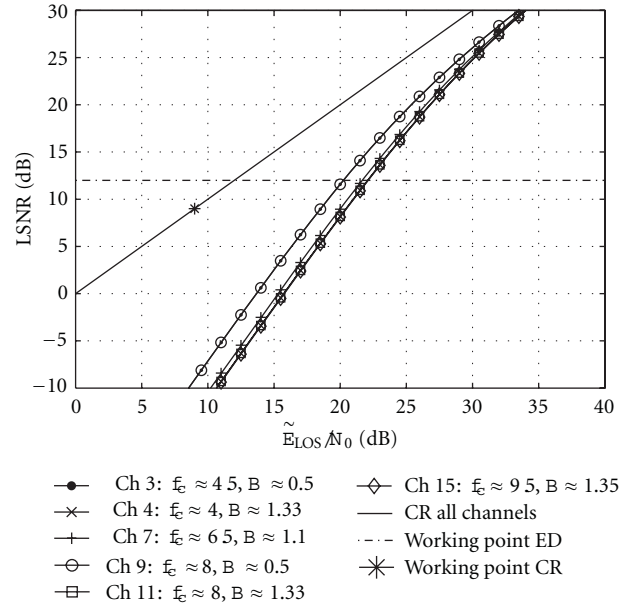


FIGURE 7: Relation between input SNR \tilde{E}_{LOS}/N_0 and output SNR LSNR for the short preamble codes with a spreading $L = 64$ and $N_{pr} = 16$ with respect to the IEEE 802.15.4a channels. The channel parameters in the legend are in GHz.

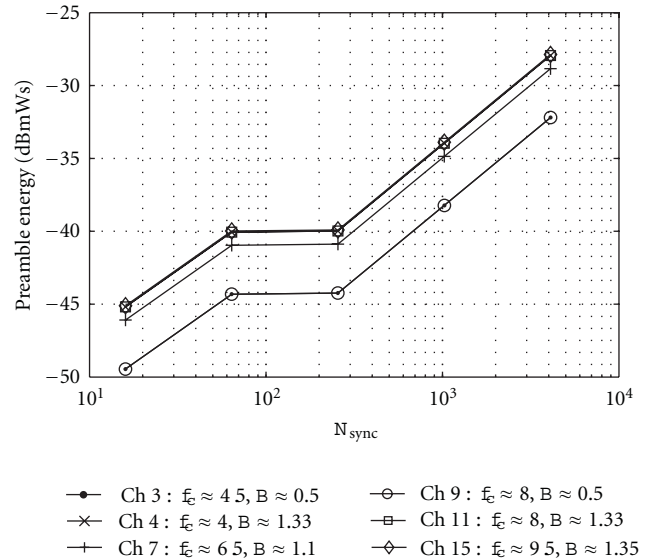


FIGURE 8: Allowed preamble energy for the specific IEEE802.15.4a channels.

be observed that the low-band channels (Ch 3 and Ch 4) perform better than the high-band channels due to lower free-space losses. Only half the operating range is obtained when f_c is increased from 4 to 8 GHz. A shift in the carrier frequency leads to a change of E_{LOS}/N_0 , but it does not change the relation of input and output SNR (compare Ch 3 and Ch 9). A shift of the bandwidth changes this relation due to a change of ND, which is observable for Ch 9 and Ch 11. The operating range is doubled with the CR when the bandwidth is increased from 500 MHz to 1.33 GHz, while only the 1.3

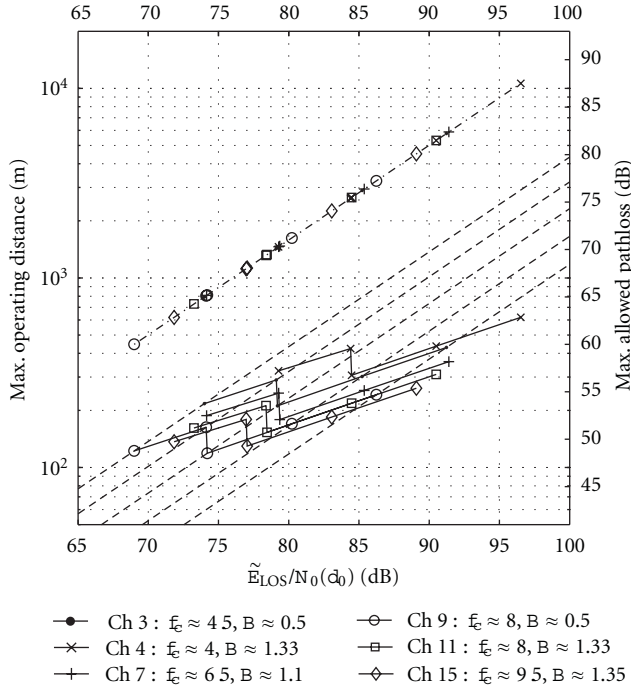


FIGURE 9: Maximal operating distance and maximal allowed pathloss for the specific IEEE 802.15.4a channels. The dashed lines show the characteristic for a channel with $B = 499.2$ MHz with the ND of Figure 6.

fold distance is achieved with the ED. The best performance is obtained at Ch 4, which has a low carrier frequency $f_c \approx 4$ GHz and a large bandwidth of $B \approx 1.33$ GHz. It reaches a $d_{\max} \approx 10620$ m ($PL_{\max} \approx 88$ dB) for the CR and $d_{\max} \approx 620$ m for the ED ($PL_{\max} \approx 63$ dB). The mandatory Ch 3 of the low band shows a significantly better performance in comparison to the mandatory channel in the high band Ch 9 due to the lower f_c .

6. Conclusions

A coherent receiver and an energy detector have been studied for ranging in IEEE 802.15.4a, in the sense of maximal allowed transmit energy, maximal operating distance, and maximum allowed pathloss.

The maximal allowed transmit energy according to the FCC/CEPT regulations depends strongly on the parameters of the preamble. For most of the preamble code sequences, the average power limit applies. A longer spreading of the preamble symbols leads to a performance gain, because a larger preamble energy is obtained. As the FCC/CEPT limits the power spectral density, a higher bandwidth leads to an increased energy too.

The maximal operating distance is calculated from the link budget. The coherent receiver directly depends on the receiver input SNR, while the energy detector is also influenced strongly by the parameters of the preamble codes due to the noncoherent combining loss. A 64-symbol repetitions preamble is most efficient for the energy detector due to lower noncoherent combining losses and the short

preamble symbols are preferable due to less despreading effort. The channels from the low-frequency band achieve longer ranges due to the lower pathloss. The mandatory low-frequency channel ($f_c = 4.5$ GHz) achieves almost twice the range in comparison to the mandatory high-frequency channel ($f_c = 8$ GHz). A gain is obtained for the high-bandwidth channels. The range is almost doubled with the coherent receiver, while the energy detector reaches only a gain of 30 percent.

The low-complexity energy detector achieves maximal operating distances of several hundred meters, while the coherent receiver reaches distances up to several thousand meters in free-space. Thus, both receiver architecture are appropriate for real-time locating systems and sensor networks in typical indoor scenarios.

Acknowledgments

The authors would like to warmly thank G. Kubin, TU Graz, and M. Pistauer, CISC Semiconductor GmbH, for their support in the project. The project was funded by the Federal Ministry for Transport, Innovation and Technology (BMVIT) and the Austrian Research Promotion Agency (FFG).

References

- [1] D. Harmer, M. Russell, E. Frazer et al., "EUROPCOM: emergency ultrawideband radio for positioning and Communications," in *Proceedings of the IEEE International Conference on Ultra-Wideband (ICUWB '08)*, pp. 85–88, 2008.
- [2] J. Rantakokko, P. Hndel, and M. Fredholm, "User requirements for localization and tracking technology," in *Proceedings of the International Conference on Indoor Positioning and Indoor Navigation (IPIN '10)*, pp. 221–222, September 2010.
- [3] M. Z. Win and R. A. Scholtz, "Impulse radio: how it works," *IEEE Communications Letters*, vol. 2, no. 2, pp. 36–38, 1998.
- [4] Y. Qi and H. Kobayashi, "On relation among time delay and signalstrength based geolocation methods," in *Proceedings of the IEEE Global Telecommunications Conference (GLOBECOM '03)*, pp. 4079–4083, December 2003.
- [5] L. Yang and G. B. Giannakis, "Ultra-wideband communications," *IEEE Signal Processing Magazine*, vol. 21, no. 6, pp. 26–54, 2004.
- [6] S. Gezici, Z. Tian, G. B. Giannakis et al., "Localization via ultra-wideband radios: a look at positioning aspects of future sensor networks," *IEEE Signal Processing Magazine*, vol. 22, no. 4, pp. 70–84, 2005.
- [7] I. Guvenc and Z. Sahinoglu, "Threshold-based TOA estimation for impulse radio UWB systems," in *Proceedings of the IEEE International Conference on Ultra-Wideband (ICU '05)*, pp. 420–425, September 2005.
- [8] M. Z. Win, D. Dardari, A. F. Molisch, W. Wiesbeck, and J. Zhang, "History and applications of UWB," *Proceedings of the IEEE*, vol. 97, no. 2, pp. 198–204, 2009.
- [9] N. A. Alsindi, B. Alavi, and K. Pahlavan, "Measurement and modeling of ultrawideband TOA-based ranging in indoor multipath environments," *IEEE Transactions on Vehicular Technology*, vol. 58, no. 3, pp. 1046–1058, 2009.
- [10] IEEE Std., *Part 15.4: Wireless Medium Access Control (MAC) and Physical Layer (PHY) Specifications for Low-Rate Wireless*

Personal Area Networks(WPANs), Amendment 1: Add Alternate PHYs, 2007.

- [11] Y. S. Kwok, F. Chin, and X. Peng, "Ranging mechanism, preamble generation, and performance with IEEE 802.15.4a low-rate low-power UWB systems," in *Proceedings of the IEEE 9th International Symposium on Spread Spectrum Symposium on Spread Spectrum Techniques and Applications (ISSSTA '06)*, pp. 430–434, Bra, August 2006.
- [12] M. Weisenhorn and W. Hirt, "Robust noncoherent receiver exploiting UWB channel properties," in *Proceedings of the International Workshop on Ultra Wideband Systems Joint with Conference on Ultrawideband Systems and Technologies (Joint UWBSTWUWBS '04)*, pp. 156–160, 2004.
- [13] K. Witrisal, G. Leus, G. J. M. Janssen et al., "Noncoherent ultra-wideband systems: An overview of recent research activities," *IEEE Signal Processing Magazine*, vol. 26, no. 4, pp. 48–66, 2009.
- [14] A. A. D'Amico, U. Mengali, and L. Taponocco, "TOA estimation with the IEEE 802.15.4a standard," *IEEE Transactions on Wireless Communications*, vol. 9, no. 7, pp. 2238–2247, 2010.
- [15] T. Gigl, *Low-complexity localization using standard-compliant UWB signals*, Ph.D. thesis, Graz University of Technology, Graz, Austria, 2010.
- [16] T. Gigl, J. Preishuber-Pfluegl, and K. Witrisal, "Statistical analysis of a UWB energy detector for ranging in IEEE 802.15.4a," in *Proceedings of the IEEE International Conference on Ultra-Wideband (ICUWB '09)*, pp. 129–134, September 2009.
- [17] B. Geiger, T. Gigl, J. Preishuber-Pfluegl, and K. Witrisal, "Experimental characterization of system parameters for ranging in IEEE 802.15.4a using energy detectors," *Radioengineering*, vol. 18, no. 3, pp. 249–257, 2009.
- [18] F. Troesch, *Novel low duty cycle schemes: from ultra wide band to ultra low power*, Ph.D. thesis, ETH Zurich, 2010.
- [19] FCC, "Revision of part 15 of the commission's rules regarding ultra-wideband transmission systems," First Report and Order, ET-Docket 98-153, FCC 02-28 Std., FCC, 2002.
- [20] EC, "Commission Decision of 21 April 2009: amending Decision 2007/131/EC on allowing the use of the radio spectrum for equipment using ultra-wideband technology in a harmonised manner in the community," Official Journal of the European Union L105/9 Std., April 2009.
- [21] T. Gigl, J. Preishuber-Pfluegl, D. Arnitz, and K. Witrisal, "Experimental characterization of ranging in IEEE 802.15.4a using a coherent reference receiver," in *Proceedings of the IEEE 20th International Symposium in Personal, Indoor and Mobile Radio Communications*, pp. 92–96, September 2009.
- [22] G. Kolumbán, T. Krébesz, C. K. Tse, and F. C.M. Lau, "Derivation of circuit specification for the UWB impulse radio transceivers," in *Proceedings of the IEEE International Symposium on Circuits and Systems: Nano-Bio Circuit Fabrics and Systems (ISCAS '10)*, pp. 337–340, 2010.
- [23] L. Couch, *Digital and Analog Communication Systems*, Prentice Hall, Upper Saddle River, NJ, USA, 7th edition, 2007.
- [24] G. Fischer, O. Klymenko, and D. Martynenko, "Time-of-arrival measurement extension to a non-coherent impulse radio UWB transceiver," in *Proceedings of the 5th Workshop on Positioning, Navigation and Communication (WPNC '08)*, pp. 265–270, March 2008.

Research Article

Analysis and Mitigation of the Narrowband Interference Impact on IR-UWB Communication Systems

Ehab M. Shaheen¹ and Mohamed El-Tanany²

¹Department of Electronic Warfare, Military Technical College, Tenth District, Nasr City, Cairo 11528, Egypt

²Department of Systems and Computer Engineering, Carleton University, 1125 Colonel By Drive, Ottawa, ON, Canada K1S 5B6

Correspondence should be addressed to Ehab M. Shaheen, efareed2007@yahoo.com

Received 22 September 2011; Revised 11 December 2011; Accepted 13 December 2011

Academic Editor: Yo-Sheng Lin

Copyright © 2012 E. M. Shaheen and M. El-Tanany. This is an open access article distributed under the Creative Commons Attribution License, which permits unrestricted use, distribution, and reproduction in any medium, provided the original work is properly cited.

The impact of narrowband interference signals on impulse radio ultrawideband (UWB) communication systems has been investigated. A closed form expression for the bit error rate performance of UWB communication system in a Log-normal flat fading channel under such impact is evaluated. The actual UWB channel model is known as a multipath fading channel; however flat fading channel model can be considered with some of the UWB wireless applications such as UWB wireless sensor networks which are characterized by size and energy constraints. Thus, a simple and low-cost one-finger Rake receiver can be used with such wireless systems. It was proven that UWB systems unavoidably suffer from the interference caused by the coexisting systems due to the restraint on their transmission power levels. To this end, we propose an interference canceller scheme which is capable of suppressing the impact of such interference and enhancing the performance of UWB communication systems. The interference canceller scheme performance is also investigated in various scenarios of operation such as the presence of multiple narrowband interference signals, symbol timing error, and a comparison with a notch filter-based case.

1. Introduction

In comparison with some traditional communication technologies, UWB communication technologies have some advantages, such as higher multipath resolution, higher data throughput, low probability of detection, and low probability of intercept. So, it is very natural that the appeal of UWB signaling for communications has been more recent and has attracted a lot of attention globally [1].

In order to reduce the interference to existing narrowband systems, the Federal Communications Commission (FCC) also imposed a power restriction on UWB communication systems, where the power spectral density levels are limited to -41.3 dBm/MHz. However, its performance can suffer considerably in the presence of strong narrowband interferences [2, 3].

Previous work on performance analysis of UWB communication systems in the presence of NBI has been largely focused on different types of channel models. In [4] such performance has been investigated in additive white

Gaussian noise (AWGN) channel model under the impact of IEEE802.11a narrowband interference, whereas in [5], such performance has been investigated in Nakagami flat and frequency-selective UWB fading channel models. The impact of NBI on the performance of UWB communication systems in Log-normal multipath fading channel has been investigated in [6].

In 2003, the IEEE802.15.3a model was developed by a standardization group for UWB communication systems in order to compare standardization proposals for high-data rate wireless personal area networks [7]. Although it is clear that the actual UWB channel model is a multipath fading channel, some wireless systems such as the wireless sensor networks are characterized by size and energy constraints. These constraints are imposed on each node that necessitate the use of simple devices. Thus, a one-finger Rake receiver can be considered as a suboptimal solution for simple and low-cost communication systems.

To this end, the goal of this paper is to investigate the performance of IR-UWB communication systems in

the presence of NBI in a Log-normal flat fading channel. A closed form expression for the bit error rate (BER) performance of such systems in the presence of NBI by using a Gaussian Hermite quadrature expansion is derived. In addition, to propose the use of a NBI cancellation scheme that had been used previously with CDMA systems. It will be shown that such canceller scheme is capable of mitigating the impact of NBI signals on UWB communication systems. Its performance is also investigated in different scenarios of operation such as symbol timing error and the presence of multiple NBI signals. Finally, its performance will be compared with the performance obtained by using a notch filter.

The paper is organized as follows. The system model is described in Section 2. In Section 3 the UWB BER performance is analyzed. The idea of such canceller scheme is presented in Section 4. Section 5 presents the used simulation procedures for the proposed canceller scheme. Representative numerical and simulation results are presented in Section 6. Finally, Section 7 draws the conclusions.

2. System and Channel Models

A binary communication system in a single-user case is considered. For a matched filter (MF) reception, the transmitted UWB signal can be written in the form of a time hopping pulse position modulation (TH-PPM) as

$$S_{\text{PPM}}(t) = \sqrt{E_b} \sum_{j=-\infty}^{\infty} p(t - jT_f - c_j T_c - \delta d_{\lfloor j/N_s \rfloor}), \quad (1)$$

where $p(t)$ is the shape of the transmitted pulse with pulse width T_m , d_j is the transmitted j th binary data bit and composed of equally likely bits, and E_b is the bit energy. N_s is the number of pulses transmitted per bit, T_c is the hop width, and c_j is the TH code, $c_j \in \{0, 1, \dots, N_h - 1\}$, such that an additional time shift of " $c_j T_c$ " is introduced when the j th pulse is transmitted. T_f is the frame duration, satisfying $T_f = N_h T_c$; the bit duration can be represented as $T_b = T_f = N_c T_c$ and δ is the modulation index (the time shift added to a pulse with an optimal value of 20% of a pulse width [8]).

The NBI signal, $I(t)$, is modeled as the standard IEEE802.11a, which can be approximated as the sum of " N " tone interferers and it can be written as

$$I(t) = \sum_{n=1}^{N_i} \sqrt{2I_n} \cos(2\pi f_n t + \phi_n), \quad (2)$$

where " f_n " is the n th interference frequency and " ϕ_n " is the phase which can be considered as a random variable uniformly distributed over the interval $[0, 2\pi)$, " I_n " is the transmitted power of the n th tone signal.

Recent measurements indicate that the probability density function (pdf) of the received power in UWB channels is well approximated by Log-normal distribution [9]. Thus, the impulse response of the UWB system in a flat fading channel can be written as [10]

$$h_s(t) = a_s \delta(t - \tau_s), \quad (3)$$

where " a_s " is the channel gain coefficient, and " τ_s " is the associate channel time delay.

We will assume that the NBI signal is affected by Rayleigh fading, thus the NBI channel impulse response can be written as

$$h_i(t) = \alpha_{I_n} \delta(t - \tau_n), \quad (4)$$

where " α_{I_n} " is the Rayleigh distributed channel gain, and " τ_n " is the corresponding time delay, $n = 1, \dots, N_i$.

The overall received signal, $r(t)$, can be written as

$$r(t) = s_d(t) + i_n(t) + n(t), \quad (5)$$

where, $n(t)$ is the AWGN with two-sided power spectral density " $N_o/2$ ". The UWB received signal, $s_d(t) = S_{\text{PPM}}(t) * h_s(t)$, can be written as

$$s_d(t) = \sum_{j=-\infty}^{\infty} a_s \sqrt{E_b} p(t - jT_f - c_j T_c - \delta d_{\lfloor j/N_s \rfloor} - \tau_s), \quad (6)$$

while the NBI received signal, $i_n(t) = I(t) * h_i(t)$, can be written as

$$i_n(t) = \sum_{n=1}^{N_i} \alpha_{I_n} \sqrt{2I_n} \cos(2\pi f_n(t - \tau_n) + \phi_n). \quad (7)$$

Without loss of generality, we will assume that the desired signal channel impulse response, $h_s(t)$, and the interferer channel gains, α_{I_n} , are normalized such that $E[a_s^2] = 1$, and $E[\alpha_{I_n}^2] = 1$, where $E[\cdot]$ denotes the expectation operator.

3. Performance Analysis

In this section, we evaluate the performance of a TH-PPM-UWB system in the presence of NBI in a Log-normal flat fading channel. It will be assumed that the channel is perfectly known at the MF receiver.

The correlation mask can be written as

$$\begin{aligned} m'(t) &= a_s \cdot m(t), \\ m(t) &= [p(t) - p(t - \delta)]. \end{aligned} \quad (8)$$

The transfer function of the MF receiver can be written as $|M(f)| = F.T.\{m(t)\}$, where $F.T.\{\cdot\}$ represents the Fourier Transform process; we can note that " $M(f)$ " depends on the used pulse waveforms.

For a TH-PPM UWB system $M(f)$ can be written as

$$\begin{aligned} |M(f)| &= 2 |P(f)| |\sin(\pi f \delta)| \\ &\times \sum_{k=0}^{N_s-1} \exp(j2\pi f (kT_f + c_k T_c)), \end{aligned} \quad (9)$$

where $P(f)$ is the Fourier Transform of the UWB pulse, $p(t)$, which can be modeled as the six derivative Gaussian pulse as suggested in [11]

$$p(t) = \sqrt{\frac{640}{231N_s\tau_p}} \times \left[1 - 12\pi \left(\frac{t}{\tau_p}\right)^2 + 16\pi^2 \left(\frac{t}{\tau_p}\right)^4 - \frac{64}{15}\pi^3 \left(\frac{t}{\tau_p}\right)^6 \right] \times \exp\left[-2\pi \left(\frac{t}{\tau_p}\right)^2\right], \quad (10)$$

where τ_p is the pulse shaping factor, and the energy of $p(t)$ is $E_p = 1/N_s$.

$$P(f) = \frac{8\pi^3}{3\sqrt{1155}N_s} \tau_p^{13/2} f^6 e^{(-\pi/2)f^2\tau_p^2}. \quad (11)$$

With the consideration of perfect synchronization with the desired signal, the decision statistic can be written as

$$Z = \sum_{j=-\infty}^{\infty} \int_{jT_f}^{j(T_f+1)} r(t) \cdot m'(t) dt \quad (12)$$

$$Z = S_{\text{ppm}} + I_N + n,$$

where S_{ppm} , I_N , and n are the desired signal, interference, and noise components, respectively.

$$S_{\text{ppm}} = \sqrt{E_b}(1 - \rho)a_s^2, \quad (13)$$

where ρ is the correlation coefficient between the two pulses $p(t)$ and $p(t - \delta)$, for bits 0 and 1, respectively, ρ can be written as

$$\rho = \int_{-\infty}^{\infty} p(t)p(t - \delta)dt, \quad \rho \in [-1, 1]. \quad (14)$$

The interference term, I_N can be written as

$$I_N = \sum_{n=1}^{N_i} \alpha_{I_n} \sqrt{2I_n} |M(f_n)| \cos(\phi_n). \quad (15)$$

Following the same approach as [11], the phase term $\{\arg[M(f_n)] + 2\pi f_n(t - \tau_n)\}$ is included within the random phase ϕ_n , conditioned on the r.v. $|M(f_n)|$. Also, each term $\alpha_{I_n} \cos(\phi_n)$ is a zero mean Gaussian r.v. with variance "1/2". Thus, the NBI term, " I_N " can be considered conditionally Gaussian with variance $[\sigma_I^2 = \sum_{n=1}^{N_i} I_n \cdot |M(f_n)|^2]$.

The variance of the noise can be written as

$$\sigma_N^2 = N_o(1 - \rho)a_s^2. \quad (16)$$

The total disturbance due to the NBI plus noise can be considered conditionally Gaussian with variance $[\sum_{n=1}^{N_i} I_n \cdot |M(f_n)|^2 + \sigma_N^2]$.

The conditional bit error probability (BEP), conditioned on (a_s) can be written as

$$P_{e|a_s} = Q(\sqrt{a_s^2\gamma}), \quad (17)$$

where

$$\gamma = \frac{1}{(N_o/E_b(1 - \rho)) + (\sum_{n=1}^{N_i} |M(f_n)|^2 / \text{SIR} \cdot T_b \cdot (1 - \rho)^2)}, \quad (18)$$

where SIR is the signal to interference ratio.

Since " a_s " is Log-normally distributed, then " a_s^2 " is Log-normally distributed as well. The BEP expression is obtained by averaging (17) over " a_s^2 " as

$$P_e \simeq \int_0^{\infty} Q(\sqrt{a_s^2\gamma}) \cdot f(a_s) da_s, \quad (19)$$

where $f(a_s)$ is the pdf of (a_s) , which is normally distributed with mean (μ_r) and variance (σ_r^2) , and is given by

$$f(a_s) = \frac{1}{a_s\sigma_r\sqrt{2\pi}} \exp\left(-\frac{[\ln(a_s) - \mu_r]^2}{2\sigma_r^2}\right). \quad (20)$$

Parameters (μ_k, σ_k) are usually introduced to characterize a Log-normal distribution in wireless communications, where as presented in [12] $\mu_k = \lambda\mu_r$, $\sigma_k = \lambda\sigma_r$, and $\lambda = 10/\ln(10)$. The parameter " σ_k " is known as the dB spread, and its value ranges between 6 and 12 dB for most of the wireless communication systems [12], and between 2 and 5 dB for the UWB systems [13].

In order to calculate (19), the Q-function can be presented by the Craig's formula [14]

$$Q(x) = \frac{1}{\pi} \int_0^{\pi/2} \exp\left(-\frac{x^2}{2\sin^2(\phi)}\right) d\phi. \quad (21)$$

Then, by substituting in (19)

$$P_e = \frac{1}{\pi} \int_0^{\pi/2} \left[\int_0^{\infty} \exp\left(-\frac{a_s^2\gamma}{2\sin^2(\phi)}\right) \frac{1}{a_s\sigma_r\sqrt{2\pi}} \cdot \exp\left(\frac{[\ln(a_s) - \mu_r]^2}{2\sigma_r^2}\right) da_s \right] d\phi, \quad (22)$$

By letting $x = ((\ln(a_s) - \mu_r)/(\sqrt{2}\sigma_r))$, P_e will become

$$P_e = \frac{1}{\pi} \int_0^{\pi/2} \left[\frac{1}{\sqrt{\pi}} \int_{-\infty}^{\infty} e^{-x^2} \cdot \exp\left(-\frac{\gamma}{2\sin^2(\phi)} \cdot \exp[2\sqrt{2}x\sigma_r + 2\mu_r]\right) dx \right] d\phi. \quad (23)$$

The inner integral in (23) can be approximated by a Gauss-Hermite series expansion to become

$$= \frac{1}{\sqrt{\pi}} \sum_{i=1}^N w_i \exp\left(-\frac{\gamma}{2\sin^2(\phi)} \exp[2\sqrt{2}b_i\sigma_r + 2\mu_r]\right) d\phi, \quad (24)$$

where " w_i " and " b_i " are the weights and the associated roots of the Hermite polynomial, respectively. The values of " w_i "

and “ b_i ” can be found in [15]. “ N ” is the number of samples points used in this approximation.

By substituting (24) in (23) we will get

$$P_e = \frac{1}{\sqrt{\pi}} \sum_{i=1}^N w_i \times \left[\frac{1}{\pi} \int_0^{\pi/2} \cdot \exp\left(-\frac{\gamma}{2\sin^2(\phi)} \cdot \exp(2\sqrt{2}b_i\sigma_r + 2\mu_r)\right) \right] d\phi. \quad (25)$$

This equation can be rearranged, where a closed form expression of the BER performance of a UWB system in the presence of NBI signal can be finally evaluated as

$$P_e = \frac{1}{\sqrt{\pi}} \sum_{i=1}^N w_i \left[Q\left(\sqrt{\gamma \cdot \exp(2\sqrt{2}b_i\sigma_r + 2\mu_r)}\right) \right]. \quad (26)$$

4. ICS Performance Analysis

Assuming that the NBI signal is modeled as the standard orthogonal frequency division multiplexing (OFDM) IEEE802.11a signal and the UWB receiver is subjected to a single high power IEEE802.11a NBI signal; the idea of the ICS operates by (1) the incoming received signal will be split into two paths. In the first path an attempt to demodulate the NBI signal from the incoming received signal is done. (2) The output from the demodulation process will be used to regenerate the NBI signal. (3) The regenerated NBI signal will be multiplied by the NBI channel estimate prior to its subtraction from the incoming received signal at the input of the UWB receiver.

If the demodulation process is successful and the NBI channel model is perfectly known, the NBI signal can be perfectly suppressed from the incoming received signal and the reception of the UWB signal can be achieved as if there was no interference.

Figure 1 depicts a simplified schematic model of such canceller scheme. Note that, it has been shown in [5] that the assumption of sum of tone interferers is a good approximation for an OFDM signal. Thus, the OFDM-based IEEE802.11a NBI signal is approximated as “ N ” tone interferers (equal to the OFDM data subcarriers).

In order to analyze the performance of the ICS, the performance of the NBI receiver has to be initially investigated. The NBI receiver probability of symbol error can be summarized into one of the following cases.

Case 1: No Symbol Errors. If the NBI demodulator produces no errors, then the NBI receiver will be able to perfectly regenerate the NBI signal and the canceller scheme will efficiently suppress the NBI signal. In such case, the BER performance of the ICS is equivalent to the performance of a UWB system in the absence of interference.

Case 2: Multiple Symbol Errors. When the NBI demodulator produces multiple symbol errors, the BER of the ICS in this case can be written as

$$(P_e)_{\text{uwb}}^{\text{ics}} = P_{e-\text{uwb}}^{\text{no int.}} \times \left(1 - P_{\text{ofdm}}^{e=1} - \dots - P_{\text{ofdm}}^{e=e'}\right) + P_{e-\text{uwb}}^1 \times P_{\text{ofdm}}^{e=1} + \dots + P_{e-\text{uwb}}^{e'} \times P_{\text{ofdm}}^{e=e'}, \quad (27)$$

where $P_{e-\text{uwb}}^{\text{no int.}}$ is the BER performance of a UWB system in the absence of interference, $(P_{e-\text{uwb}}^{e'})$ is the probability of a UWB system in the presence of (e') tone interferers, while $(P_{\text{ofdm}}^{e=e'})$ is the probability of e' symbol errors occurring in a block of length “ N ” symbols.

Note that, the probability that the NBI receiver produces “ e ” symbol errors over a block of “ N ” symbols is given by [16]

$$P_{\text{ofdm}}^e = \frac{N!}{(N-e)! \times e!} P^e (1-P)^{N-e}, \quad (28)$$

where “ N ” can be interpreted for an OFDM NBI signal as the number of the OFDM data subcarriers, and “ P ” is the probability of symbol error.

It is worth mentioning that, the NBI receiver average probability of OFDM symbol error (av. Pse) can be considered as one of the main factors that control the performance of such canceller scheme. By manipulating this parameter we can evaluate the ICS performance.

5. Simulation of the ICS

Figure 2 depicts the simulation blocks of the ICS. The sampling rates of the UWB and IEEE802.11a NBI signals are “50 GHz” and “20 MHz,” respectively. In simulation points “C and D”, the IEEE802.11a NBI signal and the UWB signals are generated after adding the impact of their respective channel models.

Detection and noise level adjustment stages are used in order to generate the AWGN with the desired SNR ratio. It is worth mentioning that pilot symbols are inserted at the IEEE802.11a transmitter in all frequency domains at fixed time intervals (as in each subcarrier channel, the level of fluctuation is independent), where at the receiver the NBI channel is estimated with the aid of these pilot symbols.

6. Numerical Results

In this section, numerical examples are presented to investigate the performance of both a TH-PPM system and the ICS in Log-normal flat fading channels and validated with the aid of simulation. A six derivative Gaussian received pulse will be used with values: $\tau_p = 0.192$ ns, $\delta = 0.068$ ns, $T_f = 10$ ns, $N_s = 1$ pulse/bit, and $\rho = -0.824$. The standard IEEE802.11a NBI signal will operate at the upper U-NII band with center frequency = 5.745 GHz, and the frequency spacing between the carriers $\Delta f = 0.3125$ MHz.

Figure 3 numerically evaluates the BER performance of TH-PPM UWB system in the presence of IEEE802.11a NBI at different SIRs. It can be seen that the performance of a UWB

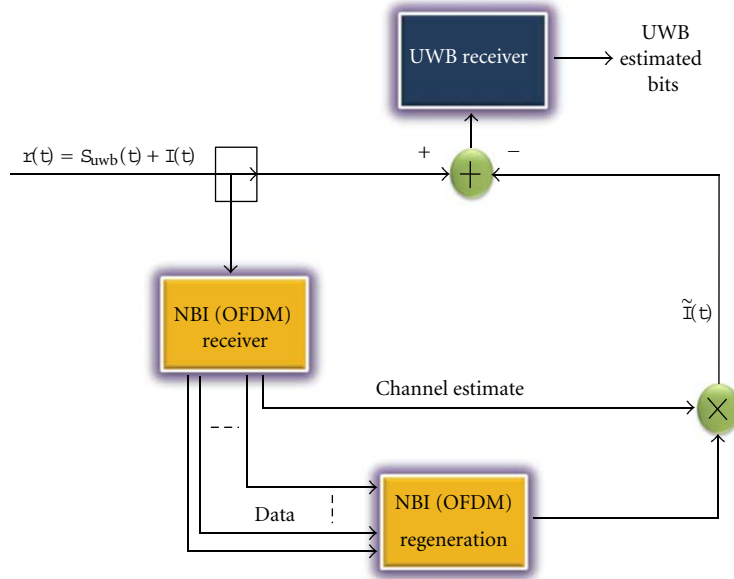


FIGURE 1: A simplified schematic model for the proposed canceller scheme.

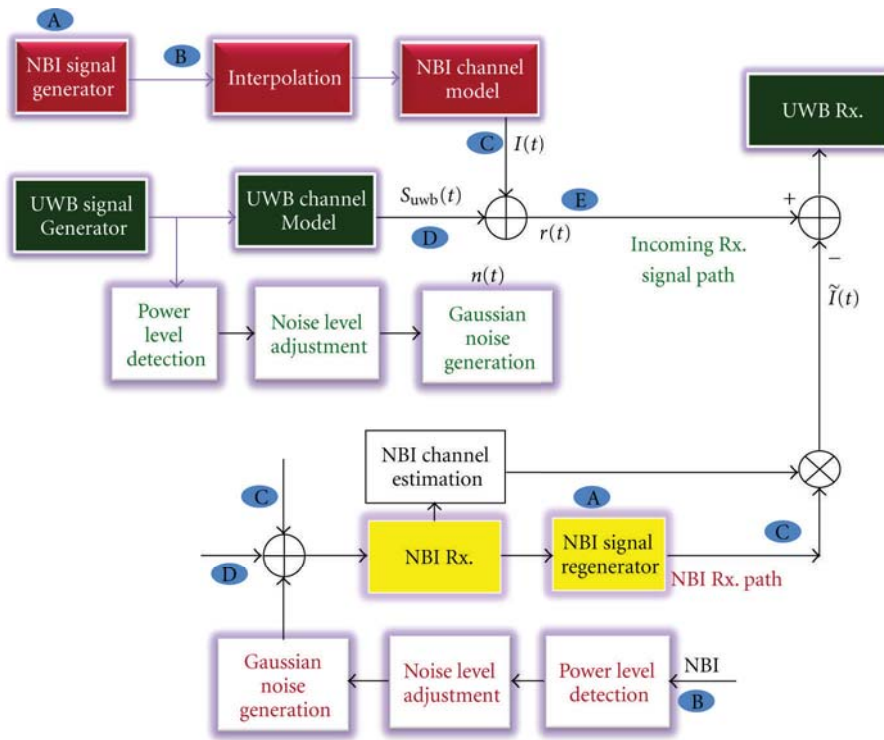


FIGURE 2: Simulation block diagram of the proposed canceller scheme.

system is deteriorated due to the presence of NBI. A SNR degradation is expected to be less than 2 dB and 12 dB for SIR = -5 and -10 dB, respectively, at BER = 1 × 10⁻².

Figure 4 depicts a comparison between the simulation and analytical performance of a TH-PPM UWB system with the aid of the ICS at SIR = -10 dB and dB-spread = 3 dB.

It can be seen that the impact of NBI can be completely suppressed at an av. Pse = 1 × 10⁻³, whereas for an av. Pse = 0.05, the SNR degradation is less than 2 dB at BER = 1 × 10⁻³.

Also it can be seen that the simulation and the analytical results are in a good agreement, in which we can conclude the validation of the obtained analytical results.

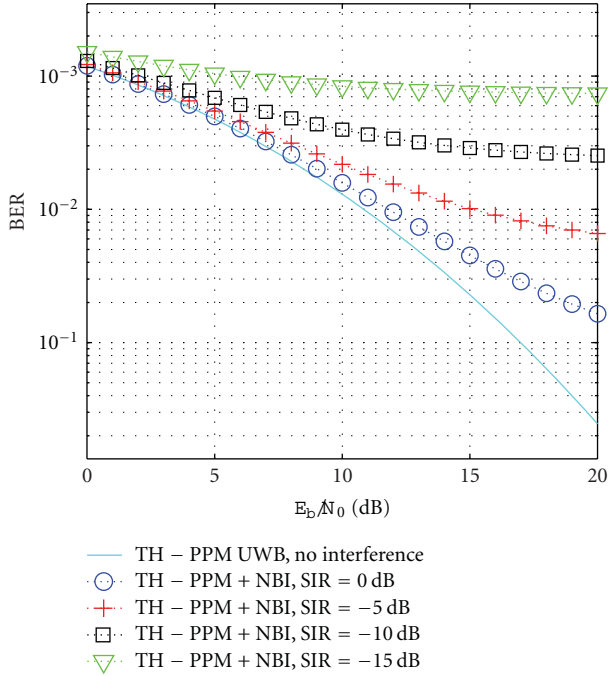


FIGURE 3: TH-PPM UWB performance in the presence of NBI.

Now the performance of the ICS is investigated in various scenarios of operation as follows.

6.1. Symbol Timing Error. The first considered scenario is the presence of symbol timing errors (timing misalignment errors) between the regenerated NBI signal and the incoming received signal at the input of the subtraction process.

Figure 5 depicts the ICS performance in a Log-normal flat fading channel, the av. Pse = 0.1, dB-spread value = 2 dB and SIR = -15 dB. It can be seen that for a timing misalignment error equal to 0.5%, there is an additional SNR degradation equal to 2 dB at BER = 3×10^{-3} , whereas, for a timing misalignment error equals to 1% there is an additional SNR degradation equals to 4 dB at BER = 5×10^{-2} .

6.2. Multiple NBI Signals. The second considered scenario is the presence of two IEEE802.11a NBI signals. The ICS attempts to mitigate the impact of each NBI signal individually, where it regenerates and subtracts each NBI signal from the incoming received signal at the input of the UWB receiver. It is worth noting that the two used NBI signals have center frequencies 5.22 GHz and 5.745 GHz, respectively.

Figure 6 depicts a comparison between the BER performances of the canceller scheme in the presence of one and two NBI WLANs, the dB-spread value is 3 dB and the SIR = -10 dB.

It can be seen that an additional SNR degradation in the ICS performance is expected to be less than 2 dB at BER = 1×10^{-2} .

6.3. Notch Filter-Based Case. The performance effectiveness of the ICS is analyzed by making a comparison with

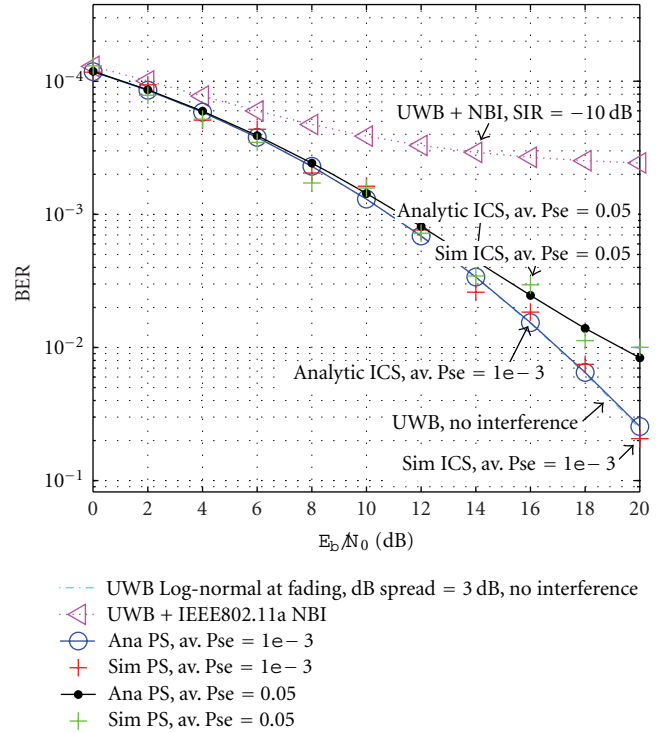


FIGURE 4: Simulation and analytical performance comparison of the ICS, dB-spread = 3 dB and SIR = -10 dB.

the performance obtained by using a notch filter. The notch filter was simulated as a resonator with quality factor ($Q = 35$). The 3 dB bandwidth of the notch filter with the previous quality factors will be 165 MHz for a WLAN NBI signal with center frequency = 5.745 GHz.

The comparison is done in two scenarios: (1) the notch filter is assumed perfectly tuned to the center frequency of the NBI signal. (2) The notch filter is detuned and there is a shift between the center frequency of the NBI signal and the notch frequency.

Figure 7 depicts the BER performance comparison between a notch filter which is perfectly tuned to the center frequency of the NBI signal and the proposed ICS at SIR = -10 dB and dB-spread = 3 dB. It can be seen that the ICS with av. Pse = $1e-3$ and 0.01 outperforms the perfectly tuned notch filter. However, for an av. Pse = 0.05, the notch filter outperforms the ICS specially for large SNR.

Figure 8 depicts this comparison with a detuned notch filter with a notch frequency shift equal to 40 MHz. It can be seen that the ICS always outperform the detuned notch filter even with an av. Pse = 0.05, which means that the notch filter has to be perfectly tuned and has a prior knowledge about the center frequency of the NBI.

6.4. ICS Complexity. It can be seen from the previous discussion that the proposed canceller scheme is more complex than the use of a notch filter. Yet, the notch filter has to have a prior knowledge of the NBI signal. Also, the ICS is more agile than the notch filter based case in mitigating NBI

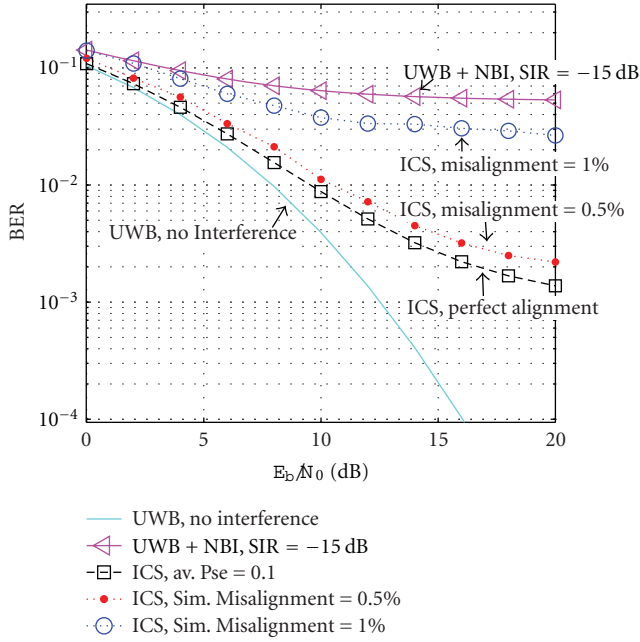


FIGURE 5: Timing error impact in the ICS performance, dB-spread = 2 dB and SIR = -15 dB.

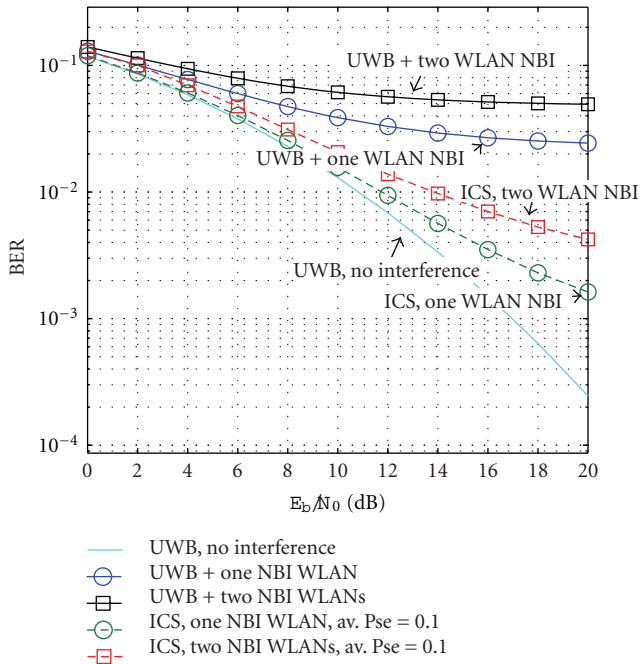


FIGURE 6: BER performance of the ICS in the presence of two NBI WLANs in a Log-normal flat fading channel, SIR = -10 dB.

signals as a detuned notch filter will not be able to mitigate the NBI impact on the UWB receiver. Such agility feature can compensate for the ICS's complexity drawback.

7. Conclusion

In this paper, the impact of IEEE802.11a NBI on the performance of a TH-PPM UWB system in a Log-normal

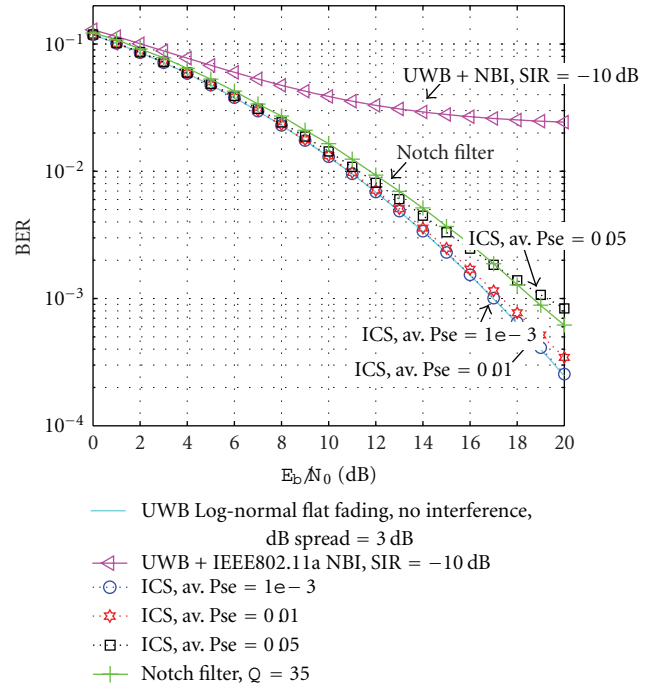


FIGURE 7: BER performance comparison of the ICS with a perfectly tuned Notch filter.

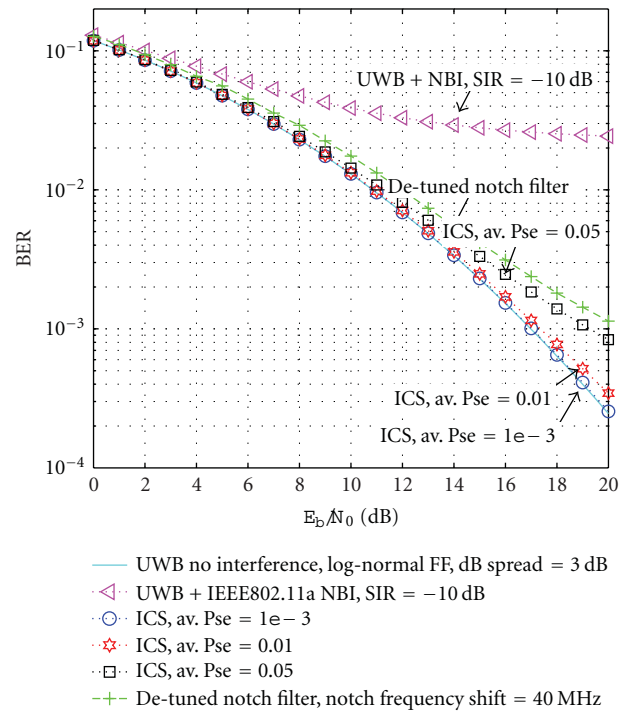


FIGURE 8: BER performance comparison of the ICS with a De-tuned Notch filter.

flat fading channel is investigated. Although, the considered channel is not the actual UWB channel, but this investigation is suitable for some wireless systems such as the wireless

sensor networks. It has been shown that the impact of the IEEE802.11a NBI signal can severely degrade the UWB BER performance.

To this end, a canceller scheme that had been used with the CDMA systems is proposed to mitigate the impact of such interference on UWB communication systems. The ICS performance is analytically evaluated in Log-normal flat fading channels and validated with the aid of simulation.

The ICS performance is also investigated in various scenarios of operation such as the presence of symbol timing errors, the presence of two IEEE802.11a NBI signals, and a comparison with the performance obtained by using the conventional tuned and detuned notch filter. It was shown that such canceller scheme is capable of mitigating the impact of NBI signals on UWB communication systems and outperforming the notch filter based case.

References

- [1] H. Quach and A. Dinh, "Narrowband interference elimination in UWB communications systems," in *Proceedings of the Canadian Conference on Electrical and Computer Engineering (CCECD '07)*, pp. 1341–1344, Vancouver, BC, Canada, 2007.
- [2] E. M. Shaheen and M. El-Tanany, "BER analysis of UWB systems in the presence of narrowband interference in lognormal multipath fading channels," in *Proceedings of the IEEE Military Communications Conference (MILCOM '09)*, pp. 1–7, Boston, Mass, USA, 2009.
- [3] E. M. Shaheen and M. El-Tanany, "The impact of narrowband interference on the performance of UWB systems in the IEEE802.15.3a channel models," in *Proceedings of the IEEE 23rd Annual Canadian Conference on Electrical and Computer Engineering (CCECE '10)*, May 2010.
- [4] B. Hu and N. C. Beaulieu, "Effects of IEEE 802.11a narrowband interference on A UWB communication system," in *Proceedings of the IEEE International Conference on Communications (ICC '05)*, vol. 4, pp. 2818–2824, 2005.
- [5] M. Chiani and A. Giorgetti, "Coexistence between UWB and narrow-band wireless communication systems," *Proceedings of the IEEE*, vol. 97, no. 2, pp. 231–254, 2009.
- [6] J. Wang and W. Tung, "Narrowband interference suppression in time-hopping impulse radio ultra-wideband communications," *IEEE Transactions on Communications*, vol. 54, no. 6, pp. 1057–1067, 2006.
- [7] A. F. Molisch, J. R. Foerster, and M. Pendergrass, "Channel models for ultrawideband personal area networks," *IEEE Wireless Communications*, vol. 10, no. 6, pp. 14–21, 2003.
- [8] F. Ramirez-Mireles, "Signal design for ultra-wide-band communications in dense multipath," *IEEE Transactions on Vehicular Technology*, vol. 51, no. 6, pp. 1517–1521, 2002.
- [9] A. F. Molisch, "Ultra-wide-band propagation channels," *Proceedings of the IEEE*, vol. 97, no. 2, pp. 353–371, 2009.
- [10] M. D. Benedetto and G. Giancola, *Understanding Ultra Wideband Radio Fundamentals*, Prentice Hall, 2004.
- [11] A. Giorgetti and D. Dardari, "The impact of OFDM interference on TH-PPM/BPAM transmission systems," in *Proceedings of the IEEE 61st Vehicular Technology Conference (VTC '05)*, vol. 2, pp. 1037–1042, Stockholm, Sweden, May-June 2005.
- [12] N. C. Beaulieu, A. A. Abu-Dayya, and P. J. McLane, "Estimating the distribution of a sum of independent lognormal random variables," *IEEE Transactions on Communications*, vol. 43, no. 12, pp. 2869–2873, 1995.
- [13] J. Foerster et al., "Channel modelling sub-committee report final," Tech. Rep. P802.15-02/490r1-SG3a, IEEE P802.15 Wireless Personal Area Networks, 2003.
- [14] M. K. Simon and M. S. Alouini, *Digital Communication Over Fading Channels*, Wiley-Interscience, 2nd edition, 2005.
- [15] M. Abramowitz and I. Stegun, *Handbook of Mathematical Functions With Formulas, Graph, and Mathematical Tables*, Dover, New York, NY, USA, 9th edition, 1971.
- [16] R. E. Ziemer and R. L. Peterson, *Introduction to Digital Communication*, Prentice Hall, 2001.